

# **Exergy Methods for the Mission-Level Analysis and Optimization of Generic Hypersonic Vehicles**

**Keith Merritt Brewer**

Thesis submitted to the Faculty of the  
Virginia Polytechnic Institute and State University  
in partial fulfillment of the requirement for the degree of

Master of Science  
In  
Mechanical Engineering

Dr. Michael von Spakovsky, Chair

Dr. Walter O'Brien

Dr. Michael Ellis

Dr. David Moorhouse

April 21, 2006

Blacksburg, Virginia

Keywords: exergy, hypersonic, optimization, scramjet

# **Exergy Methods for the Mission-Level Analysis and Optimization of Generic Hypersonic Vehicles**

by Keith Merritt Brewer

## **Abstract**

Though the field of hypersonic vehicle design is thriving again, few studies to date demonstrate the technology through a mission in which multiple flight conditions and constraints are encountered. This is likely due to the highly integrated and sensitive nature of hypersonic vehicle components. Consequently, a formal Mach 6 through Mach 10 flight envelope is explored which includes cruise, acceleration/climb, deceleration/descend and turn mission segments. An exergy approach to the vehicle synthesis/design, in which trade-offs between dissimilar technologies are observed, is proposed and measured against traditional methods of assessing highly integrated systems.

A quasi one-dimensional hypersonic vehicle system simulation program was constructed. Composed of two sub-systems, propulsion and airframe, mechanisms for loss are computed from such irreversible processes as shocks, friction, heat transfer, mixing, and incomplete combustion. The propulsion sub-system consists of inlet, combustor, and nozzle, while the airframe provides trim and force accounting measures. An energy addition mechanism, based on the potential of MHD technology, is utilized to maintain a shock-on-lip inlet operating condition. Thirteen decision variables (seven design and six operational) were chosen to govern the vehicle geometry and performance. A genetic algorithm was used to evaluate the optimal vehicle synthesis/design for three separate objective functions, i.e the optimizations involved the maximization of thrust efficiency, the minimization of fuel mass consumption, and the minimization of exergy destruction plus fuel exergy loss.

The principal results found the minimum fuel consumption and minimum exergy destruction measures equivalent, both meeting the constraints of the mission while using 11% less fuel than the thrust efficiency measure. Optimizing the vehicle for the single most constrained mission segment yielded a vehicle capable of flying the entire mission but with fuel consumption and exergy destruction plus fuel loss values greater than the above mentioned integrated vehicle solutions. In essence, the mission-level analysis provided much insight into the dynamics of mission-level hypersonic flight and

demonstrated the usefulness of an exergy destruction minimization measure for highly integrated synthesis/design.

# Acknowledgements

I would like to thank Dr. Michael von Spakovsky for firstly initiating an interesting and research worthy topic and secondly providing me the opportunity of participating in its development through two years of funding (not to mention his patience with its conclusion). Not only has this degree afforded invaluable technical and personal growth but also provided an exceptional chance to meet new friends and appreciate Virginia Tech and the Town of Blacksburg.

Kyle Markell shared a research topic, office, and at one time a residence with me over the course of this work. Kyle's assistance, insight, patience, and attention to detail were all invaluable, without which this work could not be completed. Kyle also had the privilege of defending his thesis first, for which I am thankful.

There were innumerable instances in which Dr. David Riggins and Dr. David Moorhouse offered much needed and expert suggestions regarding the specifics of this work. Their patience and resourcefulness throughout were greatly appreciated. In addition, many thanks to Ball Aerospace and the U.S. Air Force Office of Scientific Research for the opportunity to work along side these and other great minds at Wright Patterson Air Force Base while enjoying a great (and Chipotle filled) summer in Dayton, OH.

I am grateful to Drs. David Moorhouse, Walter O'Brien and Michael Ellis for serving as members of my graduate committee, reviewing and editing this work, and certainly providing valuable feedback.

Finally, I would like to thank my parents and brother for their support (both emotional and financial) and instilling in me their deep respect for education that has led me to have so many great experiences.

Keith Merritt Brewer

# Table of Contents

LIST OF FIGURES.....	VII
LIST OF TABLES.....	IX
NOMENCLATURE.....	XI
CHAPTER 1 INTRODUCTION.....	1
1.1 THE EVOLUTION OF AIRBREATHING PROPULSION.....	1
1.1.1 <i>Propellers</i> .....	2
1.1.2 <i>Turbojets</i> .....	3
1.1.3 <i>Ramjets</i> .....	4
1.2 HYPERSONIC AIRBREATHING PROPULSION.....	5
1.2.1 <i>Scramjets</i> .....	5
1.2.2 <i>Hypersonic Challenges</i> .....	7
1.2.3 <i>Recent Milestones in Hypersonic Flight</i> .....	9
1.3 HYPERSONIC VEHICLE SYNTHESIS/DESIGN.....	10
1.3.1 <i>An Exergy Based Approach</i> .....	10
1.3.2 <i>Thesis Objectives</i> .....	11
CHAPTER 2 REVIEW OF LITERATURE.....	13
2.1 HYPERSONIC VEHICLE OPTIMIZATION.....	13
2.1.1 <i>Inlet Flow Control</i> .....	13
2.1.2 <i>Vehicle Configurations</i> .....	15
2.2 EXERGY METHODS FOR VEHICLE PERFORMANCE EVALUATION.....	21
2.2.1 <i>Exergy Analyses of Scramjet Engines</i> .....	21
2.2.2 <i>System and Mission-Level Exergy Applications in High Performance Aircraft Applications</i> .....	31
CHAPTER 3 VEHICLE SUB-SYSTEM AND COMPONENT MODELS.....	37
3.1 TECHNICAL BACKGROUND/ SYSTEM OVERVIEW.....	37
3.1.1 <i>Equations of Motion</i> .....	37
3.1.2 <i>Compressible Flow Relations</i> .....	40
3.1.3 <i>Generalized One-Dimensional Flow</i> .....	46
3.1.4 <i>Hypersonic Vehicle Description and Decomposition</i> .....	48
3.2 INLET COMPONENT MODEL.....	48
3.2.1 <i>Inlet Design and Variables</i> .....	48
3.2.2 <i>Inlet Solution Procedure</i> .....	50
3.2.3 <i>Inlet Loss Mechanisms</i> .....	56
3.2.4 <i>Inlet Constraints</i> .....	56
3.2.5 <i>Inlet Design Considerations</i> .....	58
3.3 COMBUSTOR COMPONENT MODEL.....	58
3.3.1 <i>Combustor Design and Variables</i> .....	59
3.3.2 <i>Combustor Solution Procedure</i> .....	60
3.3.3 <i>Combustor Loss Mechanisms</i> .....	68
3.3.4 <i>Combustor Constraints</i> .....	70
3.4 NOZZLE COMPONENT MODEL.....	70
3.4.1 <i>Nozzle Design and Variables</i> .....	71
3.4.2 <i>Nozzle Solution Procedure</i> .....	72
3.4.3 <i>Nozzle Loss Mechanisms</i> .....	76
3.4.4 <i>Nozzle Constraints</i> .....	76
3.4.5 <i>Nozzle Design Considerations</i> .....	77
3.5 AIRFRAME SUB-SYSTEM MODEL.....	78
3.5.1 <i>Atmospheric Flight</i> .....	79
3.5.2 <i>Force Accounting</i> .....	80

3.5.3 Lift and Trim.....	83
3.5.4 Vehicle Mass Estimations.....	86
3.5.5 Airframe Solution Procedure.....	87
3.5.6 Aerodynamic Loss Mechanisms.....	88
3.5.7 Airframe Sub-system Constraints.....	89
<b>CHAPTER 4 MISSION-LEVEL SYNTHESIS/DESIGN CHALLENGE .....</b>	<b>91</b>
4.1 MISSION OVERVIEW .....	91
4.1.1 Climb/Acceleration and Descend/Deceleration.....	93
4.1.2 Constant Altitude/Speed Cruise.....	95
4.1.3 Constant Altitude/Speed Turn.....	95
4.1.4 Total Mission.....	96
4.2 PROGRAM OPTIMIZATION.....	97
4.2.1 Optimization Background.....	98
4.2.2 Objective Functions.....	98
4.2.3 MooLENI Evolutionary Algorithm.....	100
4.2.3 Hypersonic Vehicle Model and Optimization Integration.....	101
<b>CHAPTER 5 RESULTS.....</b>	<b>103</b>
5.1 INTEGRATED HYPERSONIC VEHICLE MODEL VALIDATION AND EXPLORATION .....	103
5.1.1 Engine Sub-system.....	103
5.1.2 Airframe and Engine Sub-systems – Thermodynamic/Flow Conditions.....	106
5.1.3 Airframe and Engine Sub-systems – Shock-on-Lip.....	108
5.1.4 Airframe and Engine Sub-systems – Airframe and Propulsive Trim Effects.....	112
5.1.5 Airframe and Engine Sub-systems – Airframe and Propulsive Lift and Drag Effects.....	116
5.1.5 Effects of Single Segment Discretizations.....	120
5.2 MISSION-LEVEL OPTIMIZATION OF THE INTEGRATED HYPERSONIC VEHICLE .....	123
5.2.1 Objective Function and Vehicle Synthesis/Design.....	123
5.2.2 Objective Function and Vehicle Mission Segment Exergy Destruction Plus Fuel Exergy Loss.....	128
5.2.3 Objective Function and Vehicle Fuel Consumption.....	130
5.2.4 Vehicle Evolution.....	132
5.3 THE OPTIMIZATION PROCESS.....	134
5.4 TOTAL MISSION AND MISSION SEGMENT OPTIMIZATION COMPARISONS .....	139
5.4.1 Combined Single Segment Optimized Vehicle Performance versus Mission-Level Optimized Vehicle Performance.....	139
5.4.2 Mission-Level Performance of Single Segment Optimized Vehicles .....	142
5.5 HIGH PERFORMANCE MISSION EXPLORATION.....	144
<b>CHAPTER 6 CONCLUSION.....</b>	<b>146</b>
<b>REFERENCES.....</b>	<b>149</b>

# List of Figures

Figure 1.1. An illustration of airbreathing and non-airbreathing propulsive devices.	1
Figure 1.2. A propeller creates thrust by accelerating the ambient airflow.	2
Figure 1.3. A generic turbojet engine.	3
Figure 1.4. The synthesis of engine and fuselage in a generic fighter aircraft [2].	4
Figure 1.5. A generic ramjet configuration.	4
Figure 1.6. A dual mode turboramjet concept. A common diffuser accommodates both the turbojet (top) for low speed flight and the ramjet (bottom) for high speed flight [3].	5
Figure 1.7. A generic scramjet engine flowpath.	6
Figure 1.8. Physical effects characteristic of hypersonic flow [4].	7
Figure 1.9. NASA's X-43A vehicle dimensions [6].	9
Figure 1.10. NASA's X-43A mission profile [6].	10
Figure 2.1. Inlet flow operational conditions.	14
Figure 2.2. Potential inlet flow control methods using plasmas [21].	15
Figure 2.3. Vehicle defining parameters [25].	16
Figure 2.4. The fixed geometry inlet model used by Hendrick [26].	17
Figure 2.5. The effect of energy and exergy performance measures on optimization for (a) combustor inlet pressure and (b) angle of attack [26].	19
Figure 2.6. A periodic hypersonic cruise trajectory [27].	19
Figure 2.7. Hypersonic vehicle configuration and design variables [27].	20
Figure 2.8. Simple scramjet engine model [31].	24
Figure 2.9. Effectiveness parameters vs. combustor length [31].	24
Figure 2.10. Engine thrust effectiveness and thermodynamic effectiveness vs. combustor length [9].	25
Figure 2.11. Carpet plot for sized mission fuel weight as a function of OPR and TIT for the F-5E with J85 derivative engines [33].	27
Figure 2.12. Chargeable fuel weights for an F-5E subsonic area intercept mission as a function of OPR and TIT [33].	28
Figure 2.13. Parametric plot of inlet forebody angle and inlet first ramp length on engine specific exergy destruction and specific thrust [9].	30
Figure 2.14. Parametric plot of combustor length and nozzle expansion angle on engine specific exergy destruction and specific thrust [9].	30
Figure 2.15. Variation of vehicle specific thrust and exergy destruction rate with fan bypass ratio and turbine inlet temperature for a fixed compressor pressure ratio of 8. (mission segment 5: Climb) [10].	35
Figure 3.1. Oblique shock and centered expansion fan.	41
Figure 3.2. Oblique shock detail.	42
Figure 3.3. Detached shocks occur at angles greater than $\nu_{max}$ .	44
Figure 3.4. Prandtl-Meyer expansion detail for (a) an infinitesimal obtuse turning angle and (b) general flow turning.	44
Figure 3.5. A generic one-dimensional differential duct with multiple physical interactions.	46
Figure 3.6. Propulsion sub-system components and airframe sub-system.	48
Figure 3.7. Inlet geometry and design details [9].	49
Figure 3.8. Inlet interface and vehicle geometric definitions [9].	50
Figure 3.9. Inlet throat detail [9].	52
Figure 3.10. Conceptual diffuser used to calculate the entropy generation rate due to friction [9].	54
Figure 3.11. Inlet flow tailoring system using energy exchange [9].	55
Figure 3.12. Combustor schematic [9].	60
Figure 3.13. Combustor differential element [9].	62
Figure 3.14. Wall enthalpies with and without heat transfer [3].	65
Figure 3.15. Mixing and combustion efficiencies versus combustor length [9].	68
Figure 3.16. Nozzle schematic.	71
Figure 3.19. Three-dimensional nozzle view.	74

Figure 3.20. Plume interaction for a differential element.	75
Figure 3.21. Pressure ratio limit vs. beneath cowl flow Mach number.	77
Figure 3.22. 2-D method of characteristics applied to a nozzle with 258 nozzle entrance expansion angle and 1 meter throat height.	78
Figure 3.23. Forces acting on an aerospace vehicle during flight.	79
Figure 3.24. Resolved force accounting.	81
Figure 3.25. Illustration of integration technique [9].	82
Figure 3.26. The five composite areas of the vehicle [9].	83
Figure 3.27. (a) Vehicle plan area and (b) elevon and wing cross-section detail [9].	84
Figure 3.28. Lift to Drag ratio for the diamond airfoil at Mach numbers and angles of attack of interest.	85
Figure 4.1. Total scramjet vehicle mission.	91
Figure 4.2. Acceleration detail.	93
Figure 4.3. Forces acting on an aerospace vehicle during flight.	94
Figure 4.4. Force balance during a turn (tail view).	96
Figure 5.1. Hypersonic vehicle flow condition boundaries.	106
Figure 5.2. Inlet flow dynamics for shock-on-lip control for (a) Mach 6 to Mach 8 (design) and (b) Mach 8 to Mach 10 acceleration mission segments. Values given for the inlet Mach number are from the baseline thrust efficiency-based objective function vehicle described in table 5.4.	110
Figure 5.3. Required energy/exergy addition for the baseline thrust efficiency-based objective function vehicle.	111
Figure 5.4. Airframe and propulsive forces acting on the hypersonic vehicle.	112
Figure 5.5. Airframe and propulsive moments acting on the hypersonic vehicle. Positive values indicate a nose-up pitching moment.	114
Figure 5.6. Lift to drag ratio for the diamond airfoil.	115
Figure 5.7. Component contributions to overall vehicle drag per mission segment for the baseline thrust efficiency-based objective function vehicle.	117
Figure 5.8. Breakdown of sub-system charged lift for nose-, inlet-, and cowl-to-tail force accounting systems. Values are given for the Mach 6 to Mach 8 acceleration segment of the baseline thrust efficiency-based objective function vehicle.	120
Figure 5.9. Optimum vehicle geometry for each of the three objective functions.	125
Figure 5.10. Drag contribution by airframe component for the optimum vehicles. Obj1, Obj2, and Obj3 are the maximized thrust efficiency, minimum fuel mass, and minimum exergy objective functions, respectively.	127
Figure 5.11. Lift contribution by airframe component for the optimum vehicles.	128
Figure 5.12. Exergy destruction plus fuel exergy loss per mission segment.	128
Figure 5.13. Exergy destroyed plus fuel exergy lost per mission segment for the best performing integrated vehicles.	129
Figure 5.14. Fuel mass used per mission segment for each of the objective functions.	131
Figure 5.15. Vehicle geometry evolutions from the initial to the optimal solution for each objective function.	133
Figure 5.16. Performance characteristics for the single segment and integrated mission optimizations.	141
Figure 5.17. Performance characteristics for the Mach 6 to Mach 8 single segment optimized vehicle over the complete hypersonic mission envelope compared to the mission-level integrated vehicle optimizations.	143

# List of Tables

Table 1.1. Typical takeoff weight fraction breakdowns of current aircraft and multi-stage rocket transportation systems [3].	7
Table 2.1. Bowcutt's selected geometric parameters [25].	16
Table 2.2. Decision variable fixed values and ranges for Markell's parametric study [9].	29
Table 2.3. Objective functions for the AAF synthesis/design optimization performed by Periannan [10].	34
Table 3.1. Prandtl-Meyer function and maximum turning angles for various Mach numbers ( $\gamma = 1.4$ ).	45
Table 3.2. Influence coefficients for flow in a duct [42].	47
Table 3.3. Inlet independent design and operational variables.	49
Table 3.4. Inlet design and operational constraints.	57
Table 3.5. Inlet flow parameters.	58
Table 3.6. Combustor design variables.	59
Table 3.7. Combustor parameters.	61
Table 3.8. Nozzle design decision variables.	71
Table 3.9. Airframe decision (independent) and dependent sub-system variables.	88
Table 4.1. Mission segment details.	92
Table 4.2. Air and vehicle flight envelope data for a dynamic pressure of 85kPa.	92
Table 4.3. Mission segment characteristics and constraining conditions.	97
Table 4.4. Mission design and operational decision variables for the inlet, nozzle, combustor, and airframe.	101
Table 5.1. Combustor model comparison/validation .	104
Table 5.2. Required and actual mass flow rates of $H_2$ .	105
Table 5.3. Effects of step size on nozzle exit results.	106
Table 5.4. Flow properties for a thrust efficiency-based objective function baseline vehicle over the entire hypersonic mission.	107
Table 5.5. Shock-on-lip exergy destruction [GJ] for the baseline thrust efficiency-based objective function vehicle.	109
Table 5.6. Breakdown of moments due to surface forces for the baseline thrust efficiency-based objective function vehicle. For the vehicle shown in figure 5.4, positive values indicate a clockwise (nose-up) moment.	113
Table 5.7. Breakdown of overall vehicle drag for the baseline thrust efficiency-based objective function vehicle.	116
Table 5.8. Propulsion and airframe sub-system contributions to overall vehicle lift for the baseline thrust efficiency-based objective function vehicle.	118
Table 5.9. Breakdown of vehicle lift (by force) showing contributions to overall vehicle lift for the baseline thrust efficiency-based objective function vehicle.	119
Table 5.10. Effects of further discretizations on mission specific constraining equations for the Mach 8 to Mach 10 acceleration mission segment.	121
Table 5.11. Effects of further discretizations on a number of variables including fuel usage and exergy destruction plus fuel exergy loss.	122
Table 5.12. Integrated hypersonic vehicle objective function values.	124
Table 5.13. Optimum decision variables for the best performing runs of each objective function.	124
Table 5.14. Mission segment optimum operational variable values.	125
Table 5.15 Optimum vehicle characteristics for each mission segment.	126
Table 5.16. Fuel mass used per mission segment.	131
Table 5.17. Optimum actual mass fractions versus the predicted mass fractions for the integrated hypersonic vehicle.	132
Table 5.18. Mission characteristics for initial and optimal solutions.	133
Table 5.19. Objective function performance.	134
Table 5.20. Samples of results populations for sparse and dense optimal solution spaces.	135

<b>Table 5.21. Decision variable constraint limits before and after range narrowing.</b>	<b>136</b>
<b>Table 5.22. Solutions (initial/optimal), generations (initial/optimal) and computation time for the minimum fuel mass objective function.</b>	<b>138</b>
<b>Table 5.23. Optimum decision variable values for the best performing runs of each objective function.</b>	<b>140</b>
<b>Table 5.24. Failure location of single segment optimized vehicles flown through the entire mission.</b>	<b>142</b>
<b>Table 5.25. Mission segment characteristics and constraining conditions for the high performance mission.</b>	<b>144</b>
<b>Table 5.26. Equivalence ratios and fuel exergy lost per mission segment for the high performance mission exploration.</b>	<b>144</b>

# Nomenclature

$A$	Area, fit parameter	$f_{st}$	Stoichiometric fuel-to-air ratio
$a$	Speed of sound	$g$	Acceleration of gravity
$C_D$	Drag coefficient	$H, h$	Height, enthalpy
$C_L$	Lift coefficient	$H_2$	Hydrogen
$C_p$	Pressure coefficient	$H_2O$	Water
$C_m$	Mixing constant	$h_{pr}$	Fuel lower heating value (LHV)
$C_f$	Skin friction coefficient	$I_{sp}$	Specific impulse
$CR$	Contraction ratio	$ICR$	Internal contraction ratio
$c_p$	Constant pressure specific heat	$L$	Lift, length
$c_v$	Constant volume specific heat	$L_m$	Length for minor mixant to be depleted
$c.g.$	Center of gravity	$M$	Mach number
$c.s.$	Control surface	$M_w$	Molecular weight
$D$	Drag	$m$	mass
$D_h$	Hydraulic diameter	$\dot{m}$	Mass flow rate
$E$	Energy	$MHD$	Magnetohydrodynamics
$Ex, ex$	Exergy	$N_2$	Nitrogen
$F$	Force, streamthrust	$n$	Load factor, step size

$\dot{n}$	Molar flow rate	$U, u$	Velocity
$nm$	Nautical miles	$V$	Velocity
$O_2$	Oxygen	$\forall$	Volume
$P$	Static pressure, power	$W, w$	Weight, work
$Pr$	Prandtl number	$x$	Length, distance
$Q, q$	Heat	$y$	Fuel-to-air axial velocity ratio, mole fraction
$\dot{Q}$	Heat flow rate	$z$	Elevation
$\dot{q}$	Heat flux		
$q_0$	Dynamic pressure	<b>Greek</b>	
$R$	Specific gas constant, range	$\alpha$	Angle-of-attack
$R_c$	Radius of curvature	$\beta$	Oblique shock angle
$Re_x$	Reynolds number	$\gamma$	Specific heat ratio
$r$	Recovery factor	$\delta$	Reference angle, differential amount
$S$	Entropy, planform area	$\varepsilon$	Reaction coordinate, thermo- dynamic effectiveness
$\dot{S}$	Entropy flow rate	$\eta$	Efficiency
$T$	Thrust, static temperature	$\theta$	Deflection angle, flight angle
$T$	Thrust	$\mu$	Kinematic viscosity, Mach angle
$t$	Time, thickness	$\nu$	Prandtl-Meyer function, stoichiometric coefficient

$\pi_c$	Total pressure ratio	$aw$	Adiabatic wall
$\pi_f$	Fuel mass fraction	$b$	Combustion, forebody
$\rho$	Density	$c$	Cowl, chord
$\tau_{wall}$	Wall shear force	$comb$	Combustor
$\varphi$	Equivalence ratio	$cowl$	Cowl lip
$\psi$	Inlet static temperature ratio	$cn$	Cowl extension into nozzle
$\omega$	Elevon deflection angle	$c.v.$	Control volume
		$des$	Destruction
<b><i>Subscripts</i></b>		$diff$	Differential
$0$	Atmospheric conditions, freestream	$elev$	Elevon
$1$	Inlet entrance, initial	$ext$	Extension
$2$	Final	$fb$	Forebody
$4$	Inlet exit	$f$	Friction, fuel
$5$	Combustor entrance	$fric$	Friction
$6$	Combustor exit/nozzle entrance	$g$	Gas
$7$	Nozzle exit	$ht$	Heat transfer
$aero$	Aerodynamic	$inc. comb.$	Incomplete combustion
$avg$	Average	$irr$	Irreversibility

<i>ic</i>	Internal compression	<b><i>Superscripts</i></b>	
<i>M</i>	Mixing	*	Reference conditions
<i>mix</i>	Mixing, mixture	↔	in or out (of a system)
<i>n</i>	normal		
<i>need</i>	Required amount		
<i>nozz</i>	Nozzle		
<i>opt</i>	Optimal		
<i>p</i>	Pressure		
<i>ramp1 (r1)</i>	First inlet ramp		
<i>ramp2 (r2)</i>	Second inlet ramp		
<i>s</i>	Surface, shaft		
<i>surf</i>	Surface		
<i>t</i>	Total, tangential		
<i>vap</i>	Vaporization		
<i>veh</i>	Vehicle		
<i>w</i>	wall		

# Chapter 1

## Introduction

To discuss hypersonic vehicles, generally defined as vehicles traveling above five times the speed of sound, one must examine the fusion of the fundamental disciplines which drove their discovery: aerodynamics and propulsion. Of particular interest, since it is the topic of this thesis work, are the methods which assess the integration and performance of these two systems. Beginning with a basic history of airbreathing propulsion, this chapter summarizes the challenges and promises of hypersonic flight, the motivation for this work specifically, and the goals of this thesis work.

### 1.1 The Evolution of Airbreathing Propulsion

*Airbreathing* refers to the ability of an engine to use the ambient environment (air) as a means for propulsion. For a standard commercial airplane, fuel is stored aboard the aircraft; the air necessary for combustion is pulled through the engine by the turbine. In contrast to airbreathing engines, rockets carry their propellant on board; thus, they are not specifically included in this discussion. Creating an airbreathing vehicle with performance characteristics similar to those of rockets, however, is of great concern and is generally what drives research in the area of hypersonic airbreathing propulsion. Figure 1.1 is a simple illustration of the distinction between airbreathing engines and rockets.

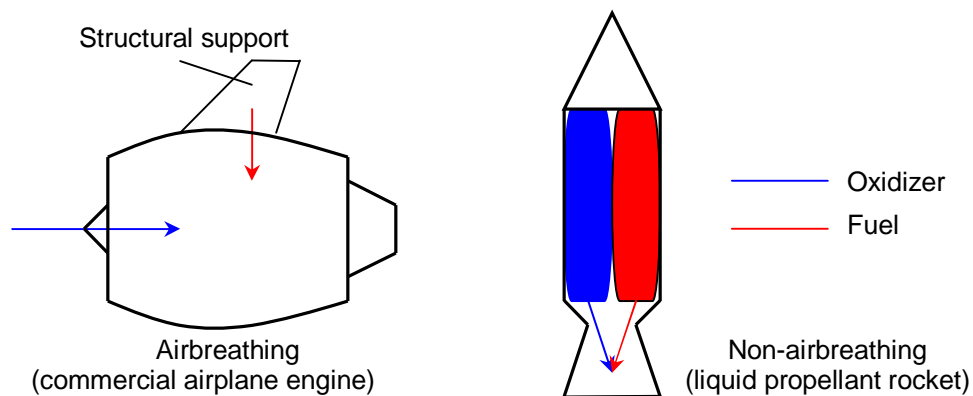


**Figure 1.1.** An illustration of airbreathing and non-airbreathing propulsive devices.

The following discussion surveys the abilities and limitations of historically key airbreathing propulsive devices, their various characteristics, as well as the level of integration between the airframe and engine.

### 1.1.1 Propellers

Arguably the two most influential individuals in the history of aviation, Wilbur and Orville Wright employed the first propellers aboard their 120 foot maiden flight in 1903. Demanding a light and powerful engine, the Wright brothers designed and built their own gasoline internal combustion engine which drove two propellers through a series of gears and linkages. For this reason, the propeller represents the least integrated propulsive device, because it can be independent of the engine which drives it. The engine need only turn a shaft and be flight-worthy (i.e. meet weight and power constraints). In addition, propellers can be located at various locations on the vehicle including the nose, wings, and front or rear of the vehicle. Propellers are the best example of an airbreathing device, as the flow rate of air through them is typically two to three orders of magnitude greater than the flow rate of fuel through the engine [1]. A simple illustration is shown below in figure 1.2.

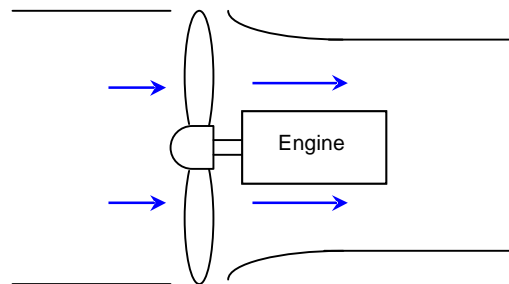


**Figure 1.2.** A propeller creates thrust by accelerating the ambient airflow.

Propellers can maintain high efficiency as long as the airflow through the blades is well behaved. As compressible flow effects become substantial (as the flight Mach number approaches unity), flow near the blade surface becomes disrupted and noise and vibration effects dictate the propeller's top speed. Propellers are most efficient far from compressible flow effects and, thus, are typically employed for speeds below 300 mph (Mach numbers less than 0.4) [1]. Designing propeller blades that can meet the challenges of transonic flight is still continuing today. However, in the late 1930's, when the conventional limits of propeller propulsion had long since been realized, a new type of engine emerged and revolutionized aviation.

### 1.1.2 Turbojets

Simultaneously developed in both England and Germany, turbojets were the solution to the noise, vibration, speed, and altitude limitations of the propeller. A schematic of the turbojet is shown in figure 1.3. The air is decelerated and organized<sup>1</sup> in the diffuser, or inlet, and then proceeds through the compressor, across which the static pressure ratio is greatly increased. Fuel is added, mixed, and combusted in the burner, after which the expansion of the flow through the turbine powers the compressor by way of a rotating shaft. The flow is finally expanded to nearly ambient pressure at a velocity and temperature greater than it entered, thus creating thrust.

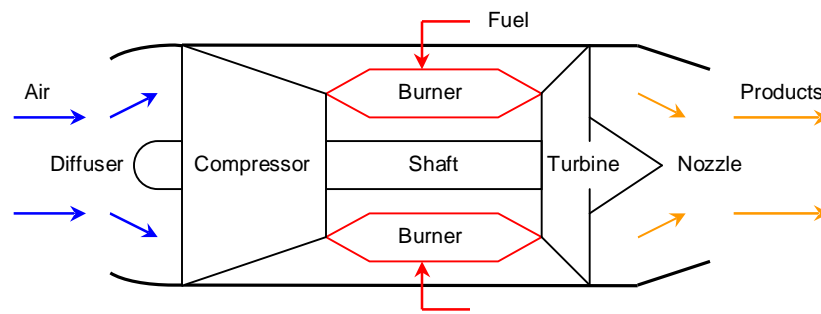


**Figure 1.3.** A generic turbojet engine.

Though the ratio of the flow rate of air to the flow rate of fuel of the turbojet was reduced in comparison to the propeller (now roughly 50), the much higher flow rates and simple, compact design yielded a more reliable engine with much greater thrust per unit mass. This development reduced the cost of air travel by requiring less maintenance, increasing flight speed, range, and altitude, and allowing for the design of larger aircraft. The turbojet also made supersonic flight possible. Variations of the turbojet still power commercial and military aircraft today<sup>2</sup>.

The turbojet also represents a higher order integration of aerodynamics and propulsion. This design was the first to use combustion to heat and pressurize the flow, after which the thrust could be increased through expansion. Though many aircraft configurations incorporate turbojets in the same fashion as propellers, that is, at various locations on the aircraft, military and high performance turbojets are integrated into the body of the craft, minimizing the drag caused by the engines. Figure 1.4 illustrates the synthesis of engine and fuselage.

<sup>1</sup> The ducting of the compressor allows for more control of the air flow at Mach numbers approaching unity, reducing the threat of flow disruption across the blades common in propellers [1].

<sup>2</sup> These variations include, most notably, performance enhancing afterburning and the development of highly efficient turboprops and turbofans.

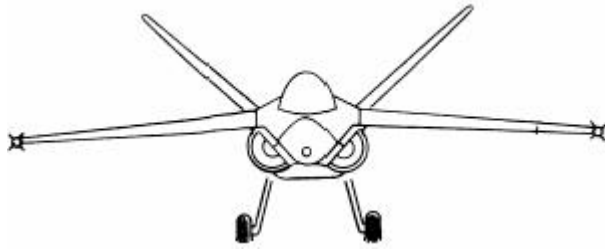


**Figure 1.4.** The synthesis of engine and fuselage in a generic fighter aircraft [2].

The high temperature and centrifugal stresses in the compressor and turbine components create a performance ceiling for the turbojet [1]. In addition, the “ram” compression due to high flight speed is a characteristic that can be exploited in a new type of propulsive device called the ramjet.

### 1.1.3 Ramjets

In 1946, little more than a decade after the turbojet made its first successful flight, the Lockheed F-80 flew on pure ramjet propulsion. Considered the simplest of all airbreathing devices, the ramjet consists of a diffuser, combustion chamber, and nozzle, as shown in figure 1.5. Though illustrated as axially symmetric, this is no longer necessary because the ramjet requires no rotating machinery. In this case, the inlet consists of both supersonic (through a series of oblique shocks) and subsonic compressions. Again, the fuel is subject to subsonic mixing and burning in the combustor. However, flame holders are often required to prevent the flame from extinguishing at high flow rates. The flow is then expanded through a converging-diverging nozzle to accommodate both subsonic and supersonic flows. Again, the high temperature exhaust flow exits at a greater velocity than it entered, thus providing thrust.

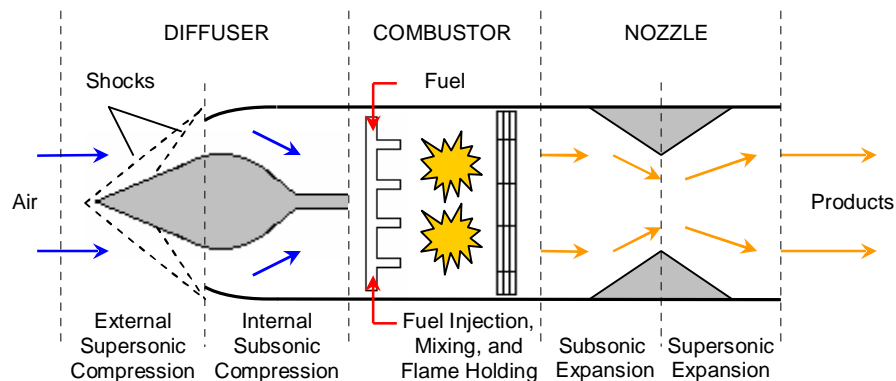


**Figure 1.5.** A generic ramjet configuration.

Representing the highest level of integration, figure 1.6 shows how the forebody and afterbody are used for compression and expansion surfaces in this potential dual mode, European Hypersonic Transportation Vehicle [3]. Dependent on ram air, the ramjet is unable to develop static thrust; thus, a dual mode of propulsion is necessary for missions that begin at takeoff. A ramjet's simplicity of design, low cost of production, and need for a first stage of propulsion make them particularly attractive for military applications, as opposed to human transportation [3].



**Figure 1.6.** A dual mode turboramjet concept. A common diffuser accommodates both the turbojet (top) for low speed flight and the ramjet (bottom) for high speed flight [3].

Just above Mach 6, ramjets reach a performance ceiling. At such high speeds, slowing the air for subsonic combustion ionizes the incoming flow, after which adding fuel no longer raises the flow temperature and prevents complete combustion. The ramjet must then be modified to allow for supersonic combustion, resulting in the method of propulsion that is the topic of this thesis.

## 1.2 Hypersonic Airbreathing Propulsion

With the promise of approaching near earth orbit, scramjets, or supersonic combustion ramjets, offer performance capabilities previously only possible with rocket propulsion. Though scramjets hold much potential, unique challenges await the developers of such aircraft. As a result, the methods by which these designs are assessed become increasingly more significant.

### 1.2.1 Scramjets

Interest in scramjets began in the 1960's. Budgets, testing, and unforeseen technical difficulties have all led to fluctuating development periods for scramjets over recent years. However, advances in materials and technology in general, along with the potential benefits of scramjet aviation, have served to keep the goal of airbreathing hypersonic flight within reach.

As illustrated in figure 1.7, the scramjet shares many similarities with the ramjet, except, of course, that the entire flow path remains supersonic. At such high flight speeds, however, aerodynamic

integration of the engine is vital to the success of the vehicle; consequently, distinguishing airframe-engine boundaries becomes difficult. In fact, the entire lower surface of the aircraft can be considered the engine for the following reasons. For hypersonic flight at high altitudes, it is necessary to reduce drag. However, the low density of air requires a large compression surface (resulting in greater drag), and hence the forebody of the vehicle must be utilized as a diffuser. Similarly, nozzle areas greater than inlet areas are required to produce appreciable thrust. Thus, conventional axisymmetric nozzles become large and impractical, and the afterbody surface must be used for free expansion. The resulting planar geometry introduces aerodynamic effects uncharacteristic of common aircraft. Pressures acting on the compression and expansion surfaces of the inlet and nozzle are greater than the ambient conditions, producing lift and introducing moments about the aircraft center of mass. This lift can potentially render wings obsolete and consequently, further reduces the ability to classify and investigate the engine and airframe separately.

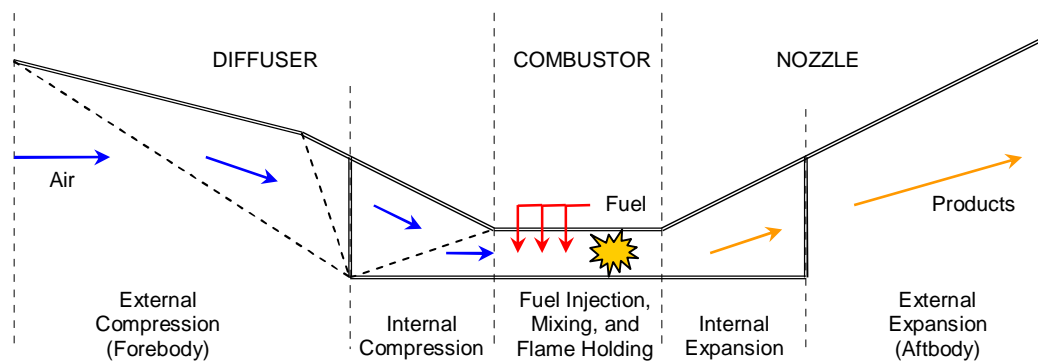


**Figure 1.7.** A generic scramjet engine flowpath.

Examining table 1.1, one can imagine the benefits of an airbreathing vehicle with the performance characteristics of rocket propulsion. The large fraction of rocket weight allotted for oxygen implies that if such a vehicle were airbreathing, that portion could be converted to payload, empty weight, and fuel with many potential benefits. For example, increased empty weight could mean improvements to structure and instrumentation. With more weight for fuel, the possibility of extending vehicle range or performance exists. In addition, current delivery costs can amount to \$10,000 per pound of payload to low earth orbit [3]. Increasing the weight fraction for payload can reduce this cost. Further reductions in cost would result from the likelihood that the entire airbreathing vehicle would be reusable. Furthermore, an airbreathing aircraft capable of takeoff from a traditional airport could

alleviate the need for expensive launch facilities and retrieval missions and consequently, open the door for commercial hypersonic flights.

**Table 1.1.** Typical takeoff weight fraction breakdowns of current aircraft and multi-stage rocket transportation systems [3].

Takeoff Weight Fraction	Aircraft	Rocket
Payload	15%	4%
Empty	55%	7%
Fuel	30%	24%
Oxygen	0%	65%

Though the rewards of scramjet propulsion are great, numerous challenges face engineers attempting to enter the hypersonic age.

### 1.2.2 Hypersonic Challenges

Though the defined boundary between hypersonic and supersonic arenas is not well defined, it is important to note that there is a distinct difference between the two flows, primarily resulting from the high altitudes and high temperatures traversed in hypersonic flight. A few of them are denoted in the following figure.

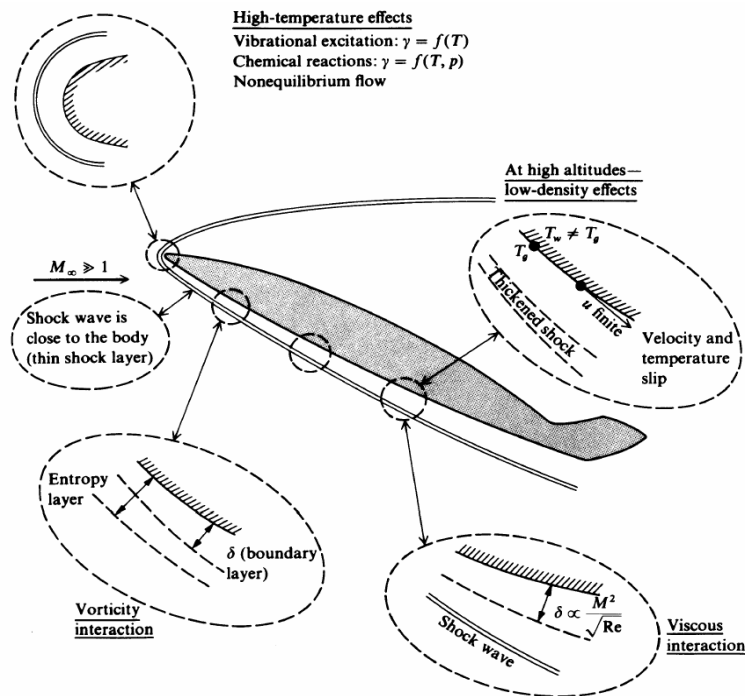


**Figure 1.8.** Physical effects characteristic of hypersonic flow [4].

Thin shock layers and entropy layers characteristic of hypersonic flow provide unique challenges because they both interact with the boundary layer<sup>3</sup>, essentially complicating analytical approaches. Viscous interactions occur where the thick boundary layer meets the outer inviscid flow, intensifying skin friction and heat transfer effects. In addition, these layers affect pressure distributions on the vehicle, thereby influencing lift, drag, and overall vehicle stability. High temperature effects result from viscous interactions by exciting and reacting molecules within the boundary layer, producing radiative heating. These effects can generate temperatures upwards of 11,000°K, making material selection critical [4]. In addition, convective or aerodynamic heating at hypersonic speeds can result in hydrogen embrittlement or oxidation of the structure [3]. Of particular significance to unmanned hypersonic vehicles, communications blackouts can result from ionized flows absorbing radio frequency radiation, making vehicle control another concern. Lastly, low density flows, rarely encountered in typical aerodynamic applications, further complicate design and analysis. Anderson provides a particularly vivid description of the problem of low density flows:

*...when you wave your hand through the air (at 342,000 ft.), you are more able to 'feel' individual molecular impacts; the air no longer feels like a continuous substance, but rather like an open region punctuated by widely spaced particles...[4]*

These variations in flow properties at high altitudes require changes in conventional methods of analysis. For this situation particularly, continuum flow assumptions must be replaced by free molecule flow, greatly changing the governing equations and complicating analyses. Velocity slip, occurring when the viscous no-slip condition<sup>4</sup> fails, and temperature slip, occurring when the material surface temperature and gas surface temperature are unequal, result from low density flows as well.

Ground testing hypersonic vehicles is equally difficult. Generating sustained wind tunnel tests for conditions above Mach 15 has yet to be realized in the literature. Generating such high speed flows has consequences as well. For example, the reflected shock tunnels utilized by Paull and Stalker produce atomic oxygen and nitric oxide, hindering accurate combustion simulation [5]. These speeds also yield temperatures that complicate simple measurement techniques. The melting of measurement devices such as thermocouples and shock interactions at their tips require innovative solutions. In

---

<sup>3</sup> Shock layers merge with boundary layers while entropy layers introduce regions of strong vorticity within the boundary layer [4].

<sup>4</sup> The no-slip condition assumes that the flow velocity at the material surface is zero due to friction.

addition, a lack of information about aerodynamic data and “rules of thumb,” conventionally utilized in subsonic and supersonic vehicle design, further complicate testing.

In essence, the ability to develop analytical tools, materials, and test procedures capable of predicting and operating over a large range of pressures, temperatures, altitudes, and speeds will determine how quickly the benefits of hypersonic airbreathing propulsion can be realized.

### 1.2.3 Recent Milestones in Hypersonic Flight

NASA’s 230 million dollar Hyper-X program began in 1996 with conceptual design work and wind tunnel simulations of a potential scramjet vehicle. Since then, it has twice demonstrated the possibility of hypersonic airbreathing flight. Three X-43A’s were built with differences to simulate a variable geometry combustor. The general vehicle geometry can be seen in figure 1.9. All three X-43A’s were first attached to a Pegasus rocket booster, which was carried to an altitude of 40,000 ft. by a B-52B launch aircraft. The Pegasus rocket then separated and carried the X-43A to its desired speed and altitude, upon which the scramjet detached and accelerated under the power of airbreathing propulsion. Figure 1.10 shows the mission profile of the X-43A.

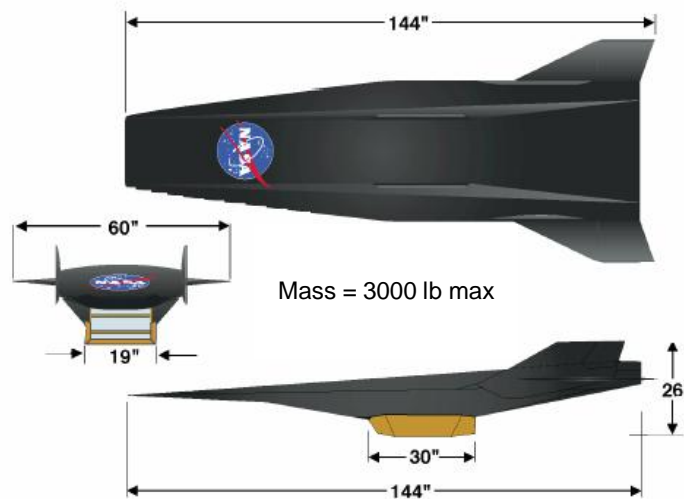


**Figure 1.9.** NASA's X-43A vehicle dimensions [6].

The first X-43A was scheduled to fly in June 2001, but was destroyed by ground crew when the rocket booster, with the test vehicle attached, became unstable during transonic acceleration. The second test flight, in March 2004, successfully maintained flight at Mach 7 for ten seconds of scramjet engine operation. The third and final X-43A accelerated to a flight Mach number of 9.8, reaching nearly 7000 mph. It sustained these conditions for twenty seconds before starting its decent. Perhaps as

important as the demonstration itself is the data collected during the decent segment of the mission. Undoubtedly, this data will be used to improve the analytical tools for hypersonic vehicle design.

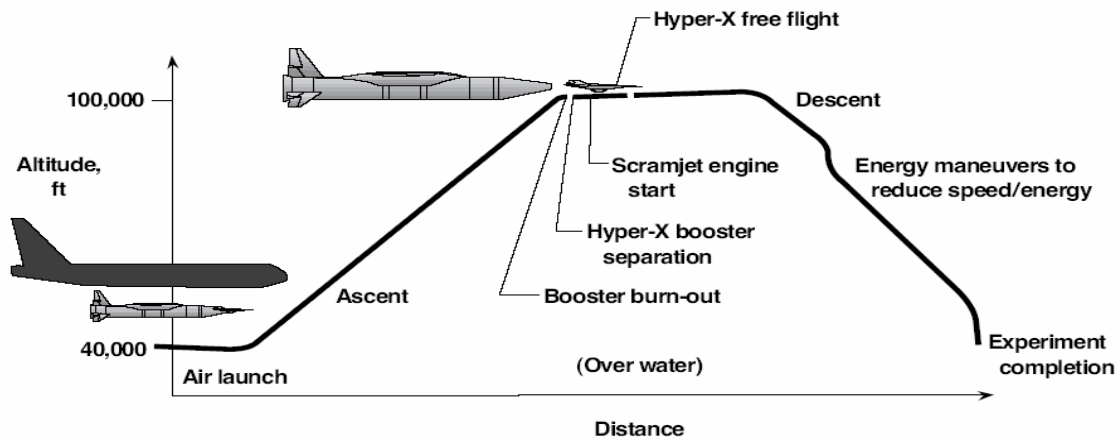


Figure 1.10. NASA's X-43A mission profile [6].

## 1.3 Hypersonic Vehicle Synthesis/Design

As previously shown, the high level of system integration characteristic of hypersonic vehicle concepts introduces the need for a common metric capable of making performance trade-offs between sub-systems. This section is devoted to demonstrating this need and presenting the specific goals of this thesis.

### 1.3.1 An Exergy Based Approach

Common practices in aircraft design rely on the isolation and optimization of individual vehicle sub-systems such as engine and environmental control sub-systems. When a certain vehicle performance is desired, these individually optimized sub-systems are assembled into a final vehicle configuration. However, Muñoz and von Spakovsky have demonstrated that the true optimal synthesis/design and operation can be achieved only by optimizing all components and sub-systems simultaneously [7]. This is significantly more important the greater the need for an integrated synthesis/design is; and, as will be shown, a separate and isolated approach to all aspects of hypersonic vehicle synthesis/design is not feasible. Furthermore, Rancruel and von Spakovsky demonstrated this approach in their large-scale optimization of an advanced air fighter, with 493 degrees of freedom, over an entire mission [8]. Of course, as also shown recently by, for example, Markell [9] and Periannan [10], the choice of evaluation criteria (i.e. objective functions) utilized during the optimization not only

affects the degree of integration and, therefore, the optimum vehicle found but the degree to which a designer is able to understand the integrations which are possible between the fundamentally different sub-systems and processes (e.g., the airframe aerodynamics and the engine propulsion).

In order to deal with this last issue of sub-system and process dissimilarities, a common measure or currency is needed [11]. Such a metric is exergy, which is a *non-conserved property* defined as the largest amount of energy that can be transferred from a system to a weight in a weight process while bringing the system to mutual stable equilibrium with a notional reservoir [12]<sup>5</sup>. For example, airframe drag [14], inlet [15], engine [16, 17], and environmental control sub-system [18] performance can all directly be measured on the basis of irreversibilities, which destroy or consume this non-conserved property called exergy.

Finally, a brief survey of the application of exergy methods and large-scale optimization with decomposition to the synthesis/design and operation of supersonic and hypersonic aircraft is provided in chapter two.

### 1.3.2 Thesis Objectives

Applying an exergy-based approach to the mission-level optimization of a highly integrated hypersonic vehicle and comparing the results with more conventionally-based approaches is the overall objective of this thesis. Specific objectives include the following:

- Develop detailed, quasi one-dimensional computer simulation models capable of capturing vehicle sub-system interactions, their primary loss mechanisms (irreversibilities), and overall flight behavior.
- Define a hypersonic mission encompassing a variety of speeds, altitudes, turns and ranges representative of a sensible hypersonic application.
- Identify and optimize key decision (both design and operational) variables for optimal vehicle synthesis/design and operation based on various evaluation criteria (i.e. objective functions) and specifically examine the usefulness of an exergy-based approach for system-level optimization over an entire hypersonic mission.

---

<sup>5</sup> Note that in the literature, the terms “availability” [13] and “generalized available energy” [12] are used synonymously with “exergy.” This is true up to a point, but the more general of these concepts is the “generalized available energy” of Gyftopoulos and Beretta [12] which includes the other two as special cases.

- Analyze and discuss the resulting optimal combinations of decision variable values and compare mission segment performance for each of the evaluation criteria (e.g., observe, if possible, which mission segment(s) drives/constrains the vehicle design).

Finally, as in any optimization approach, the level of modeling detail directly impacts the results so that the optimal hypersonic aircraft configurations found must be viewed within the context of the models used. However, as indicated previously, the primary goal here is not the development of vehicle configurations but an examination instead of the viability of the methods used. For example, much more work would be required to create high-fidelity models. The optimal configurations found are therefore only of secondary importance and not necessarily conclusive in and of themselves.

## Chapter 2

### Review of Literature

A review of published work is necessary to assess the current state of hypersonic vehicle technologies, develop realistic computational models, and validate results. The primary areas of research pertaining to this thesis are hypersonic vehicle optimization techniques, exergy methods for performance analysis, and system and mission-level energy and exergy methods. All three are briefly examined here.

#### 2.1 Hypersonic Vehicle Optimization

Understanding the synthesis/design challenges and essential components of a conceptual hypersonic vehicle is vital to the successful evaluation of its performance. Of particular importance is how inlet flow modeling is approached and controlled, basic hypersonic vehicle geometries are modeled, and objective functions are utilized to perform an optimization.

##### 2.1.1 Inlet Flow Control

The coupled nature of engine performance and aerodynamic stability in hypersonic vehicles provides an interesting and challenging synthesis/design problem. Arguably the single largest factor influencing hypersonic vehicle performance is the ability to maintain a shock-on-lip vehicle operating condition throughout a wide range of flight operations, a complexity that arises from the intrinsic behavior of shocks. As illustrated in figure 2.1a, the term shock-on-lip refers to the leading edge forebody shock intersecting<sup>6</sup> the cowl lip surface. This condition yields the largest mass capture<sup>7</sup> and flow uniformity vital for combustion. Over- and under-spiced operation, shown in figures 2.1b and 2.1c,

---

<sup>6</sup> In actuality, the shock or shocks converging on the cowl lip create immense local heating, and, therefore, ideally the shocks would converge slightly before the cowl lip where mass capture can remain near optimum [19].

<sup>7</sup> As will be shown in Chapter 3, mass capture is nearly proportional to thrust and, hence, plays a significant role in vehicle performance.

respectively, can lead to, among other complications, inlet unstart<sup>8</sup>, causing catastrophic failure. Therefore, maintaining sufficient inlet flow control is vital.

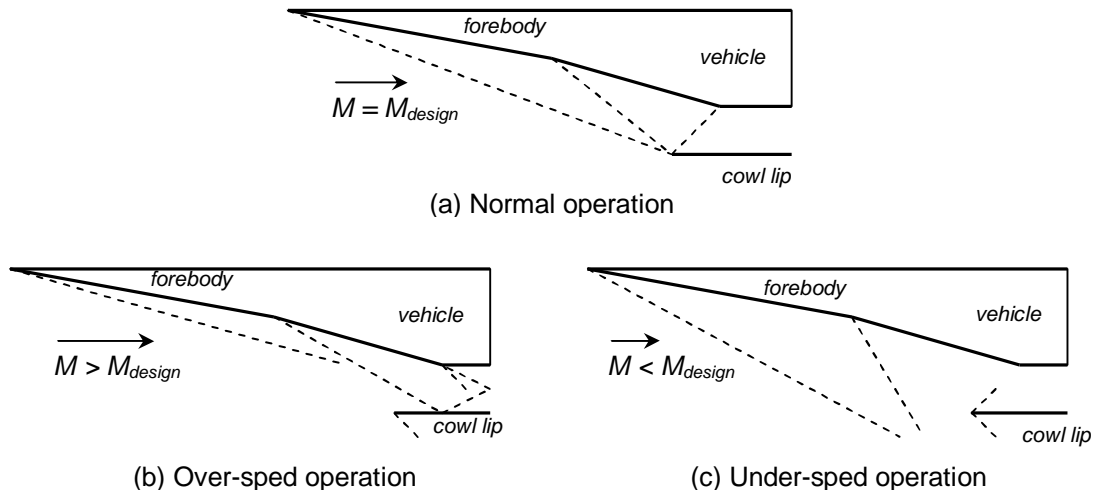


**Figure 2.1.** Inlet flow operational conditions.

Both traditional and innovative techniques have been proposed to meet the challenges of inlet flow control. The method commonly employed for flight control in general aviation is variable vehicle geometry. In a hypersonic vehicle, however, cost, complexity, and weight constraints may render untenable the use of variable geometry configurations to provide the necessary flow control over a range of flight Mach numbers and angles of attack [19]. As a result, much advancement has been made in the modern field of energy distribution. Proposed methods for flow control include mass injection, plasma and magnetohydrodynamics (MHD), and electrostatic fields [20]. The promise of these technologies lies in the potential for the “rearrangement” of energy throughout a scramjet flowpath. For example, an inlet operating at off-design can have energy removed via MHD power extraction to manipulate the local Mach number and locate the shock on the cowl lip. Simultaneously, the power extracted can be redistributed to an area in which it can improve vehicle efficiency, such as at the nose of the vehicle to reduce blunt body leading edge drag. Van Wie and Nedungadi provide an excellent review of the current state of many MHD technologies in [21]. Figure 2.2 shows several problems and possible solutions utilizing plasma-based technologies. Camberos et al. [22] have developed methods for quantifying the irreversible losses (exergy consumptions) due to MHD flow - an essential step toward

<sup>8</sup> Inlet unstart occurs when the flow Mach number approaches unity at the entrance to the combustor, after which the flow becomes subsonic, causing a critical condition from which a supersonic combustor cannot recover.

the integration of a plasma-assisted system into a multi-disciplinary, exergy-based synthesis/design methodology.

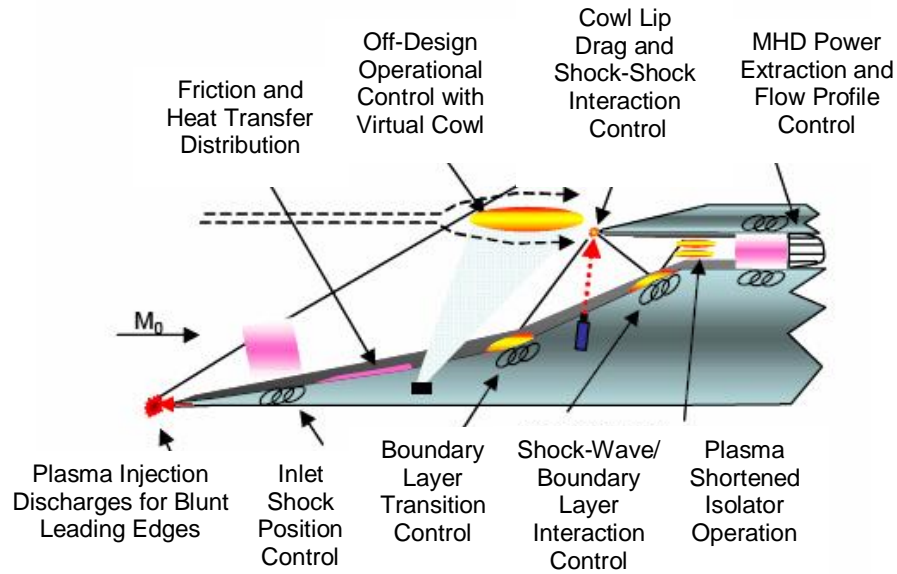


**Figure 2.2.** Potential inlet flow control methods using plasmas [21].

Other interesting energy addition applications have emerged as well. Taylor and Riggins [23] describe the possibility of utilizing electro-magnetics and ionization on mixing and combustion in scramjet combustors. Preliminary computational results indicate opportunities for reduced combustor length and increased performance without large increases in entropy generation (irreversibilities/exergy consumption). Schneider et al. [24] have described the possibility of vehicle control by way of upstream, off-axis heat addition. The deposition of energy causes an asymmetric pressure distribution, indicating that vehicle steering and lifting moments can potentially be created.

New technologies will undoubtedly play an important role in the development of hypersonic vehicles. However, the actual implementation of these elements requires further development, testing, and analysis before their advantages can be fully realized.

### 2.1.2 Vehicle Configurations

The following discussion surveys vehicle configurations in an effort to reveal key decision (both synthesis/design and operational) variables for a multi-disciplinary approach to hypersonic vehicle synthesis/design, as well as investigate the need for a mission-level optimization.

Bowcut [25] expressed the need for a coupling of aerodynamic and propulsive forces in the hypersonic arena. Therefore, he applied a synthesis/design technique to demonstrate hypersonic vehicle optimization with the basic vehicle parameters defined in figure 2.3. After identifying these key parameters, summarized in table 2.1, performance models were developed and an optimization tool was employed to maximize a particular objective function for two prospective hypersonic vehicles: a Mach 15 cruise and a Mach 15 acceleration vehicle.

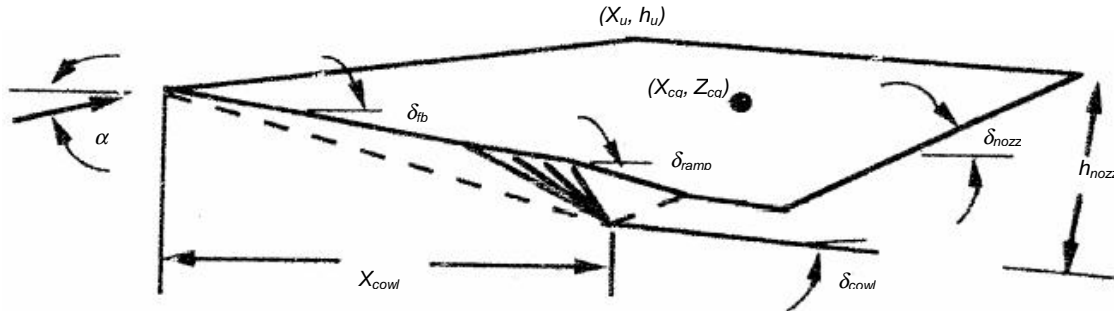


Figure 2.3. Vehicle defining parameters [25].

Table 2.1. Bowcut's selected geometric parameters [25].

Nomenclature	Description	Acceleration Optimized Values	Cruise Optimized Values
Independent (Decision) Variables			
$X_{cowl}$	Axial cowl lip location (ft.)	64.80	53.97
$\delta_{fb}$	Forebody compression angle ( $^{\circ}$ )	6.76	6.97
$\delta_{ramp}$	Isentropic compression ramp angle ( $^{\circ}$ )	34.62	22.13
$\delta_{cowl}$	Engine cant angle ( $^{\circ}$ )	3.65	4.27
$\delta_{nozz}$	Nozzle average angle ( $^{\circ}$ )	14.81	8.17
Dependent Variables			
$h_u$	Body bump height (ft.)	1.33	1.11
$S_w$	Wing size (ft. <sup>2</sup> ) (not shown)	0	0
$\delta_{elev}$	Elevon deflection angle ( $^{\circ}$ ) (not shown)	-1.90	-0.06

A fixed vehicle planform with a length of one hundred feet and width of twenty feet was established as the baseline. The planar volume shown in figure 2.3 is conserved by means of a bump coordinate ( $X_u, h_u$ ). The flowpath analysis consists of five performance models: inlet, combustor, nozzle, wing, and elevon. The inlet model utilizes dual shock (denoted by the dotted lines in figure 2.3) and isentropic ramps for ideal gas compression. The combustor solves quasi-one-dimensional conservation of mass, momentum, and energy equations with a frozen gas treatment for unburnt hydrogen fuel. Ideal expansion is assumed for the nozzle, and wing and elevon models balance vehicle

forces (i.e. lift equal to weight) and moments to provide stable, level flight. Equations (2.1) and (2.2) show the respective objective functions to which the acceleration and cruise vehicles were subjected,

$$I_{sp\text{eff}} = \frac{T - D}{g\dot{m}_f} \quad (2.1)$$

$$\frac{L}{D} I_{sp} = \frac{L}{D} \frac{T}{g\dot{m}_f} \quad (2.2)$$

where the specific impulse ( $I_{sp}$ ) is a function of thrust ( $T$ ), drag ( $D$ ), gravitational acceleration ( $g$ ), and the mass flow rate of fuel ( $\dot{m}_f$ ). Maximization of equation (2.1) minimizes the propellant fraction necessary to accelerate the vehicle to a desired velocity, while maximization of equation (2.2), with respect to all five decision variables, maximizes the range of the vehicle based on the lift to drag ratio,  $L/D$ . In addition to these optimizations, Bowcutt also optimizes each of the five decision variables separately and compares the resulting effective specific impulse objective functions to that of the multi-disciplinary outcome, i.e. the optimizations with all five variables (shown in table 2.1).

The multi-disciplinary optimizations resulted in two very different geometries for the two optimization objective functions. This dissimilarity implies that synthesizing/designing a vehicle capable of performing efficiently for combined cruise and acceleration mission segments may indeed be challenging. In addition, the multi-disciplinary approach yielded an effective specific impulse forty-one percent greater than the next highest single variable optimization result. Here the benefits of employing a synthesis/design methodology are realized. In essence, Bowcutt’s study provides many valuable insights on hypersonic vehicle performance dynamics and optimization.

In a second hypersonic study, Hendrick [26] compared the ability of energy and exergy analyses to evaluate the effect of inlet contraction ratio on the fixed geometry hypersonic vehicle configuration in figure 2.4. Hendrick utilized a quasi one-dimensional approach with real gas

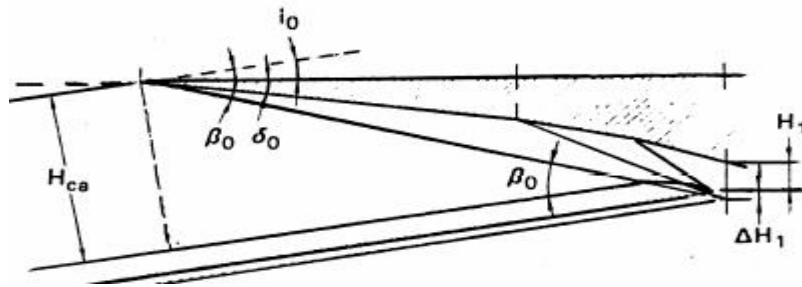


**Figure 2.4.** The fixed geometry inlet model used by Hendrick [26].

aerothermodynamics including contributions from shocks, skin friction, and heat transfer to model his 50 meter, Mach 15 accelerator vehicle. The model employed a fixed geometry, three-shock diffuser with forebody and ramp shocks. The goal of this study was to determine the optimum combustor entrance pressure at a Mach 15 flight condition, which essentially meant finding the optimum cowl lip height,  $H_l$ , that resulted in the optimum contraction of the ambient flow,  $H_{ca}/H_l$ . To make these calculations, both specific impulse and the propulsive efficiency were maximized. The latter is given in equation (2.3) below.

$$\eta_p \equiv \frac{\text{propulsion power}}{\text{fuel injected power}} = \frac{I_{sp}V_0}{Q_c} \quad (2.3)$$

Here,  $V_0$  is the flight velocity and  $Q_c$  is the fuel heat of combustion for hydrogen, and the efficiency represents the ratio of the vehicle's realized to potential power. Hendrick furthermore examined the effect of angle of attack on specific impulse (energy based analysis) and lost work (exergy based analysis), where the lost work,  $\Phi$ , is defined as a function of the heat transfer temperature and irreversibilities in the system, i.e.

$$\Phi \equiv \text{Lost work} = T^* S_{irr} \quad (2.4)$$

and

$$S_{irr} = -Q \frac{\Delta T}{T^2} + \frac{C_f m_a V^2}{2R_h T}, \quad (2.5)$$

where the first term in the summation of equation (2.5) represents irreversibilities due to heat transfer and from the flow to the hydrogen fuel, which acts as both propellant and heat sink. The second term, representing the irreversibilities due to skin friction, is a function of the surface smoothness, geometry and general flow properties.

Shown on the following page in figure 2.5a, both specific impulse and propulsive efficiency measures produce nearly identical values for the optimum combustor entrance pressure. Similarly, figure 2.5b shows that the specific impulse maximization and lost work minimization converge on the same optimum angle of attack. Again this study illustrates the highly coupled nature of propulsive and aerodynamic forces and provides motivation for pursuing the usefulness of a second law approach to hypersonic vehicle optimization. The results also indicate that a translating cowl or some other flow diffusion manipulation device could provide performance benefits for multiple mission segments.

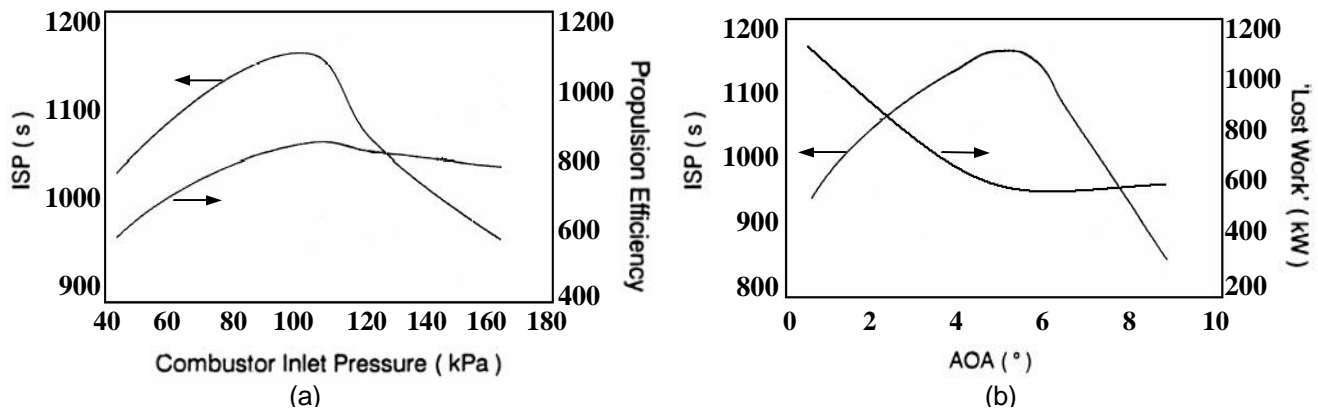


**Figure 2.5.** The effect of energy and exergy performance measures on optimization for (a) combustor inlet pressure and (b) angle of attack [26].

A few authors have suggested using unconventional periodic flight trajectories to minimize fuel use over a particular mission [27-29]. One in particular performed by Starkey et al. [27] examine a multi-disciplinary design approach to the optimization of a Mach 10 cruise vehicle. In this study, a parallelized evolutionary algorithm minimizes fuel use over one standard steady-state and two periodic trajectory cruises. The periodic cruises consist of a range,  $R$ , traversed in a single cycle of the period by a powered and glide phase as shown in figure 2.6 [27].

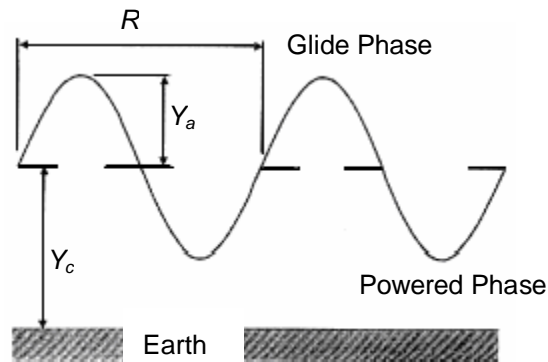


**Figure 2.6.** A periodic hypersonic cruise trajectory [27].

In the periodic case, the “cruise” label is somewhat misleading because the vehicle actually traverses a range of Mach numbers, dynamic pressures, equivalence ratios, and angles of attack throughout its periodic trajectory. For traditional cruise missions, these values remain relatively constant. The optimization process occurs in two stages. First, the vehicle is optimized for a Mach 10

design point after which the trajectory optimization program minimizes the mass flow rate of fuel over the range flown.

Similar to Bowcutt, Starkey utilizes a hypersonic vehicle model with four sub-systems: inlet, combustor, nozzle, and airframe. The engine sub-system<sup>9</sup> consists of a quasi-one-dimensional flowpath including a ten-species, twenty-reaction, variable area combustor with mixing profile and injection model for hydrogen fuel. Also captured are the effects of heat transfer and friction. Again, the nozzle is considered unreacting, and is modeled by the two-dimensional method of characteristics. Twenty-two design decision variables define the vehicle geometry whose total mass is scaled through the use of a uniform mass density assigned to a baseline configuration. Many of these variables are shown in figure 2.7.

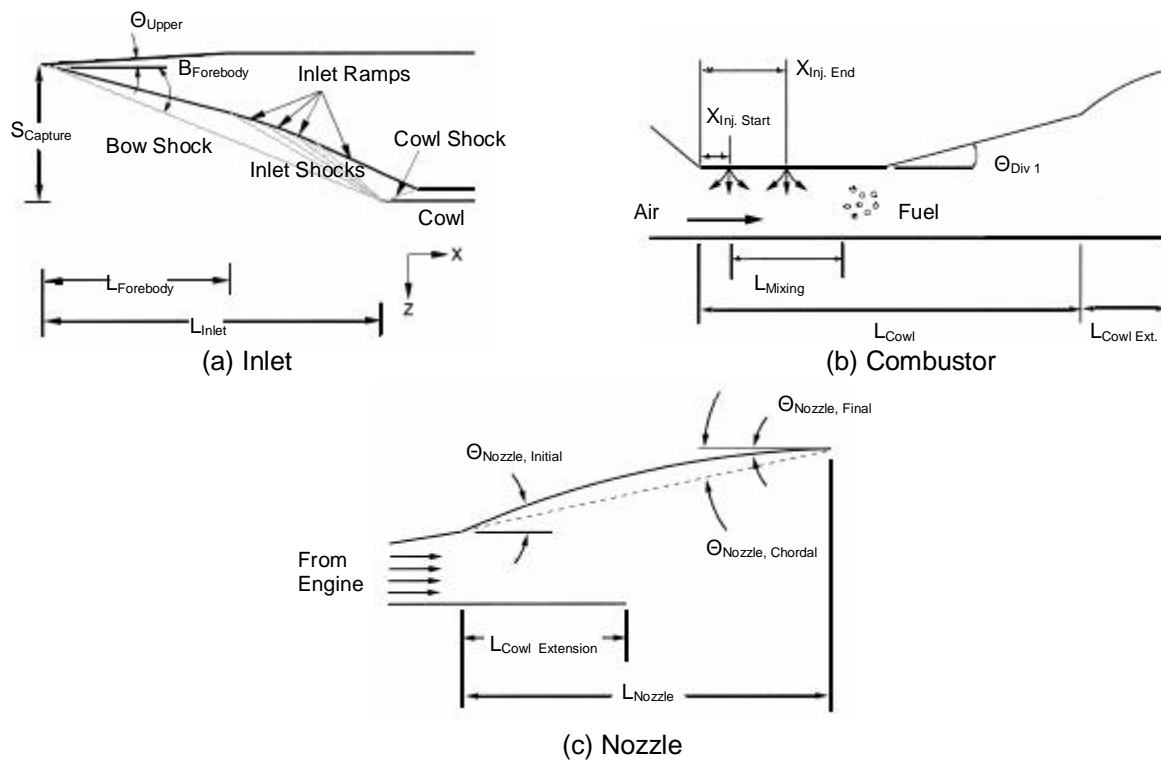


**Figure 2.7.** Hypersonic vehicle configuration and design variables [27].

First, the vehicle optimization is performed after which off-design data is fed into the trajectory optimization program. The first utilizes a standard, steady state cruise trajectory with the engine always on. The second employs one cycle of a periodic trajectory, Per1, with the engine allowed to cycle on

<sup>9</sup> In this case, the inlet, combustor, and nozzle compose the engine sub-system.

and off (with fixed equivalence ratio) once as chosen by the optimization. The final optimization as well is composed of a single cycle of a periodic trajectory, Per2, also with a fixed equivalence ratio but with unlimited engine on/off cycling allowed. The result of this study shows that the Per1 trajectory is capable of providing the same fuel economy as the standard cruise trajectory, while the Per2 trajectory performed significantly worse. Another interesting result is that all three optimizations chose to perform at Mach numbers at the upper limit of the allowable range - nearly Mach 13. This shows the tendency of the optimization is to over-speed the vehicle, that is, to drive it away from its actual Mach 10 design flight condition by increasing the angle of attack, which thereby increases mass capture area and, hence, provides a larger thrust per flow rate of fuel. For future studies, Starkey et al. are generating results for a parallel vehicle geometry/trajectory optimization, which will likely have many interesting implications for the standard mission profiles in use today.

Finally, these works indicated which geometric design parameters are currently considered the most important for the performance evaluation of hypersonic vehicles. Furthermore, the opportunity for carrying out hypersonic mission-level performance evaluations emerges since in the literature current optimization approaches tend to focus exclusively on single mission segments.

## **2.2 Exergy Methods for Vehicle Performance Evaluation**

The second half of the literature review examines the role exergy has played as an analytical tool in recent studies, and specifically, to what extent it has been explored in the realm of high performance aircraft. Throughout this section, the appeal of an exergy approach is presented with results validating the argument for constructing a unifying methodology based on exergy for vehicle design.

### **2.2.1 Exergy Analyses of Scramjet Engines**

The first applications of exergy analysis to hypersonic vehicles dealt specifically with their engines. As it is a highly integrated vehicle and component boundaries are not well defined, this can refer to a combination of inlet, combustor, and nozzle, or strictly the combustor. As a result, many investigations have revealed information regarding performance measures, general trends in hypersonic vehicles, and design considerations, and are hence discussed here.

Brilliant [30] applied an exergy analysis to a scramjet engine in order to evaluate the benefits of such an approach. For these studies, Brilliant selected a baseline vehicle and measured performance from Mach 7 to Mach 25. His model incorporated inlet, combustor, and nozzle components and was designed for a Mach 25 design point flown along a constant dynamic pressure trajectory of 50,000 Pa. A forebody and inlet ramp, five and ten degrees, respectively, compress the flow. Though designed for Mach 25, the inlet utilizes varying inlet contraction ratios, effectively reflecting a variable geometry inlet. The inlet model incorporates losses due to wall cooling, friction, and shocks which occur during the compression process. The combustor, adding hydrogen fuel at a fixed equivalence ratio of one to the air from the inlet, simulates both finite rate and equilibrium combustion processes with and without friction and heat transfer. Five percent of the hydrogen is assumed to be frozen in order to simulate a ninety-five percent combustion efficiency. Above Mach 10, the combustor geometry is constant; and, below Mach 10, it diverges to maintain supersonic combustion. The nozzle component allows for frozen and equilibrium chemistry as well as a combined expansion process. Losses captured in the nozzle are a function of stream thrust efficiency (an energy-based measure) and are converted to irreversibilities via an approximation. The nozzle exit to inlet area ratio is 1.7, and the flow expands according to the nozzle geometry unless ambient pressure is reached before the end of the nozzle at which point an ambient exit pressure is assumed. A few of the observed trends and important results are summarized below [30].

- The inlet losses increase with Mach number though the decrease in exergy of the incoming air due to wall cooling are not completely lost<sup>10</sup>, since the fuel is preheated as a result..
- The total exergy at the combustor exit increases with the amount of hydrogen which is unreacted at the exit (frozen). This result seems at first glance misleading but indeed reflects the fact that the larger the amount of unreacted hydrogen, the less exergy can be realized as thrust: combustion reduces the potential of the fuel.
- As expected, frozen nozzle expansion modeling underestimates nozzle performance since additional thrust cannot be realized.
- As the Mach number increases, irreversibilities in the nozzle increase rapidly. This is due to gaseous dissociation as higher temperatures and pressures are produced in the combustor.

---

<sup>10</sup> Some irreversibilities are generated due to the fact that energy is transferred across a finite temperature difference.

- When both wall cooling and heat transfer effects are included, the sum of the losses result in slightly less exergy destruction than when each are examined individually and then combined, indicating some level of non-linearity/coupling effect.
- The baseline engine cannot produce thrust at Mach 25 when the nozzle has any losses.

This comprehensive work provides many valuable insights into hypersonic engine operation, design considerations, and even potential performance limitations. At its conclusion, Brilliant suggests performing a mission-level, fully integrated system optimization to examine how component trade-offs impact vehicle performance, to specifically minimize the exergy used in the form of fuel.

Riggins defined an engine thrust effectiveness, which essentially referenced the thrust produced to the maximum possible thrust if no irreversibilities were present. This was necessary because earlier exergy applications, referenced to a thermodynamic dead state<sup>11</sup>, resulted in an over-prediction of optimal combustor length where the optimal length was defined as the distance at which the largest net thrust is realized. The two equations for the rational efficiency,  $X$ , and thermodynamic effectiveness,  $\eta_{ee}$ , are given in equations (2.6) and (2.7), respectively. The rational efficiency is a function of heat released ( $Q_{released}$ ), heat expended ( $Q_{expend}$ ), and the dead state velocity ( $u_0$ ) and temperature ( $T_0$ ), while the engine thrust effectiveness is a function of engine mass flow rate through the engine ( $\dot{m}$ ), nozzle exit velocity ( $u_e$ ), pressure ( $P_e$ ), and area ( $A_e$ ), as well as their respective dead state counterparts, denoted by the subscript “0.” Equation (2.7) physically captures the actual to ideal momentum change across the engine [31].

$$\Psi(x) = \frac{\int_0^x \delta Q_{released} + \frac{u_0^2}{2} - \int_0^x T_0 ds}{\Delta Q_{expend} + \frac{u_0^2}{2}} \quad (2.6)$$

$$\eta_{ee} = \frac{\dot{m}u_e(x) + P_e(x)A_e - (\dot{m}u_0 + P_0A_0)}{\dot{m}u_{e_{ideal}} + P_{e_{ideal}}A_e - (\dot{m}u_0 + P_0A_0)} \quad (2.7)$$

Equation (2.6) is an exergy-based measure because the numerator represents the change in actual flow exergy across the engine while the denominator is directly proportional to the chemical exergy of the fuel. Equation (2.7) represents a pseudo-exergy-based measure since it refers to the ideal change in

---

<sup>11</sup> Reference state or state of the “notional reservoir” used to determine the value of the exergy for a given state [12].

momentum across the engine to an ideal change, i.e. one without any irreversibilities or exergy destruction.

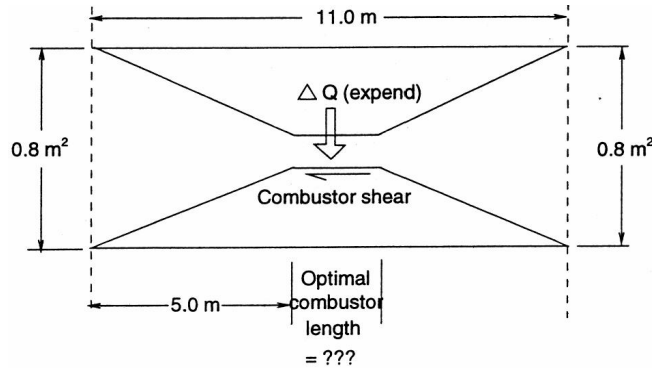


Figure 2.8. Simple scramjet engine model [31].

To determine the usefulness of these measures, they were applied to determining the optimal combustor length of the simple scramjet engine shown in figure 2.8 [31]. In this study, an isentropic inlet and nozzle contract and expand the flow, respectively, through an area ratio of twenty. The perfect gas, one-dimensional flow is subject to Rayleigh heating and a high coefficient of friction within the combustor where heat released from the fuel is a function of distance such that a constant combustion efficiency results.

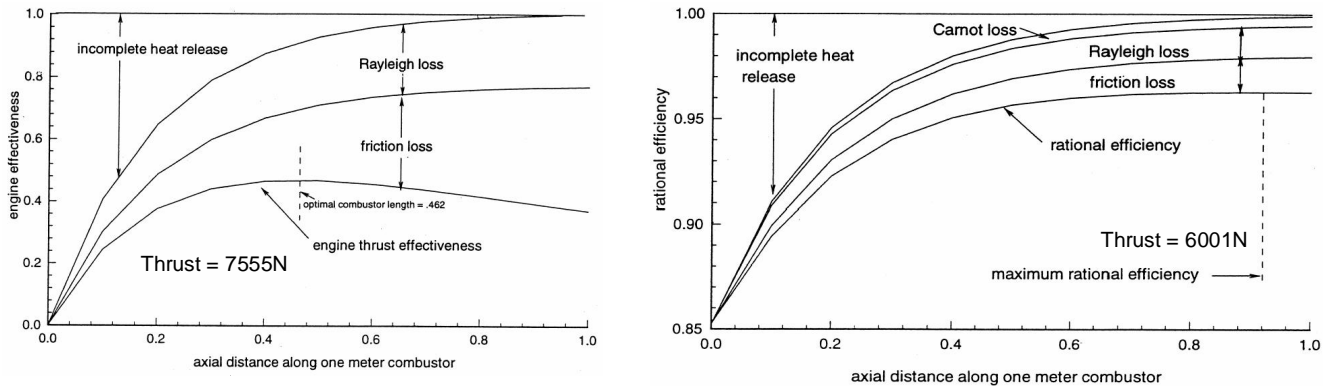


Figure 2.9. Effectiveness parameters vs. combustor length [31].

The results of the optimization for both measures appear in figure 2.9 where it is obvious that the optimum produced by maximizing the engine thrust effectiveness is significantly better than that produced by the rational efficiency. The implication is that the exergy approach as represented by the rational efficiency may not be as useful as the pseudo-exergy approach represented by the engine thrust

effectiveness. However, the problem here lies in the specific exergy measure chosen and not in the exergy approach in general.

To illustrate this last point, Markell, Brewer, and von Spakovsky [32] used the thermodynamic effectiveness along the combustor length which references the thermodynamic dead state as well and is defined as

$$\varepsilon(x) = 1 - \frac{T_0 s_{irr}(x)}{\delta Q_{release}(x) \left( 1 - \frac{T_0}{T_t(x)} \right)}, \quad (2.8)$$

which is a function of dead state temperature ( $T_0$ ) and engine irreversibilities ( $s_{irr}$ ), heat released ( $Q_{release}$ ), and engine total temperature ( $T_t$ ) each as functions of axial position along the combustor. This measure was used to determine the optimal combustor length of a simple scramjet engine similar to the one depicted in figure 2.8. Plots of the results for the thermodynamic effectiveness as well as those for Riggins' engine thrust effectiveness are given in figure 2.10. As can be seen, with this new exergy measure the choice of dead state does not effect the optimal combustor length, which differs from the rational efficiency in figure 2.9. The choice of dead state does, however, affect the relative value of the thermodynamic effectiveness which, of course, is to be expected since the effectiveness value is measured relative to a given reference, i.e. dead state. Nonetheless, the same optimum thrust and combustor length are effectively found with either of the effectivenesses presented above (see figure 2.10).

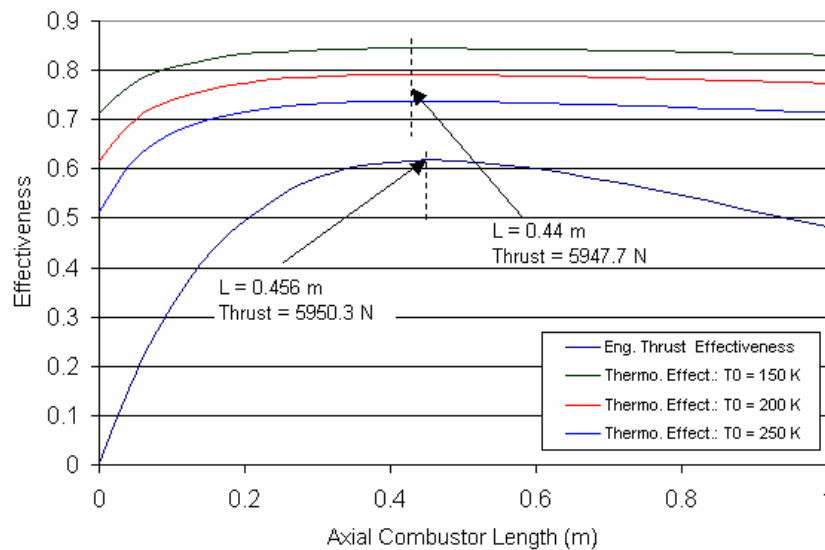


**Figure 2.10.** Engine thrust effectiveness and thermodynamic effectiveness vs. combustor length [9].

Figliola and Tipton utilize both an energy and exergy-based approach for the optimization of an aircraft environmental control system (ECS) [18]. The energy-based approach minimizes vehicle gross takeoff weight as the objective function, while the exergy-based analysis minimizes entropy generation within the ECS. The energy analysis consisted of varying the heat exchanger effectiveness and size, and ECS coolant flow rate to minimize gross takeoff weight. The avionics box, compressor, expansion valve, pumps, and heat exchangers are all evaluated in the exergy analysis and each of their contributions to entropy generation are examined and summed. Again, an exergy approach was suspected to be advantageous over the energy approach because minimizing the losses (entropy generation) in the system could provide both an optimal solution and an indication of the location and magnitude of such losses.

The results of both optimizations provided similar solutions. As suspected, Figliola and Tipton showed that the results of the entropy generation study provide much more insight into the operational aspects of each component. In essence, all components of the ECS generate entropy and impact fuel weight (which affects gross takeoff weight); however, where an expansion valve only indirectly impacts fuel usage (it does not itself consume fuel), and exergy balance on the valve can provide an exact computation of the entropy generated and thus provide a means to evaluate its impact on overall vehicle performance. Only in the latter can exact tradeoffs on vehicle performance be addressed.

Roth [33] and Roth and Mavris [34] present a typical or classical analysis method commonly used in cycle technology trade-off studies and an exergy analysis. The latter is used to create a unified method of evaluation for all aspects of vehicle synthesis/design. Specifically, the authors recommend its use to quantitatively assess the potential benefits of new technologies in highly integrated systems. The motivation for such an approach is summarized in the following excerpt:

*All vehicles must obey the same laws of physics and are subject to the same physical limitations. Given this situation, there must be a common thread of analysis applicable to all classes of vehicle..., and it should be possible to formulate a generalized theory of vehicle design based on these fundamental principles. [33]*

Roth and Mavris describe how losses anywhere in the vehicle can be traced back to fuel exergy consumed in order for a vehicle to operate. As a result, since every component of a vehicle has associated losses, every component must consume fuel exergy to overcome these losses, and being able

to measure the magnitude of such losses and their impact on system level performance is a highly useful tool. Hence, a unifying figure of merit emerges in the form of chargeable fuel weight.

As an illustrative example of the above loss management techniques, the authors examined how a Northrop F-5E aircraft with J85 engines performed at various cycle pressure ratios (OPR) and turbine inlet temperatures (TIT), two defining parameters of engine performance. Using performance data from the manufacturer, the F-5E is flown (by computational simulation) through an appropriate subsonic intercept mission encompassing combinations of takeoff, acceleration, climb, cruise, combat, loiter, and landing mission segments. In classical vehicle evaluation, these data are then resolved into the carpet plot shown in figure 2.11. The results of the plot show that for higher values of OPR and TIT, the vehicle requires less fuel to complete the described mission, which is a valuable result. However, the data reveal nothing about the magnitude or location of the losses in the engine or other components (i.e. how close they are to ideal), making the contribution of a specific technology difficult to determine. A net positive or negative impact can be observed, but what performance trade-offs occur among vehicle components that result in this net impact are not obvious.

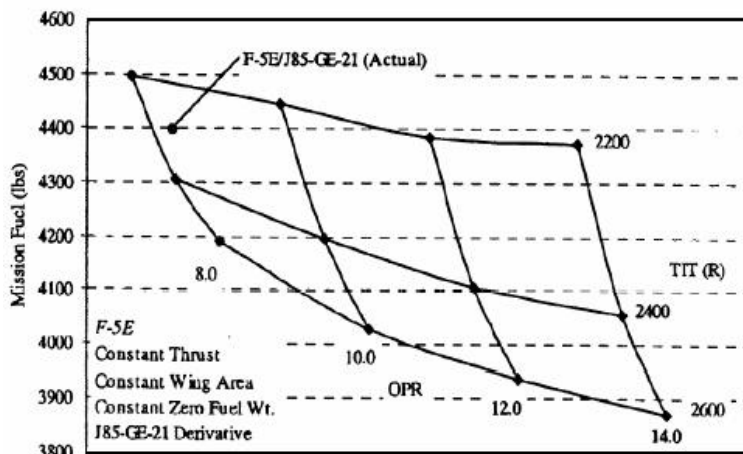


**Figure 2.11.** Carpet plot for sized mission fuel weight as a function of OPR and TIT for the F-5E with J85 derivative engines [33].

Here the appeal of an exergy analysis emerges. A “loss deck” developed by the author provides information of exergy usage across all components during the vehicle mission simulation previously mentioned. This exergy use can be translated into fuel consumed, and consequently, a new performance plot can be created on the basis of chargeable fuel weight (see figure 2.12). In this figure, exactly how

each piece of the aircraft system affects fuel use, as well as the interaction between them, can be seen. Though the figure shows the chargeable fuel weight over the entire mission, Roth and Mavris also analyze individual mission segments, providing behavioral information at that level as well.

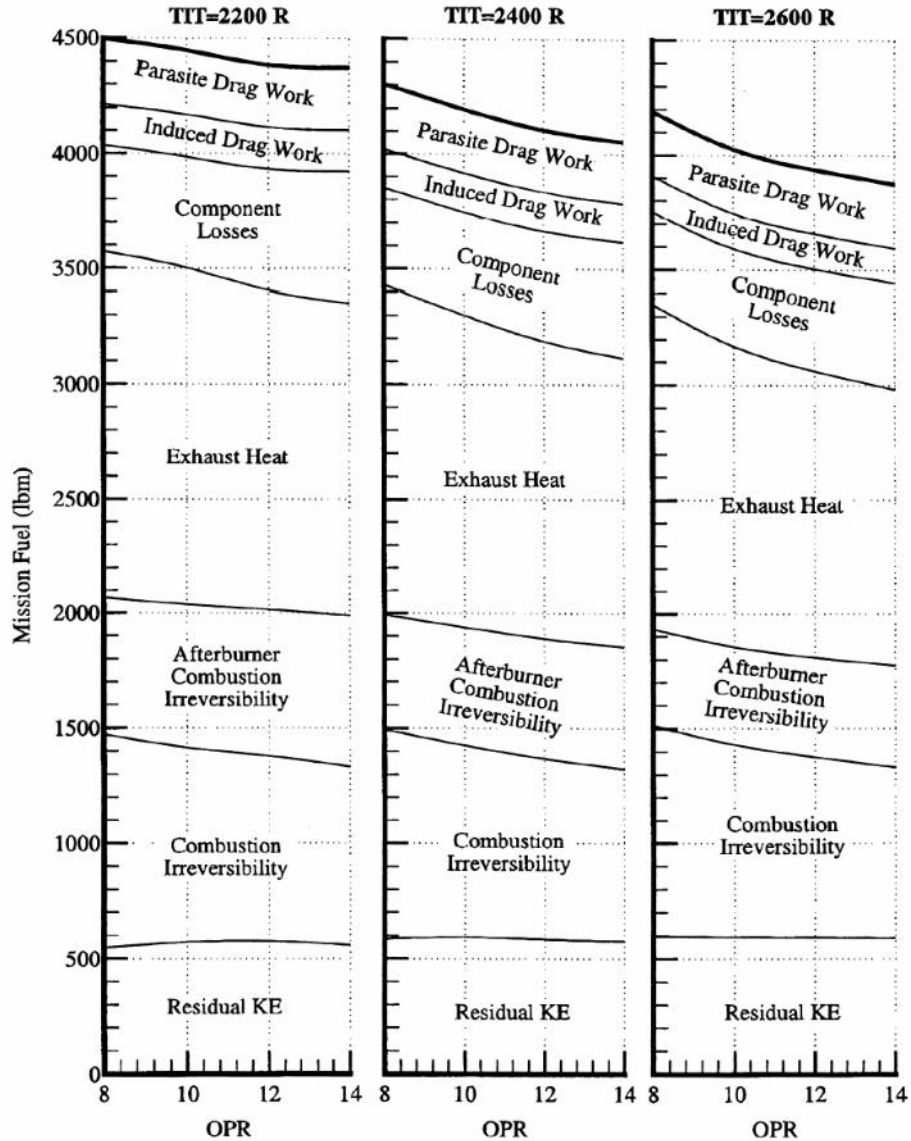


**Figure 2.12.** Chargeable fuel weights for an F-5E subsonic area intercept mission as a function of OPR and TIT [33].

An important result of this work is that exergy methods provide a “common currency” for trade-offs between dissimilar technologies: propulsive, component and airframe. This plot reveals that the primary source of loss in the mission is due to the propulsion sub-system. In addition, technology trade-offs become visible. For example, the net decrease in chargeable fuel weight as OPR increases is due primarily to the reduction in propulsion losses and results even though the component losses tend to

increase. In essence, Roth and Mavris show how identifying and quantifying these losses in a unified manner provides a highly useful tool for vehicle design.

Markell performed a parametric study on the same hypersonic vehicle model used in this thesis work to gain insight into the relationship among the design decision variables, specific exergy destruction, specific thrust, and other performance measures [9]. Table 2.2 shows the eight decision variables and the selected ranges of study. For this study, two of the design decision variables are studied at a time while the others are fixed at the values given in the table, while a Mach 9 flight condition is imposed. The forebody position and cowl position design decision variables were not varied because only very small changes in their values resulted in viable aircraft geometries (in combination with the other variables) and no observable trends resulted. This is yet another indication of the highly coupled challenge of hypersonic vehicle design.

**Table 2.2.** Decision variable fixed values and ranges for Markell’s parametric study [9].

<b>Design Variable</b>	Forebody Position ( $X_{fb}$ )	Cowl Position ( $X_{cowl}$ )	First Ramp Position ( $X_{ramp1}$ )	Forebody Angle ( $\theta_{fb}$ )	Angle of Attack ( $\alpha$ )	Nozzle Expansion Angle ( $\theta_{nozz}$ )	Combustor Length ( $L_{comb}$ )	Percent Nozzle Cowl Length ( $\%_{cowl}$ )
<b>Fixed Value</b>	8.4	13.5	2.75	2.0	1.0	18.0	0.5	0.125
<b>Range</b>	—	—	2.7 – 3.5	1.75 – 6.25	—	8.0 – 18.0	0.5 – 1.5	0 – 0.25

Two of Markell’s results are given in figures 2.12 and 2.13. In figure 2.12, inlet forebody angle,  $\theta_{fb}$ , and the first inlet ramp length,  $X_{ramp1}$ , are varied to observe the effect on specific exergy destruction and specific thrust. The plot shows that for a given ramp length, the maximum specific exergy destroyed and maximum specific thrust do not coincide at a single forebody angle, nor do they illustrate a linear relationship, indicating the need for optimization. Furthermore, there are multiple combinations of forebody angle and first ramp length that can produce a selected value of specific thrust, though a single combination destroys the least specific exergy. In addition, as ramp length is increased, the forebody angle where the largest exergy destruction occurs varies, illustrating a highly coupled and complex relationship.

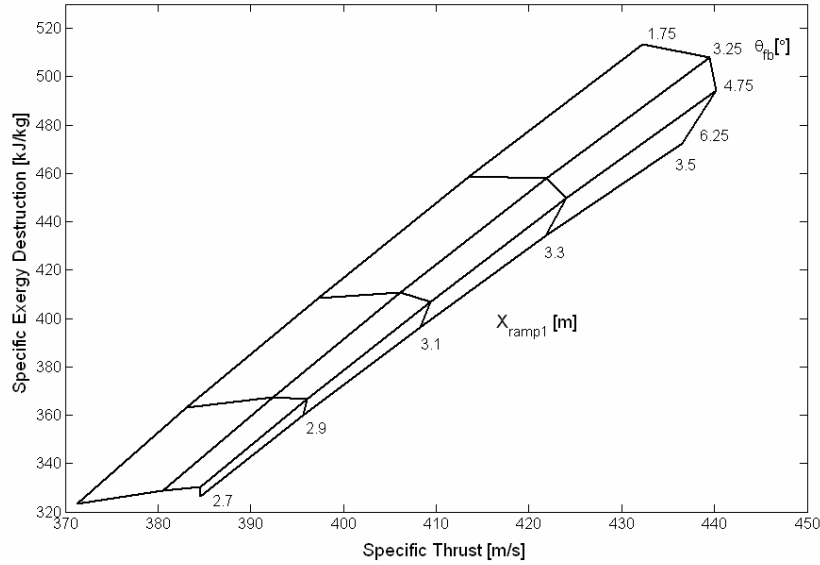


**Figure 2.13.** Parametric plot of inlet forebody angle and inlet first ramp length on engine specific exergy destruction and specific thrust [9].

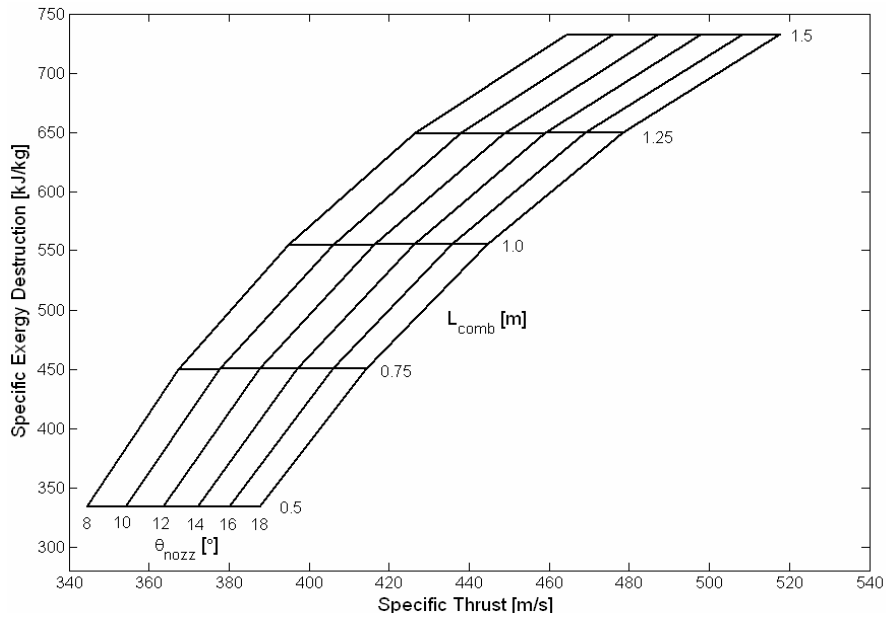


**Figure 2.14.** Parametric plot of combustor length and nozzle expansion angle on engine specific exergy destruction and specific thrust [9].

Figure 2.14 shows a parametric plot in which the combustor length,  $L_{comb}$  and nozzle expansion angle,  $\theta_{nozz}$ , are studied. In contrast to the previous figure, this result shows a somewhat more predictable response. The nearly parallel horizontal lines demonstrate the comparatively minimal

impact that nozzle expansion angle contributes to specific exergy destruction. This is due to the fact the nozzle destroys exergy only by means of such irreversibilities as friction and heat transfer, whereas the combustor destroys exergy by friction, heat transfer, incomplete combustion, and mixing effects. Again, a non-linear effect is observed. This study provided many unique insights into the potential tradeoffs and many limitations involved in hypersonic vehicle synthesis/design.

## **2.2.2 System and Mission-Level Exergy Applications in High Performance Aircraft Applications**

This section is dedicated to exploring the use of optimization in the synthesis/design of high performance aircraft. Though it has been addressed little in the literature, the methods, models, and results of these applications and analyses will be presented.

Traditionally, aircraft synthesis/design has been performed through the use of rules-of-thumb, experience, or simple trade-off analyses, primarily depending on the optimization of individual sub-systems and their combination. The perpetual development of high performance aircraft and their associated technologies constantly demands newer, more efficient, and interdisciplinary methods for evaluating and promoting their worth [11, 35]. Such a method was demonstrated by Rancruel and von Spakovsky [8, 36] with the use of a large-scale decomposition. In these studies, given a set of constraints, such as mission, environment, etc., the requirements of all sub-systems were met such that an optimal configuration was found. This was accomplished via “thermoeconomic isolation [36, 37],” in which time, conceptual, and physical decomposition were utilized to solve both system- and unit-level sub-system optimization problems.

This physical decomposition approach, called Iterative Local/Global Optimization (ILGO)<sup>12</sup>, was applied to the synthesis/design of an Advanced Tactical Fighter Aircraft. This was accomplished by decomposing the aircraft into the following six sub-systems: propulsion, fuel-loop, vapor compression and PAO loops, environmental control, airframe, and permanent/expendable payload and equipment group sub-systems. Consequently, a computational vehicle model was developed in which physical, thermodynamic, and aerodynamic interactions among sub-systems were captured. In total, these sub-systems contained nearly 500 degrees of freedom, with both discrete and continuous decision variables. ILGO was used to optimize the vehicle, in an integrated method, as the whole of each of the sub-systems synthesis/designs while including the effects of sub-system performance at off-design. The

---

<sup>12</sup> The Iterative Local/Global Optimization (ILGO) strategy was developed by Muñoz and von Spakovsky [7, 38, 39].

computational models were then utilized to optimize the system locally at both the component and sub-system levels as well as globally at the mission-level.

The performance of the Advanced Tactical Fighter Aircraft developed in this study was compared to the Air-to-Air Fighter presented by Mattingly, Heiser, and Daley [40], in which only the propulsion system was optimized. The airframe sub-system was modeled with the use of data and techniques established in Raymer [2] and Mattingly, Heiser, and Daley [40], while the propulsion sub-system was modeled using an industry engine deck which provided both thrust and the necessary power and mass flow rates required by the other sub-systems. The vehicle was optimized over a mission consisting of fourteen individual mission segments including take-off, climb, acceleration, loiter, cruise, as well as extensions and combinations of these. The objective of the optimization routine was to minimize gross take-off weight (through minimization of the thrust-to-weight ratio at take-off).

The gross take-off weight global optimum found by Rancruel and von Spakovsky was 22,396 lb., 28% lighter than the starting vehicle configuration, and was found in seven iterations. This vehicle configuration yielded a 1404 lb. (5.9%) lighter vehicle than that found by Mattingly, Heiser, and Daley. This result can be attributed to the fact that Rancruel and von Spakovsky performed and integrated synthesis/design optimization of all sub-systems involved.

Moorhouse suggests exergy as a common metric to evaluate vehicle performance tradeoffs at the system-level for multidisciplinary aircraft synthesis/design. This is done by defining total mission requirements as an exergy problem [11]. In this approach, rate of mission work  $\left(\frac{dw}{dt}\right)$  is defined as the rate of work required to lift and accelerate a vehicle's weight ( $W$ ) and payload ( $W_p$ ) as well as overcome the vehicle's irreversibilities and its extreme parasitic drag throughout an entire mission, i.e.

$$\frac{dw}{dt} = \frac{dw_{ovr}}{dt} + \frac{dw_{cust}}{dt}, \quad (2.9)$$

where  $\frac{dw_{ovr}}{dt}$  is the rate of overhead work required to move the vehicle given by

$$\frac{dw_{ovr}}{dt} = W \frac{de_w}{dt} + D_{ovr} U + \dot{P}_0 \mathcal{S}_{irr_{ovr}}. \quad (2.10)$$

In this equation,

$$e_w = \frac{U^2}{2g} + h \quad (2.10a)$$

is a weight specific energy (or exergy since kinetic and potential energies are pure forms of energy and exergy simultaneously),  $h$  is the altitude of the vehicle and  $U$  is its speed,  $D_{ovr}$  the parasitic drag chargeable to the vehicle itself and  $\dot{P}_0 \dot{S}_{irr}$  the rate of irreversibilities internal to the vehicle minus the payload and not including those associated with the fuel tank<sup>13</sup>. Similarly, the rate of customer work required to move the payload is given by

$$\frac{dw_{cust}}{dt} = W_p \frac{de_w}{dt} + D_{cust} U + \dot{P}_0 \dot{S}_{irr_{cust}}, \quad (2.11)$$

where  $D_{cust}$  is the parasitic drag chargeable to the payload itself and  $\dot{P}_0 \dot{S}_{cust}$  is the rate of irreversibilities internal to the vehicle (not including those for the fuel tank) but chargeable to the payload alone.

Now, an exergy balance on the vehicle results in

$$\eta e_{x_f} \frac{dW_f}{dt} = \frac{dw_{ovr}}{dt} + \frac{dw_{cust}}{dt} \quad (2.12)$$

where  $e_{x_f}$  is the weight specific exergy content of the fuel and  $\eta$  is the exergy combustion efficiency given by

$$\eta = \frac{\left( \frac{dW_{air}}{dt} \right) e_{x_{air}} - \left( \frac{dW_{exh}}{dt} \right) e_{x_{exh}} + \left( \frac{dW_f}{dt} \right) e_{x_f}}{\left( \frac{dW_f}{dt} \right) e_{x_f}}. \quad (2.13)$$

To consider how each sub-system, i.e. structure, controls, propulsion, etc., contributes to the overall exergy exchange during the mission, individual component losses can be modeled by decomposing these systems into sub-systems to show how each utilizes the exergy of the fuel. Furthermore, avoidable and unavoidable overhead can be identified, therefore providing insight for synthesis/design specifications and areas of potential improvement. In essence, Moorhouse provides an argument for utilizing exergy methods at all levels of vehicle and mission synthesis/design to unify the design process.

---

<sup>13</sup> The exclusion of the fuel tank irreversibility rate is due to the fact that they are taken into account in the vehicle's exergy efficiency which is detailed in Equation (2.12).

Periannan recently compared the use of both energy and exergy optimization techniques to the synthesis/design of an Advanced Aircraft Fighter (AAF) with three sub-systems: a Propulsion Sub-system (PS), an Environmental Control Sub-system (ECS), and an Airframe Sub-system (AFS) [10]. In this work, a non-linear gradient based optimization algorithm is coupled with the above AAF model and is flown through a representative mission, subject to a changing thrust and wing loading constraint diagram, as defined by Mattingly, Hesier, and Daley [40]. Five objective functions (see table 2.3) measure vehicle characteristics and interactions and are used to determine an optimum set of values for fifty-five operational and decision variables.

The first objective function minimizes the takeoff weight ( $W_{TO}$ ) of the vehicle, represented by the sum of the vehicle empty weight ( $W_E$ ), the Propulsion Sub-system weight ( $W_{PS}$ ), the Environmental Control Sub-system weight ( $W_{ECS}$ ), and the fuel weight ( $W_{FUEL}$ ). The second objective function minimizes the overall vehicle exergy destruction as a sum of the exergy losses of the PS ( $Ex_{DESTot\_PS}$ ), ECS ( $Ex_{DESTot\_ECS}$ ), and the unburned fuel exiting the nozzle ( $Ex_{FuelLoss}$ ). The third objective function is similar to objective function 2 with the addition of losses due to the Airframe Sub-system ( $Ex_{DESTot\_AFS-A}$ ). The thrust efficiency ( $\eta_{Thrust}$ ) is maximized in objective function 4 and is given as the realized thrust work ( $W_{Thrust}$ ) divided by the product of the fuel's mass ( $m_{Fuel}$ ) and lower heating value ( $LHV_{Fuel}$ ). Finally, the thermodynamic effectiveness ( $\epsilon_{thermo}$ ) is maximized in objective function 5 as realized vehicle thrust work divided by the maximum thrust work<sup>14</sup> ( $W_{Max}$ ).

**Table 2.3.** Objective functions for the AAF synthesis/design optimization performed by Periannan [10].

	Objective function	Equation
1	Minimize gross takeoff weight	$W_{TO} = W_E + W_{PS} + W_{ECS} + W_{FUEL}$
2	Minimize exergy destruction w/o AFS	$Ex_{obj2} = Ex_{DESTot\_PS} + Ex_{DESTot\_ECS} + Ex_{FuelLoss}$
3	Minimize exergy destruction w/ AFS exergy destruction	$Ex_{obj3} = Ex_{DESTot\_PS} + Ex_{DESTot\_ECS} + Ex_{FuelLoss} + Ex_{DESTot\_AFS-A}$
4	Maximize thrust efficiency	$\eta_{Thrust} = \frac{W_{Thrust}}{m_{Fuel} \times LHV_{Fuel}}$
5	Maximize thermodynamic effectiveness	$\epsilon_{thermo} = \frac{W_{thrust}}{W_{Max}} = 1 - \frac{Ex_{DESTot\_PS} + Ex_{DESTot\_ECS} + Ex_{FuelLoss}}{W_{Max}}$

<sup>14</sup> Here, the maximum thrust work is defined if no fuel is lost and there are no irreversibilities produced in the PS and ECS or in equation form,  $W_{Max} = W_{thrust} + Ex_{DESTot\_PS} + Ex_{DESTot\_ECS} + Ex_{FuelLoss}$ .

Once again, the application of an exergy approach facilitates the pinpointing and measuring of irreversibilities. Periannan discusses these in the form of parametric studies and carpet plots, similar to those presented by Roth and Mavris in figure 2.12. For example, figure 2.15 shows the effect of varying both fan bypass ratio and turbine inlet temperature on the rate of exergy destruction and specific thrust for a fixed compressor bypass ratio and mission segment.

Although not conclusive, the most significant result of this work appears to be that when AFS degrees of freedom are considered the best vehicle synthesis/design is found with an exergy based objective function which explicitly includes the exergy destruction due to the AFS. Without such an explicit inclusion of this variable, the objective functions listed in table 2.3 all converge on similar solutions. Illustrating the unifying nature of an exergy approach, this result demonstrates not only that exergy can be used to quantify and pinpoint losses throughout the vehicle but can also, in certain cases, provide a better vehicle synthesis/design overall.

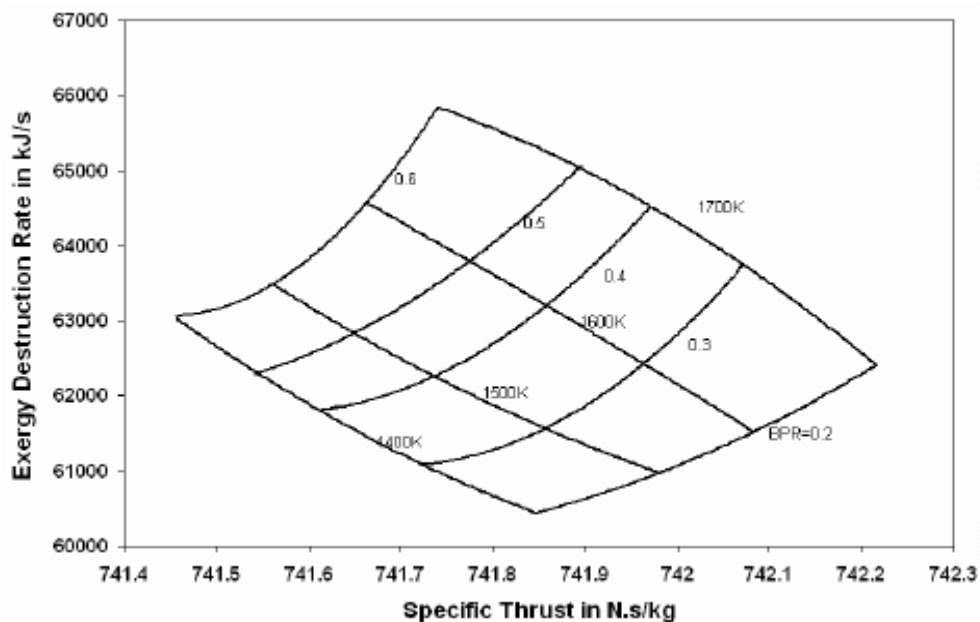


**Figure 2.15.** Variation of vehicle specific thrust and exergy destruction rate with fan bypass ratio and turbine inlet temperature for a fixed compressor pressure ratio of 8. (mission segment 5: Climb) [10].

In Markell, a hypersonic vehicle model developed jointly by myself and Markell, discussed in detail in Chapter 3, and consisting of inlet, combustor, nozzle, and airframe sub-systems is optimized for a partial scramjet mission using both energy- and exergy-based objective functions. A total of eight design and operational decision variables were used. Through the use of a genetic algorithm which generates random baseline vehicles, Markell observed the effect of an exergy approach to find the

minimum fuel usage for a partial mission which consisted of a cruise at Mach 8, an acceleration from Mach 8 to Mach 10, and a Mach 10 cruise. The goal was to find the minimum amount of energy (fuel) capable of performing the task. Throughout the optimization process a change in vehicle weight occurred each time the optimization chose new values of decision variables, and a uniform mass density based on a baseline vehicle was applied to a new geometry, as performed by Starkey [28] and discussed in Section 2.1.2. Unfortunately, the comparison of results for the energy- and exergy- based objective functions is not really meaningful since the baseline (empty) vehicle weight was different for each objective. Furthermore, even though the vehicle optimizations occurred over an integrated mission, i.e. the partial scramjet mission mentioned above, the objective functions were optimized on a rate basis and in effect resulted in non-integrated objective function optimizations. A more useful way of doing the mission-level optimizations would have been for the exergy-based objective to be on a non-rate basis and energy-based objective to be weighted average of thrust efficiency across the entire mission. It is this last approach for both objectives which has been used in this thesis work, the results of which are presented in Chapter 5.

Finally, as illustrated by all of these references, an exergy-based approach provides many insights into vehicle loss mechanisms and, in addition, provides a unifying framework for multidisciplinary vehicle design. In fact, it is an improvement over the typical energy-based approach to improving minimal energy use (fuel economy).

## Chapter 3

# Vehicle Sub-system and Component Models<sup>15</sup>

This chapter explicitly describes the vehicle sub-systems and component system models, solution procedures, and constraints used to simulate hypersonic vehicles and hypersonic flight. In addition, other options for component modeling are discussed, along with the benefits and shortcomings of each. To generate useful results, detailed models must be generated, and consequently, the majority of time spent working on this thesis work was put toward developing these tools. The prevailing goal throughout component development is to *accurately model flow behavior and loss mechanisms with the least possible computational burden*. Often, trade-offs between computational time and accuracy are made and are subsequently discussed.

### 3.1 Technical Background/ System Overview

This section provides a discussion of physical laws on which the sub-system and component models are based. These laws are presented in the form of governing equations, which are used throughout each component model. The general decomposition of the hypersonic vehicle is introduced, and essential terminology defined in an effort to prepare the reader for the sub-system and component development sections.

#### 3.1.1 Equations of Motion

A fluid can be described as a substance that deforms continuously when subjected to shear forces. Discovering the behavior, i.e. flow properties of the fluid, while it is subjected to various forces and situations is the goal of fluid mechanics. A gas is a fluid with weak intermolecular forces and, as a result, is vulnerable to large density changes from applied forces. Thus, gases are generally termed *compressible*, and specific equations for compressible flow are discussed in the next section. Here, it is important to outline the governing equations and the methods by which they are applied.

---

<sup>15</sup> All component and sub-system models were developed by Markell and myself in a joint effort to create an overall hypersonic vehicle simulation code [9].

Two methods exist for analyzing fluid flows: Lagrangian and Eulerian. The first follows a particular fluid molecule as it flows along a trajectory. Though interesting and capable of providing valuable insights, calculations using this method are highly complex; and, physical measurements of such phenomena pose unique problems. As a result, an Eulerian approach is often employed in engineering analyses. In this case, molecules are analyzed in bulk form, in an assumed continuous medium; and, properties are measured at the boundaries of a selected control volume through which fluid flows. The benefits of this type of approach are that local accelerations and decelerations of individual molecules can be neglected, thereby eliminating time as an independent variable in steady state applications. In addition, measurements of fluid properties at given instances in the flow are much simpler.

To solve complex fluid problems where compressibility effects are present, four equations (three governing equations and one equation of state) are needed to find the four primary unknown system fluid properties of pressure, temperature, density and velocity. The first two are the continuity equation and the momentum balance given in bulk flow terms by

$$\frac{dm}{dt} = \sum_q \dot{m}_q^{\leftarrow} \quad (3.1)$$

and

$$\sum F = \frac{dmV}{dt} + \sum_q V_q \dot{m}_q^{\leftarrow}, \quad (3.2)$$

where  $q$  denotes any flow inlet or exit of the system,  $m$  the system mass,  $\dot{m}$  a mass flow rate crossing the system boundary,  $V$  a velocity, and  $F$  a force. The final two necessary equations are the energy balance and the equation of state for an ideal gas, i.e.

$$\frac{dE}{dt} = -\dot{W}^{\rightarrow} + \sum_k \dot{Q}_k^{\leftarrow} + \sum_q \dot{m}_q^{\leftarrow} \left( h_q + \frac{V_q^2}{2} + gz_q \right) \quad (3.3)$$

$$P = \rho RT \quad (3.4)$$

In the energy balance, the time rate of change of energy,  $E$ , in the systems is equal to the heat rate,  $\dot{Q}_k^{\leftarrow}$  entering the system through  $k$  interactions, minus the rate of work,  $\dot{W}^{\rightarrow}$ , leaving the system, plus the

bulk flow enthalpies and kinetic and potential energies crossing the system boundaries (the last term in equation (3.3)).

Also of interest are the irreversibilities generated in a system, and thus, an entropy balance is written as

$$\frac{dS}{dt} = \sum_k \frac{\dot{Q}_k^{\leftarrow}}{T_k} + \sum_q \dot{m}_q^{\leftarrow} s_q + \dot{S}_{irr} . \quad (3.5)$$

Here, the time rate of change of entropy,  $S$ , is a function of heat transfer rates, the temperatures at which they occur at the system boundary, the bulk flow entropy transfer, and the rate of entropy generation due to irreversibilities,  $\dot{S}_{irr}$ , within the system. According to the second law of thermodynamics, the entropy generated must be greater than or equal to zero. For this study, all of the above equations are considered only for one-dimensional (bulk flow) analyses in steady state.

To study the usefulness of exergy analyses, the steady state combined rate balance, or exergy balance, is used and is expressed as

$$T_0 \dot{S}_{irr} = -\dot{W}^{\rightarrow} + \sum_k \dot{Q}_k^{\leftarrow} \left( 1 - \frac{T_0}{T_k} \right) + \sum_q \dot{m}_q^{\leftarrow} \left( h_q + \frac{V_q^2}{2} + gz_q - T_0 s_q \right) \quad (3.6)$$

Here, the ambient or reference (“dead”) state is denoted by the subscript “0”. It follows that the largest work out of the system or the least work into the system to perform a task occurs when a process is reversible<sup>16</sup>, i.e. when  $\dot{S}_{irr} = 0$ . Therefore, the term  $T_0 \dot{S}_{irr}$  represents the degradation of generalized available energy, also called *exergy destruction* [12]. What emerges is a measurable quantity which, when minimized, can provide valuable information regarding the optimal configuration and design of a system. Consequently, considerable time is spent developing methods to calculate  $\dot{S}_{irr}$ .

Finally, three ideal gas differential property relations are also used and are as follow:

$$ds = c_p(T) \frac{dT}{T} - R \frac{dP}{P} , \quad (3.7)$$

$$dh = c_p(T) dT , \quad (3.8)$$

and

---

<sup>16</sup> A reversible process of a system is defined as one after which the system can be restored to its initial state and leave no change in either the system or its surroundings [12].

$$du = c_v(T)dT , \quad (3.9)$$

where  $c_p$  is the specific heat at constant pressure and  $c_v$  is the specific heat at constant volume. Under ideal gas assumptions, the specific heats are functions of temperature only. These equations provide needed information about the flow mass specific properties entropy,  $s$ , enthalpy,  $h$ , and internal energy,  $u$ , respectively. Equations (3.1) to (3.9) provide the basis for the development of the following one- and two-dimensional compressible flow relations which are presented next.

### 3.1.2 Compressible Flow Relations

This section is dedicated to the methods by which a flow adjusts to the presence of a body. In compressible media, it happens that the upstream flow can sense the presence of pressure disturbances by wave propagation up to a defined limit. In this manner, the gas can adjust to the presence of an object before the object arrives. Once the object's speed reaches this limit, however, the flow can no longer sense its presence before it arrives, and a *shock* results. A shock process represents an abrupt change in flow properties occurring in a distance comparable to the mean free path of the molecules of the gas [41]. This finite distance can be approximated as a small fraction of a millimeter. Defining the limit at which shocks occur and being able to model flow behavior is an integral part of hypersonic aerodynamics.

Rearranging equation (3.7) and substituting the ideal gas equation of state and the Meyer relation  $R = c_p - c_v$ , an expression for the velocity of sound,  $a$ , of a gas can be expressed as

$$a = \sqrt{\gamma RT} \quad (3.10)$$

where  $\gamma$  is the ratio of specific heats,  $c_p/c_v$ . As it turns out, this is the limit at which pressure disturbances can no longer be sensed upstream. A convenient way of expressing the ratio of velocity to the speed of sound is by the dimensionless parameter, the Mach number, simply defined as

$$M = \frac{V}{a} . \quad (3.11)$$

Flow at Mach numbers below one are considered subsonic and those above supersonic. As mentioned in Chapter 1, hypersonic is generally defined as supersonic flow above Mach 5. The advantage of defining a Mach number emerges as relations are sought for the total, also called stagnation, flow properties. These relations, termed *isentropic* flow relations, define a reference state for compressible

flow. Isentropic, in this case, refers to a process that is both adiabatic and reversible<sup>17</sup>. The equations for total temperature and total pressure derived using the balance equations of the previous section applied to a control volume (system) are given as

$$T_t = T \left( 1 + \frac{\gamma - 1}{2} M^2 \right) \quad (3.12)$$

and

$$P_t = P \left( 1 + \frac{\gamma - 1}{2} M^2 \right)^{\frac{\gamma}{\gamma - 1}} \quad (3.13)$$

where the subscript  $t$  refers to the total or stagnation conditions and without the subscripts,  $T$  and  $P$  are the static conditions. These equations represent the temperature and pressure if they were brought adiabatically, or without a heat interaction, to rest at that point. They are useful because in many situations, total pressure and/or total temperature are constant, and thermodynamic processes such as heat interactions can be expressed as a function of total temperature. The development of two-dimensional shock-expansion theory, discussed next, relies upon the relations covered in equations 3.10 through 3.13.

Two-dimensional shock-expansion theory states that a supersonic flow encountering any change in boundary geometry results in an abrupt change in flow properties. When this flow approaches acute and obtuse changes in flow boundaries, *oblique shocks* and *centered*, or *Prandtl-Meyer, expansions* result respectively. These are both illustrated in figure 3.1. Detailed surveys of these two phenomena are necessary to develop many of the guiding solution procedures for problems of hypersonic flight.

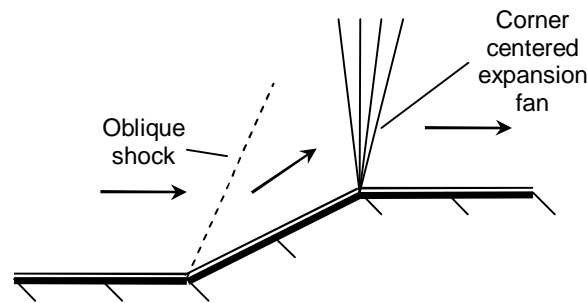


**Figure 3.1.** Oblique shock and centered expansion fan.

<sup>17</sup> Inspection of equation (3.5) shows that a steady state process can be isentropic, i.e. result in no change in entropy, under two conditions. The first is if the process is reversible,  $\mathcal{S}_{irr} = 0$ , and adiabatic,  $\mathcal{Q}_k^{\leftarrow} = 0$ . The second can occur when the entropy generation and heat terms are both nonzero. In this discussion, only the first case is considered here because an ideal (i.e. reversible) process, which is sought in aspects of design via the combined rate balance, generates no entropy due to irreversibilities.

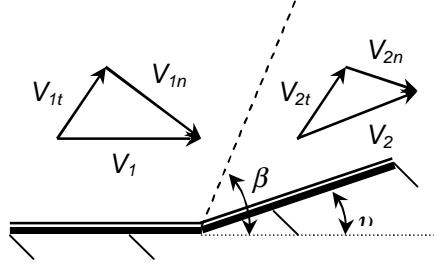


**Figure 3.2.** Oblique shock detail.

The flow solutions for oblique shocks are derived by breaking the flow into components normal and tangential to the shock wave angle,  $\beta$ . The wave angle, shown in figure 3.2, is a function of the incoming flow Mach number,  $M_1$ , and flow turning (or deflection) angle,  $\theta$ , which is found by solving the momentum and continuity equations in both the normal and tangential directions across the shock. This relationship is shown in equation (3.14). Knowing the incoming Mach number and upcoming boundary geometry, this relation is used to iteratively find the wave angle, i.e.

$$\tan \theta = 2 \cot \beta \frac{M_1^2 \sin^2 \beta - 1}{M_1^2 (\gamma + \cos 2\beta) + 2}, \quad (3.14)$$

where again  $\gamma$  is the ratio of specific heats. The normal and tangential Mach numbers, using the definition of Mach number, can now be written as

$$M_{1n} = M_1 \sin \beta, \quad (3.15)$$

$$M_{1t} = M_1 \cos \beta, \quad (3.16)$$

$$M_{2n} = M_2 \sin(\beta - \theta), \quad (3.17)$$

and

$$M_{2t} = M_2 \cos(\beta - \theta). \quad (3.18)$$

It turns out that the tangential velocities are equal, or  $V_{1t} = V_{2t}$ . In addition, the shock process is necessarily adiabatic because although thermal gradients occur across the shock, they do not transfer energy in the form of a heat interaction external to the control volume enclosing the shock. As a result, the energy equation can be reduced to show that total temperature is unchanged across the shock, i.e.  $T_{1t}$

=  $T_{t2}$ . Finally, further manipulation of these equations yields downstream properties expressed as functions of the normal downstream Mach number,  $M_{2n}$ . Thus,

$$M_{2n}^2 = \frac{M_{1n}^2 + \frac{2}{\gamma-1}}{\frac{2\gamma}{\gamma-1} M_{1n}^2 - 1}, \quad (3.18)$$

$$\frac{P_2}{P_1} = \frac{1 + \gamma M_{1n}^2}{1 + \gamma M_{2n}^2}, \quad (3.19)$$

and

$$\frac{T_2}{T_1} = \frac{1 + \frac{\gamma-1}{2} M_{1n}^2}{1 + \frac{\gamma-1}{2} M_{2n}^2}. \quad (3.20)$$

With these results, the flow behavior across shocks and the entropy generated can be characterized.

Shocks are complex processes which are irreversible because of the viscous dissipation and heat conduction that occur within the finite thickness of the shock [41]. Knowing these details is not necessary for analyzing the changes that occur from one side of the shock to the other. Combining the steady state entropy balance with equation (3.7), an expression for the rate of entropy generated due to irreversibility can be expressed as

$$\dot{S}_{irr} = \dot{m} \left( c_p \ln \left( \frac{T_2}{T_1} \right) - R \ln \left( \frac{P_2}{P_1} \right) \right). \quad (3.21)$$

Note that since this relationship is nonlinear, as are the relationships for Mach number, pressure and temperature change across the shock, the same flow turning angle accomplished with two shocks generates less entropy than that of a single shock. This has important implications for an inlet system which utilizes multiple shocks for compression.

It is also worthwhile to discuss that for certain maximum deflection angles there are no solutions to equation (3.14). This maximum angle is dependent on the flow Mach number, and physically represents the limit at which a shock becomes detached from a corner, as shown in figure 3.3. When this occurs, modeling becomes more difficult because flow near the wall is subsonic and flow away

from the wall is supersonic. This is due to a combination of normal and oblique shock effects. As will be discussed later, these effects must be taken into account in the sub-system and component models.

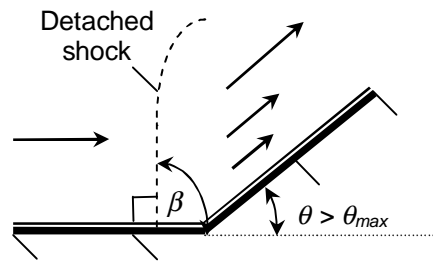


**Figure 3.3.** Detached shocks occur at angles greater than  $\theta_{max}$ .

Both oblique shocks and expansion fans are composed of Mach waves. The angle at which a Mach wave is inclined to the flow is called the Mach angle,  $\mu$ , given by

$$\mu = \sin^{-1} \frac{1}{M}. \quad (3.22)$$

Through infinitesimally small acute changes in deflection angle, an infinite number of Mach waves coalesce into a single oblique shock, with wave angle  $\nu$  described previously. For Prandtl-Meyer flow through an obtuse angle, however, these Mach waves do not interact and reinforce each other, but spread out as shown in figure 3.1 earlier. As a result, infinitesimal changes in entropy do not sum to a finite value, and the resulting process is isentropic. Thus, changes in temperature and pressure can be found from the isentropic relations, in equations (3.12) and (3.13). Knowing the downstream Mach number first, however, is essential. Finding the changes in flow properties requires scrutiny of the Mach wave interactions, somewhat similar to the oblique shock development described earlier, and is shown in figure 3.4.

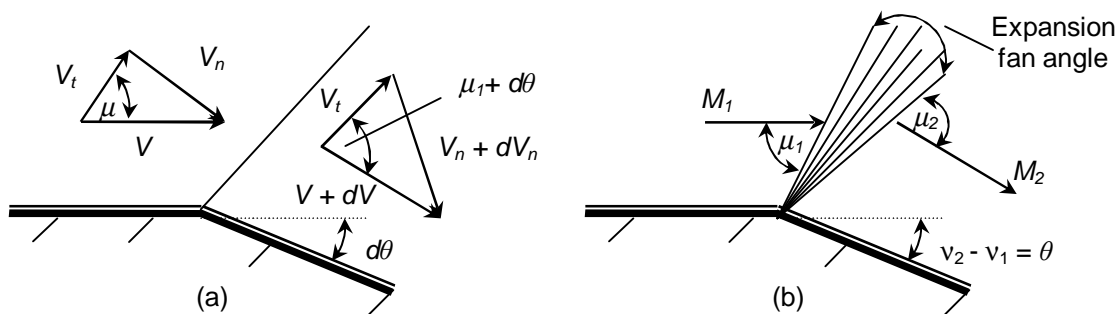


**Figure 3.4.** Prandtl-Meyer expansion detail for (a) an infinitesimal obtuse turning angle and (b) general flow turning.

The relationship between Mach wave angles,  $\mu$ , and reference turning angles,  $\theta$ , is given in equation 3.23, via the definition of a Mach wave angle, equation (3.22), such that

$$\theta = v(M_2) - v(M_1) \tag{3.23}$$

where

$$v(M) = \sqrt{\frac{\gamma+1}{\gamma-1}} \tan^{-1} \sqrt{\frac{\gamma-1}{\gamma+1} (M^2 - 1)} - \tan^{-1} \sqrt{M^2 - 1} \tag{3.24}$$

and  $v$  is called the Prandtl-Meyer function. Equation (3.24) assumes an arbitrary reference state defined as  $v_{ref} = 0$  when  $M = 1$ , which drops out of the expression when composing the flow turning angle as illustrated in equation (3.24). As a result, flow through a total turning angle,  $\nu$ , can be represented by the difference of two reference turning angles,  $\nu_2 - \nu_1$ . The result is that now the downstream Mach number, after expanding through a known turning angle, can be found by iteration.

Since the reference turning angle is zero when  $M = 1$ , Mach numbers increasingly greater than one have turning angles increasingly greater than zero, and what results is a limit on total flow turning. As was the case for shocks, there is a maximum turning angle after which solutions to equation (3.24) no longer exist. As  $M \rightarrow \infty$ , a maximum turning angle of  $130.4^\circ$  is reached. A few of these turning angle values are shown in table 3.1. John [41] states that departure from ideal gas conditions occurs before the maximum flow turning can be reached; however, knowing that such limits exist has important implications for vehicle geometry design. Also, unlike with oblique shocks, any amount of flow turning can be accomplished by single or multiple fans without variations in downstream flow properties due to the fact that during an expansion process there are no compounding interactions between individual Mach waves.

**Table 3.1.** Prandtl-Meyer function and maximum turning angles for various Mach numbers ( $\gamma = 1.4$ ).

$M_i$	$\nu_i (M_i)^\circ$	$\theta_{max} = \nu_\infty (M_\infty) - \nu_i (M_i)^\circ$
1	0	130.4
4	65.8	64.6
8	95.6	34.8
12	106.9	23.5
$\infty$	130.4	0

### 3.1.3 Generalized One-Dimensional Flow

While two-dimensional compressible flow calculations for shocks and expansions are quite straightforward, the introduction of physical phenomena such as friction and heat and mass transfer within a duct or streamtube require complicated and lengthy methods of solution beyond the scope of this project. Thus, solutions using one-dimensional approximations are utilized and give a good indication of the actual flow properties under the following conditions [42]:

- (i) The fractional rate of change of area with respect to distance along the axis is small,  $dA/A \ll 1$ .
- (ii) The radius of curvature of the duct is large compared with the passage diameter.
- (iii) The shapes of the velocity and temperature profiles are approximately unchanged from section to section along the axis of the duct.

A general application of such an analysis is shown in figure 3.5. A differential control surface is drawn representing a single section of the flow within which properties are constant. A solution across a finite distance can now be solved explicitly though the use of numerical methods.

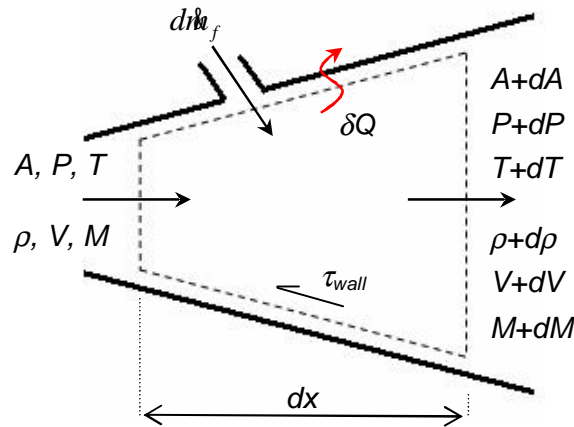


**Figure 3.5.** A generic one-dimensional differential duct with multiple physical interactions.

To consider all of the effects of energy addition or subtraction, friction, change in area, fuel addition, etc., Shapiro developed the table of influence coefficients shown in table 3.2 from a general set of governing and constitutive equations similar to ones presented in the previous sections. Each influence coefficient represents the partial derivative of the dependent variable in the left hand column with respect to the independent variable in the top row. The variables are distinguished by which can

locally be controlled or described as functions of the x-direction (the top row), and those which cannot (the left hand column). For example, in a laboratory experiment, area change by some designed geometry, friction by way of material surface roughness, and injection mass flow rate can all be parameters of the experimental setup. The same can be said for the other independent variables. What results is an extremely useful set of equations which can be applied to most problems in supersonic flow. As an example, to know the effect of friction and mass flow addition on Mach number in a variable area duct, with all other effects negligible, the resulting relation would be

$$\begin{aligned} \frac{dM}{M} = & -\frac{\left(1 + \frac{\gamma-1}{2}M^2\right)}{1-M^2} \left(\frac{dA}{A}\right) - \frac{\gamma M^2 \left(1 + \frac{\gamma-1}{2}M^2\right)}{2(1-M^2)} \left(4C_f \frac{dx}{D}\right) \\ & + \frac{\left(1 + \gamma M^2\right) \left(1 + \frac{\gamma-1}{2}M^2\right)}{1-M^2} \left(\frac{d\dot{m}}{\dot{m}}\right). \end{aligned} \quad (3.25)$$

Similar relations can be constructed to calculate the temperature, pressure, and entropy changes in the inlet, combustor, and nozzle of a scramjet engine is presented later in this chapter for the hypersonic vehicle modeled in this thesis work. In the top row of table 3.2, i.e. the independent variables,  $A$  is the duct area,  $Q$  the heat transfer into the duct,  $H$  the total enthalpy into the duct,  $c_f$  the coefficient of duct surface friction,  $D$  the diameter of the (assumed circular) duct,  $\gamma$  the ratio of specific heats, and  $M_w$  the molecular weight of the fluid. The determination of the values of these independent variables is discussed in detail in the following sections.

**Table 3.2.** Influence coefficients for flow in a duct [42].

	$\frac{dA}{A}$	$\frac{dQ + dH}{c_p T}$	$4c_f \frac{dx}{D} - 2\gamma \frac{d\dot{m}}{\dot{m}}$	$\frac{d\dot{m}}{\dot{m}}$	$\frac{dM_w}{M_w}$	$\frac{d\gamma}{\gamma}$
$\frac{dM}{M}$	$-\frac{\left(1 + \frac{\gamma-1}{2}M^2\right)}{1-M^2}$	$\frac{1 + \gamma M^2}{2(1-M^2)}$	$-\frac{\gamma M^2 \left(1 + \frac{\gamma-1}{2}M^2\right)}{2(1-M^2)}$	$\frac{\left(1 + \gamma M^2\right) \left(1 + \frac{\gamma-1}{2}M^2\right)}{1-M^2}$	$-\frac{1 + \gamma M^2}{1-M^2}$	-1
$\frac{dT}{T}$	$\frac{(\gamma-1)M^2}{1-M^2}$	$\frac{1 - \gamma M^2}{1-M^2}$	$-\frac{\gamma(\gamma-1)M^4}{2(1-M^2)}$	$-\frac{M^2(\gamma-1)\left(1 + \gamma M^2\right)}{1-M^2}$	$\frac{(\gamma-1)M^2}{1-M^2}$	0
$\frac{dP}{P}$	$\frac{\gamma M^2}{1-M^2}$	$-\frac{\gamma M^2}{1-M^2}$	$-\frac{\gamma M^2 [1 + (\gamma-1)M^2]}{2(1-M^2)}$	$-\frac{2\gamma M^2 \left(1 + \frac{\gamma-1}{2}\right) M^2}{1-M^2}$	$\frac{\gamma M^2}{1-M^2}$	0
$\frac{ds}{c_p}$	0	1	$-\frac{(\gamma-1)M^2}{2}$	$(\gamma-1)M^2$	0	0

### 3.1.4 Hypersonic Vehicle Description and Decomposition

Having laid the foundation for the component models, the system, consisting of both propulsion and airframe sub-systems, can briefly be introduced. The system breakdown can be seen in figure 3.6. The propulsion sub-system consists of inlet, combustor and nozzle, while the airframe sub-system guarantees the vehicle maintains force and trim balances throughout the varying flight conditions. To ensure that the intricacies of each component and the high-level of integration are taken into account, a detailed description of the system is presented next.

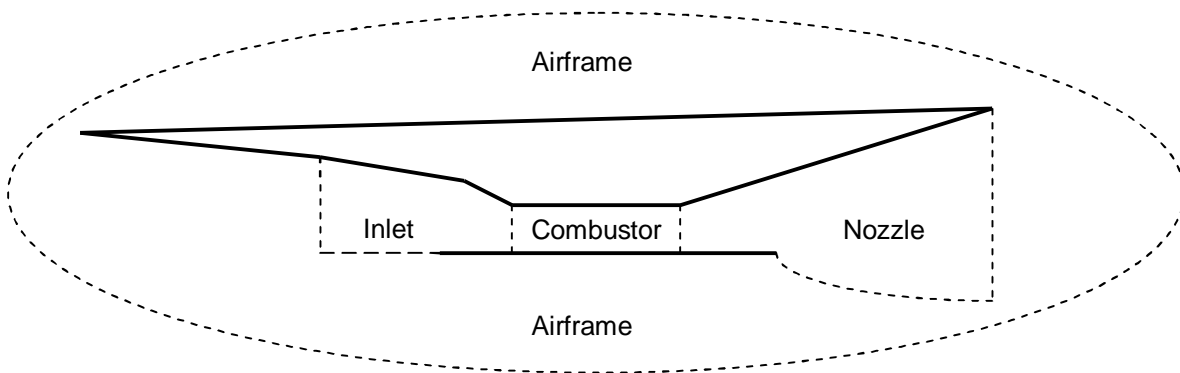


**Figure 3.6.** Propulsion sub-system components and airframe sub-system.

## 3.2 Inlet Component Model

As discussed in Chapter 2, the inlet plays a vital role in overall vehicle operation in that small changes in inlet performance can greatly impact overall performance. One purpose of the inlet is to reduce the speed of the flow so that the majority of the fuel can be mixed with the incoming air and burned before leaving the combustor. A second is to compress the flow from atmospheric conditions to a temperature and pressure at which auto ignition of the fuel will occur. Flow uniformity at the combustor entrance is desired as well. From energy usage and performance standpoints, the inlet should perform these functions as efficiently as possible.

### 3.2.1 Inlet Design and Variables

The inlet design harnesses the characteristics of supersonic flow behavior to decelerate and compress the flow via oblique shocks. As a result, a three shock system geometry was chosen to satisfy the inlet performance needs. The three shocks, due to the forebody and first and second ramps, meet on

the cowl lip and a reflected shock intersects with the roof of the combustor entrance. This process is illustrated in figure 3.7.

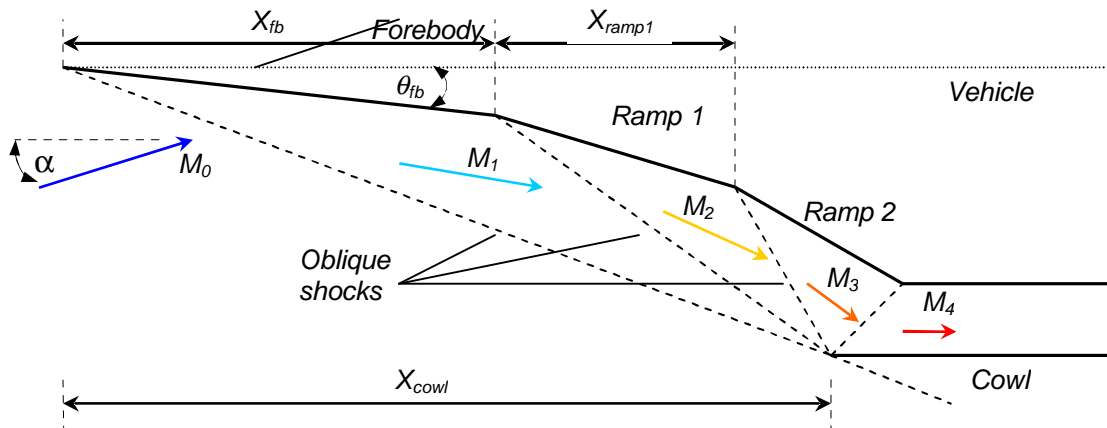


**Figure 3.7.** Inlet geometry and design details [9].

It should be noted that technically, the forebody is not considered part of the inlet since the inlet is normally considered to start at the position of the first ramp. However, for force accounting purposes discussed later in this chapter, the forebody is included. Of course, in actuality, the forebody is considered an integral part of the diffusion process, and the high level of vehicle integration makes complete separation of the two components impossible. Here, the positions of the forebody,  $X_{fb}$ , the first ramp,  $X_{ramp1}$ , and the cowl,  $X_{cowl}$ , are referenced in the axial direction from the front of the vehicle. The forebody angle,  $\theta_{fb}$ , is referenced to a line parallel with the vehicle centerline, and the angle of attack,  $\alpha$ , is the angle at which the centerline of the vehicle is inclined to the direction of flight. A summary of these variables, all of which are independent, is given in table 3.3. A benefit of modeling the vehicle this way is that flow is delivered to the combustor aligned with the vehicle centerline which results in a streamthrust exiting the nozzle also aligned with the vehicle centerline. This greatly simplifies aerodynamic force and moment calculations.

**Table 3.3.** Inlet independent design and operational variables.

Variable	Classification	Symbol	Imposed Limits
Forebody position [m]	Design	$X_{fb}$	$0.35L_{veh} \leq X_{fb} \leq 0.65L_{veh}$
Cowl position [m]	Design	$X_{cowl}$	$0.45L_{veh} \leq X_{cowl} \leq 0.77L_{veh}$
Ramp 1 position [m]	Design	$X_{ramp1}$	$0.02L_{veh} \leq X_{fb} \leq 0.33L_{veh}$
Forebody angle [°]	Design	$\theta_{fb}$	$1 \leq \theta_{fb} \leq 6$
Angle of attack [°]	Operational	$\alpha$	$0 \leq \alpha \leq 6$

The ranges shown represent values that can be chosen by an optimization program to create different vehicle configurations and produce a “best” design based upon some specified performance objective. These were selected on the basis of geometric viability and performance limitations. They can also be refined once initial solutions are found. These are discussed further in Section 3.2.4.

The problem of off-design performance must also be addressed. All of the decision variables are fixed once the vehicle begins simulation, i.e. there is no translating cowl capable of ensuring a shock-on-lip condition during varied flight conditions. Consequently, flow spillage<sup>18</sup> or shock ingestion calculations must be performed, or another method capable of maintaining shock-on-lip must be employed for off-design flight. With an inlet design chosen, methods must be developed to find the resulting flow properties and model loss mechanisms within the component.

### 3.2.2 Inlet Solution Procedure

Presented here is the solution procedure prescribed by Markell [9]. Figure 3.8 shows the three relevant flow areas found in the inlet. The term  $A_{total}$  represents, with the shock-on-lip, the total capture area of freestream flow and also the location of the engine cowl from the reference line. This reference line represents a line axially aligned with the vehicle centerline, starting from the front of the forebody. The area where internal compression begins is signified by  $A_{ic}$  while  $A_{throat}$  represents the inlet throat area. An example of both a ramp (or forebody) height,  $h_{ramp2}$ , and a shock angle,  $\beta_{fb}$ , are given in figure 3.8 because they are frequently referred to in the solution procedure.

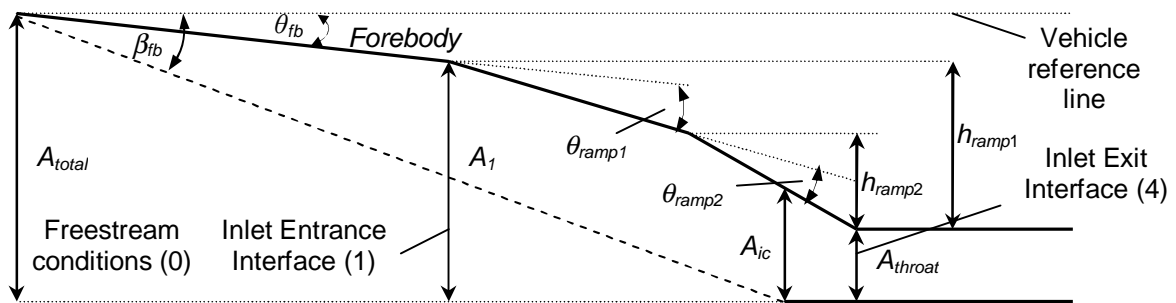


Figure 3.8. Inlet interface and vehicle geometric definitions [9].

The total vehicle contraction ratio and the inlet contraction ratio are given by

<sup>18</sup> Flow spillage can be defined as the optimum mass flow minus the actual mass flow that enters the inlet at off-design operation.

$$CR = A_{total} / A_{throat} \quad (3.26)$$

and

$$ICR = A_{ic} / A_{throat} \cdot \quad (3.27)$$

The height of the forebody and first and second inlet ramps can be calculated by referencing figures 3.7 and 3.8 and using

$$h_{fb} = X_{fb} \tan \theta_{fb} , \quad (3.28)$$

$$h_{ramp1} = X_{ramp1} \tan(\theta_{fb} + \theta_{ramp1}) , \quad (3.29)$$

and

$$h_{ramp2} = X_{ramp2} \tan(\theta_{fb} + \theta_{ramp1} + \theta_{ramp2}) , \quad (3.30)$$

where  $X_{ramp2}$  is found as a function of both capture area and the forebody, first and second ramp heights (as described in step 9) known geometries as described in the following steps (step 9 specifically). Above, each subsequent angle is referenced from the previous angle as shown in figure 3.8.

The steps taken to solve the oblique shock wave system and its associated geometry for the hypersonic vehicle while operating at design conditions are as follow:

1. With knowledge of the freestream properties ( $M_o, P_o, T_o, V_o$ ),  $\alpha$ , and  $\theta_{fb}$ , calculate the forebody oblique shock angle,  $\beta_{fb}$ , the flow properties downstream of the shock, and the entropy generated by the shock process using equations (3.12) through (3.22).
2. Calculate the total capture area,  $A_{total}$ , from the relationship

$$A_{total} = X_{cowl} \tan(\beta_{fb} - \alpha) \quad (3.31)$$

from which the captured mass flow rate is easily computed by means of a steady state application of the momentum equation, i.e.  $\dot{m} = \rho_o A_{total} V_o$ .

3. Determine the height of the forebody,  $h_{fb}$ , from equation 3.26 with the variables  $X_{fb}$  and  $\theta_{fb}$ .
4. The oblique shock wave angle emanating from the first inlet ramp can now be obtained from basic geometry

$$\beta_1 = \tan^{-1} \left( \frac{A_{total} - h_{fb}}{X_{cowl} - X_{fb}} \right) - \theta_{fb} \quad (3.32)$$

and the corresponding first inlet ramp angle,  $\theta_{ramp1}$ , is produced by direct application of equation (3.14).

5. Once again, calculate the downstream properties and the irreversibility associated with the shock using equations (3.12) through (3.21).
6. Repeat step 3 to determine the height of the first inlet ramp,  $h_{ramp1}$ .
7. Repeat steps 4 for the second inlet ramp shock wave angle,  $\beta_{ramp2}$ , and 5 for the properties after the second inlet ramp shock, then repeat step 3 for the second inlet ramp height as well.
8. With knowledge of the forebody deflection angle, both inlet ramp angles, and the Mach number just upstream of the cowl shock, the cowl shock angle needed adjust the flow so that it flows into the combustor,  $\beta_3$ , is calculated from equation (3.14).
9. Two separate expressions for  $A_{throat}$  must be set equal to one another to ensure that the shock emanating from the cowl lip is canceled at the expansion corner. The second inlet ramp axial length that satisfies this condition is

$$X_{ramp2} = \frac{A_{throat} - h_{fb} - h_{ramp1} - (X_{fb} + X_{ramp1} - X_{cowl}) \tan \delta_3}{\tan \delta_3 + \tan(\theta_{fb} + \theta_{ramp1} + \theta_{ramp2})} \quad (3.33)$$

where  $\delta_3$  is as defined in figure 3.9 and the total inlet length is calculated by summing the forebody axial length with the two ramp axial lengths, or  $X_{inlet} = X_{fb} + X_{ramp1} + X_{ramp2}$ .

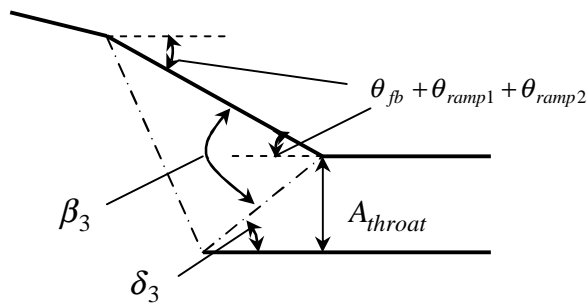


**Figure 3.9.** Inlet throat detail [9].

10. Steps 4 and 5 are repeated for the cowl oblique shock. The throat area is calculated by subtracting the forebody and ramp heights from the total capture area.
11. With a complete description of the flow properties throughout the inlet as well as the inlet configuration now known, the pressure forces acting on all surface areas can be calculated.

These pressure forces along with their corresponding location of action (assumed to be center of each segment) are passed on to the aerodynamic program for lift and drag calculations.

Due to the complexities regarding solving two-dimensional flow problems with friction, heat transfer, etc. as covered in Section 3.1.3, frictional effects and shocks must be accounted for separately for computational times to be reasonable. Consequently, a conceptual diffuser of contraction ratio  $A_1/A_{throat}$  and surface area equal to the inlet surface area (length of both inlet ramps) is employed in conjunction with the flow properties at the inlet entrance (station 1 of figure 3.10) to determine the rate of irreversibility produced by the friction,  $\dot{S}_{irr,fric}$ . Using a differential marching scheme, the following equations constructed from table 3.2 are solved for the diffuser:

$$\frac{dM}{M_x} = - \left( \frac{1 + \frac{\gamma-1}{2} M_x^2}{1 - M_x^2} \right) \frac{dA}{A_x} + \frac{\gamma M_x^2 \left( 1 + \frac{\gamma-1}{2} M_x^2 \right) 2C_f dA_{surf}}{1 - M_x^2 A_x}, \quad (3.34)$$

$$\frac{dT}{T_x} = \frac{1}{1 - M_x^2} \frac{dA}{A_x} - \frac{\gamma(\gamma-1)M_x^4}{2(1 - M_x^2)} \frac{4C_f dA_{surf}}{A_x}, \quad (3.35)$$

$$\frac{dP}{P_x} = \frac{\gamma M_x^2}{1 - M_x^2} \frac{dA}{A_x} - \frac{\gamma M_x^2 [1 + (\gamma-1)M_x^2]}{2(1 - M_x^2)} \frac{4C_f dA_{surf}}{A_x}, \quad (3.36)$$

and

$$\frac{ds}{c_p} = \frac{dT}{T_x} - \frac{\gamma-1}{\gamma} \frac{dP}{P_x}. \quad (3.37)$$

The friction entropy generation rate along with the properties exiting the inlet exit interface (station 4 of figure 3.10) are then passed to a separate solver to produce the flow properties at the entrance to the combustor, station 5. To clarify this statement, station 4 is the actual *physical* exit of the inlet component. Station 5 coincides with this physical location, however, the properties at station 5 are ‘adjusted’ (using the known rate of irreversibility produced from friction) from the properties at station 4 to reflect the effects of friction on the inlet flow.

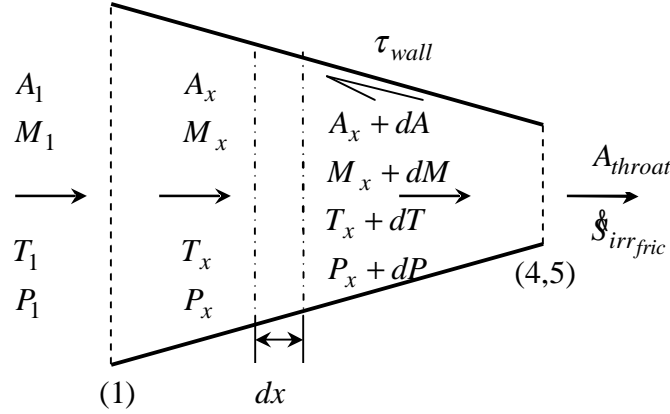


**Figure 3.10.** Conceptual diffuser used to calculate the entropy generation rate due to friction [9].

The total temperature at station 5 is equal to that at station 4 and the total pressure loss as a result of the irreversibility due to friction is calculated from

$$\frac{\dot{S}_{irr\_fric}}{\dot{m}R} = -\ln\left(\frac{P_{t5}}{P_{t4}}\right). \quad (3.38)$$

The area used for these calculations is the inlet throat area. Since the mass flow rate, inlet throat area, and total pressure and temperature at station 5 are known, the relationship

$$\dot{m} = \frac{P_{t5}}{\sqrt{RT_{t5}}} A_5 \sqrt{\gamma} M_5 \left(1 + \frac{\gamma-1}{2} M_5^2\right)^{(\gamma+1)/(2-2\gamma)} \quad (3.39)$$

can be used to determine the Mach number at station 5. This polynomial is solved using a root finder and only one of the six roots (i.e. when  $\gamma = 1.4$ ) is an acceptable solution (does not contain an imaginary part, is not negative, and is not a subsonic Mach number). Once the correct Mach number is chosen, static pressure and temperature can be calculated from the isentropic property relations given in equations (3.12) and (3.13).

A key area of concern is off-design performance. To guarantee operability throughout various flight conditions, some method must be applied to either control flow inlet flow or calculate flow spillage. The former was chosen based on the work of Moorhouse, Hoke, and Prendergast [43]. Here, energy exchange in the form of a heat interaction is required in front of the forebody oblique shock the first inlet ramp shock. The conceptual system is shown in figure 3.11. Heat is added or removed to bring the flight Mach number to the design Mach number, where the latter is the Mach number at which no energy interaction is needed to for the forebody and first inlet ramp shocks to fall on the cowl lip, i.e.

the combination of vehicle geometry and uninfluenced flight Mach number naturally locate the shocks-on-lip as calculated in the steps presented previously. As a result, the maximum mass flow is captured at each flight Mach number (each mission segment) at the cost of the energy interaction.

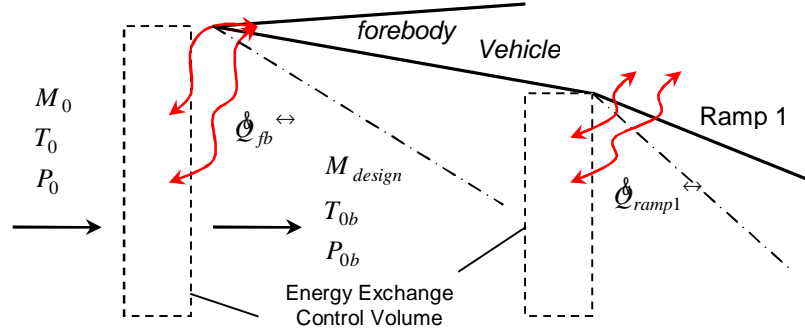


**Figure 3.11.** Inlet flow tailoring system using energy exchange [9].

The tailoring of the shock system to produce a shock-on-lip conditions is done through the following procedure. A design Mach number of  $M_{design} = 9$  is chosen. This is chosen based on the ability of all shocks occurring throughout the total mission, as designed in Chapter 4, to be tailored to this Mach number. The cross-sectional area of the energy exchange control volume equals the freestream capture area,  $A_{total}$ . For a given freestream Mach number of  $M_0$ , the thermal energy required to achieve the design Mach number is found using

$$\dot{Q}^{\leftrightarrow} = \dot{m} c_p (T_{t_{0b}} - T_{t_0}) \quad (3.40)$$

where

$$\frac{T_{t_{0b}}}{T_{t_0}} = \left( \frac{1 + \gamma M_0^2}{1 + \gamma M_{design}^2} \right)^2 \left( \frac{M_{design}^2}{M_0^2} \right)^2 \left( \frac{1 + \frac{\gamma-1}{2} M_{design}^2}{1 + \frac{\gamma-1}{2} M_0^2} \right) \quad (3.41)$$

and  $P_{0b} = P_0$ . At Mach numbers less than the design condition, energy must be extracted; at Mach numbers above that for design, energy must be deposited. Once  $T_{t_{0b}}$  and  $P_{0b}$  are calculated, the static temperature and pressure exiting the control volume are determined from the isentropic flow relations (equations (3.11) and (3.12)). The same approach is applied to the control volume after the forebody shock and before the first inlet ramp shock. As a result, flight operating conditions within a given range (again, dependent on the design Mach number) can all be made to result in the optimum mass capture at

all times. The rate of entropy generation due to irreversible heat exchange (i.e. across a finite temperature difference) can be found from an entropy balance across each of the control volumes in figure 3.11. Equation (3.42) is an example of the rate of entropy generation due to the forebody energy exchange, i.e.

$$\dot{S}_{irr_{ng}} = \dot{m}(s_{0b} - s_0) - \frac{\dot{Q}^{\leftarrow}}{T_{0b}}. \quad (3.42)$$

The irreversibilities produced by energy addition are charged to the airframe sub-system.

This methodology is easily applied to the inlet model considered here and does not require iterative solution procedures common in flow spillage calculations. It should be noted, however, that this is a simplified version of a highly complicated system such as those discussed in Chapter 2.

### 3.2.3 Inlet Loss Mechanisms

The two mechanisms for loss in the inlet are due to friction and shocks. The irreversibilities due to friction are found with equation (3.40) as discussed previously. The three shocks which contribute to the rate of entropy generation are the first and second ramp shocks, as well as the reflected cowl lip shock, labeled together with the subscript “1-3.” These values can be found by applications of equation (3.22) across each of the shocks. The total rate of entropy generation due to irreversibilities in the inlet is then given by

$$\dot{S}_{irr_{inlet}} = \dot{S}_{irr_{fric}} + \dot{S}_{irr_{shocks\ 1-3}} \quad (3.43)$$

Forebody friction and shocks are charged to the airframe sub-system, along with the irreversibilities due to the energy exchange processes.

### 3.2.4 Inlet Constraints

A number of geometric and flow property constraints, primarily based on realistic operating conditions, are placed upon the inlet to ensure a realistic operating condition. These are given in table 3.4.

This first geometric constraint ensures that the cowl begins at an axial position within the axial boundaries of the second ramp (see figure 3.7). Without this constraint, the shock at the cowl, if a suitable shock angle can be found, will be ingested into the combustor resulting in shock ingestion or

fall short of the cowl lip resulting in mass spillage. The second constraint imposes a realistic limit on the length of the forebody plus inlet, denoted above as  $X_{inlet}$ . Though vehicle configurations may be possible with  $X_{inlet} \leq 0.85 L_{veh}$ , where  $L_{veh}$  is the vehicle length, the likelihood of the overall vehicle producing any appreciable thrust in conjunction with the imposed nozzle constraints is highly improbable. Individual ramp angles are constrained to be more than one degree and less than twenty. This ensures that a ramp occurs, i.e. the ramp influences the flow and is not just a continuation of the previous geometry, and also prevents strong shocks from occurring as a result of large deflection angles. A final geometric constraint prevents strong shock reflections at the cowl entrance due to large flow turning angles. This constraint varies based on the acceptable combustor entrance Mach number range, discussed below. The specified range must be below twenty-eight degrees for the lowest acceptable Mach number and less than thirty-eight degrees for the highest.

**Table 3.4.** Inlet design and operational constraints.

	No.	Description	Range
<b>Geometric</b>	1	Cowl position [m]	$X_{fb} + X_{ramp1} < X_{cowl} < X_{fb} + X_{ramp1} + X_{ramp2}$
	2	Total inlet length (including forebody) [m]	$X_{inlet} = X_{fb} + X_{ramp1} + X_{ramp2} \leq 0.85L_{veh}$
	3	Ramp angles [°]	$1 \leq \theta_{ramp1}, \theta_{ramp2} \leq 20$
	4	Total inlet flow turning angle [°] (including forebody)	$\theta_{total} = \theta_{fb} + \theta_{ramp1} + \theta_{ramp2} \leq 28_{M=2.2} \rightarrow 38_{M=4.2}$
<b>Flow</b>	5	Combustor entrance Mach number	$2.2 \leq M_5 \leq 4.2$
	6	Combustor entrance pressure [Pa]	$P_5 \geq 50,600$
	7	Combustor entrance temperature [°K]	$T_5 \leq 2000$

Two primary concerns regarding combustor flow velocity are that i) the velocity does not ever become subsonic and ii) that the velocity does not become so excessive such that reaction of the constituents occurs unreasonably far from the combustor entrance. In addition, temperatures must be kept below levels which produce dissociation, and pressures must be great enough for auto ignition of the fuel. The values shown in table 3.4 for combustor entrance Mach number, temperature, and pressure reflect the influence of these constraints based on the works of many authors (e.g., Heiser and Pratt [3], Curran and Murthy [5], and Markell [9]). Finally, the inlet flow parameters needed are given in the table below.

**Table 3.5.** Inlet flow parameters.

Parameter	Value
Specific heat ratio, $\gamma$	1.4
Specific gas constant, $R$	288.2 J/kg K
Constant pressure specific heat, $c_p$	1009 J/kg K
Skin friction coefficient, $C_f$	0.00123

### 3.2.5 Inlet Design Considerations

The inlet design presented in this section represents one of many possible configurations. This particular design proved most suitable for the simplicity and flexibility desired of a hypersonic inlet in this thesis work. Other methods include, as previously mentioned, axisymmetric engines, which have already been defined as undesirable. Most commonly, two, three, or four shock systems are employed, utilizing both internal and external compression. Moving beyond four shocks, one can model the system as isentropic; however, determining the smooth surface geometry necessary to accommodate such a design is a lengthy process, which is discussed briefly in section 3.4. In addition, the model described in this paper maintains a centerline aligned streamthrust, which is useful for simplifying aerodynamic calculations. It is very likely that in a more detailed study, some type of thermal cooling would be necessary to maintain reasonable material surface temperatures in the inlet. A survey of inlet types is provided by Heiser and Pratt [3]. The mixture of one and two-dimensional methods shown throughout this section, and most of the vehicle as well, is why the flow throughout this analysis is termed quasi-one-dimensional.

### 3.3 Combustor Component Model

The responsibility of the combustor is to release energy from the fuel into the flow which is then transformed into thrust via expansion in a nozzle. Consequently, high temperatures caused by the reacting flows require that cooling be applied to maintain material integrity. This is typically accomplished by circulating fuel behind the combustor wall prior to injection. Thus, some of the energy of combustion is transferred to the fuel after combustion, serving as a needed preheating mechanism. As in conventional aircraft, the combustor is the source of the majority of losses. These losses occur due to

fuel-air mixing, incomplete combustion, friction, heat transfer, and non-equilibrium effects. Accurately modeling how these losses occur is vital to overall vehicle performance evaluation.

### 3.3.1 Combustor Design and Variables

The ability of Hydrogen to absorb and release significantly more energy per unit mass than conventional engine fuels makes it the fuel of choice for hypersonic propulsion and, thus, the fuel chosen for this study. It should be noted, however, that the low density of hydrogen introduces cryogenic cooling and storage challenges not specifically addressed in this study<sup>19</sup>. A combustor schematic is provided in figure 3.12. The two design variables for the combustor are the length,  $L_{comb}$ , and the equivalence ratio,  $\phi$ . The combustor length is fixed once flight begins, while the equivalence ratio varies to match the thrust requirements of each mission segment. The equivalence ratio is defined as the fuel to air ratio divided by the stoichiometric fuel to air ratio, as given in equation (3.44), i.e.

$$\phi = \frac{f}{f_{st}} \tag{3.44}$$

The combustor length is constrained to be at least two percent of the vehicle length, and no more than thirty-three percent. The equivalence ratio is prohibited from exceeding a value of two. These constraints primarily serve as practical limitations on the two variables, since a range any larger would likely result in a vehicle incapable of flight.

**Table 3.6.** Combustor design variables.

Variable	Type	Symbol	Imposed Limits
Combustor Length [m]	Independent, design	$L_{comb}$	$0.02L_{veh} \leq L_{comb} \leq 0.33L_{veh}$
Equivalence ratio	Dependent, operational	$\phi$	$0 \leq \phi \leq 2.0$

As illustrated in figure 3.11, the combustor has constant cross-sectional area fixed by the inlet geometry. In addition, it utilizes a mixing layer to incorporate incomplete combustion effects and captures heat transfer effects through the combustor wall. The mixing layer represents the portion of the flow which has become “combustible,” meaning adequate mixing of the air and fuel has occurred, enabling the chemical reaction. In addition, the mixing layer, and hence the exit flow, are assumed to be

<sup>19</sup> As will be discussed in section 3.5, the vehicle baseline weight was approximated based on average values of several hypersonic vehicle concepts, many of which do include thermal protection systems and fuel storage considerations.

uniformly distributed across the area of the combustor. This assumption simplifies the analysis so that multiple streams, implying multiple energy, momentum, and conservation equations, need not be examined. The effects of ignoring multiple streams in one-dimensional flow are presented by Schindel [44], in which thrust losses of one percent can be expected. Schindel, however, performed this study at a fixed angle of attack, in which case somewhat larger losses may result. Nonetheless, for the purposes of this analysis, acceptance of such a small error is deemed reasonable.

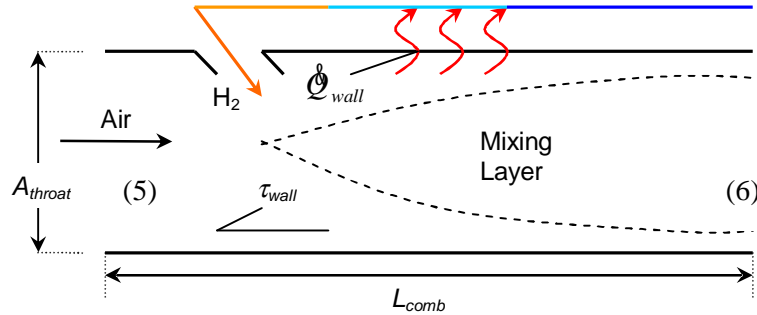
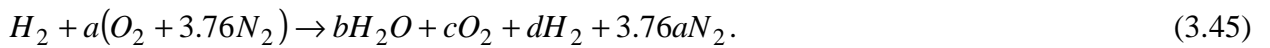


**Figure 3.12.** Combustor schematic [9].

In this study, no dissociation is assumed, due to the computational burden of solving finite rate kinetics. However, with the constraints placed on the inlet and an analysis of non-equilibrium and reaction rate chemistry of the constituents, at the temperatures and pressures encountered in this study, Markell demonstrates that this is a reasonable assumption [9]. The air is modeled as twenty-one percent oxygen and seventy-nine percent nitrogen, and, thus, the resulting reaction mechanism governing the hydrogen-air interaction on a mole basis is



As a result, the stoichiometric fuel to air ratio is found to be  $f_{st} = 0.0294$ .

### 3.3.2 Combustor Solution Procedure

An explicit, differential marching scheme, as given in Markell [9], is used to find the variations in Mach number, temperature, pressure, and irreversibilities along the length of the combustor. These changes are found using the properties delivered to the combustor by the inlet, which as mentioned above, have already been constrained to provide sufficient conditions for combustion. In addition, the parameter values summarized in table 3.7 are used.

**Table 3.7.** Combustor parameters.

Parameter		Value
Skin friction coefficient, $c_f$		0.015
Hydrogen heat of reaction, $h_{pr}$		119,954 kJ/kg
Hydrogen Injection Data	Mach Number, $M_{H_2}$	1.0
	Temperature, $T_{H_2}$	600 °K
	Pressure, $P_{H_2}$	101325 Pa
	Specific heat ratio, $\gamma_{H_2}$	1.4
	Constant pressure specific heat, $c_{pH_2}$	Constant <sup>20</sup>
	Angle	45°

The constant pressure specific heat from the inlet to the combustor is calculated from equation (3.46), where the temperature,  $T_5$ , varies along the length of the combustor, i.e.

$$c_{p_{air}} = 0.21c_{p_{O_2}}(T_5(x)) + 0.79c_{p_{N_2}}(T_5(x)). \quad (3.46)$$

Correlations using thermochemical property data from the JANAF tables are used to supply values of  $c_p$ <sup>21</sup> at various temperatures [45]. The specific heats of each constituent are specified by

$$c_{p_i} = c_{p_i}(T_5(x)) \quad (3.47)$$

where  $i$  denotes a constituent, i.e.  $O_2$ ,  $H_2O$ , etc. and  $T_5(x)$  is the temperature of the mixture at any position along the length of the combustor. The skin friction coefficient is set at 0.015, a relatively high value, to capture the impact of wall injectors and mixing on the flow. The mass flow rate of hydrogen enters the flow at an angle of forty-five degrees from the combustor wall at Mach 1. The injection angle is significant because directly impacts the x-direction flow momentum. In addition, a constant specific heat ratio of 1.4 for injected hydrogen is assumed, and the average specific heat at constant pressure for hydrogen is fixed based on the incoming static and total flow properties as suggested by Shapiro [42], i.e.

$$\bar{c}_{p_{H_2}} = \frac{h_{H_2}(T_5) - h_{H_2}(T_{5t})}{T_5 - T_{5t}}. \quad (3.48)$$

<sup>20</sup> The constant pressure specific heat is held constant during the injection process but may vary during each simulation based on the incoming flow properties as governed by equation (3.48).

<sup>21</sup> In addition to the constant pressure specific heat,  $c_p$ , the enthalpy,  $h$ , and entropy,  $s$ , are also calculated with polynomial fits as functions of temperature for each of the constituents listed in equation (3.47).

Lastly, the injection pressure and temperature are fixed at 101,325 Pa and 600°K, respectively. Thus, the total pressure of the injected hydrogen is calculated through the isentropic flow relation equation (3.12). The static temperature is necessarily higher than the hydrogen storage temperature, which should be cryogenic, due to the fact that it is absorbing energy by heat transfer to cool the combustor and nozzle walls. Exactly how the energy transfer is computed is discussed shortly.

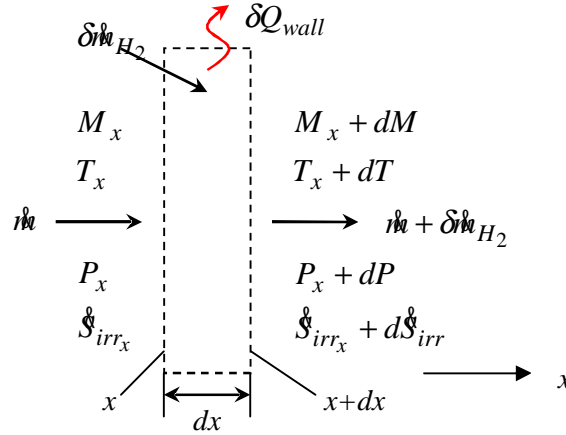


**Figure 3.13.** Combustor differential element [9].

A control volume, represented in figure 3.11, can be used to illustrate the explicit solution procedure used to solve the combustor component. As in the inlet solution for the conceptual diffuser, table 3.2 can again be used to solve for the flow properties of the combustor. For this component, however, changes due to total enthalpy change,  $dH^{22}$ , across the differential element, and heat transfer,  $\delta Q$ , through the wall to cool the combustor and nozzle, wall friction, and hydrogen mass flow rate addition must be considered. As a result, the following relations for Mach number, temperature, and pressure can be written:

$$\begin{aligned} \frac{dM}{M_x} = & \frac{1 + \gamma M_x^2}{2(1 - M_x^2)} \frac{dH - \delta Q_{wall}}{c_p T_x} + \frac{\gamma M_x^2 \left(1 + \frac{\gamma - 1}{2} M_x^2\right)}{2(1 - M_x^2)} \left( \frac{4C_f dx}{D_h} - 2y \frac{\delta\dot{m}_{H_2}}{\dot{m}} \right) \\ & + \frac{\left(1 + \gamma M_x^2\right) \left(1 + \frac{\gamma - 1}{2} M_x^2\right)}{1 - M_x^2} \frac{\delta\dot{m}_{H_2}}{\dot{m}}, \end{aligned} \quad (3.49)$$

<sup>22</sup> See equation 3.53.

$$\frac{dT}{T_x} = \frac{1 - \gamma M_x^2}{1 - M_x^2} \frac{dH - \delta Q_{wall}}{c_p T_x} - \frac{\gamma(\gamma - 1) M_x^4}{2(1 - M_x^2)} \left( \frac{4C_f dx}{D_h} - 2y \frac{\delta \dot{m}_{H_2}}{\dot{m}} \right) - \frac{(\gamma - 1) M_x^2 (1 + \gamma M_x^2)}{1 - M_x^2} \frac{\delta \dot{m}_{H_2}}{\dot{m}}, \quad (3.50)$$

and

$$\frac{dP}{P_x} = - \frac{\gamma M_x^2}{1 - M_x^2} \frac{dH - \delta Q_{wall}}{c_p T_x} - \frac{\gamma M_x^2 [1 + (\gamma - 1) M_x^2]}{2(1 - M_x^2)} \left( \frac{4C_f dx}{D_h} - 2y \frac{\delta \dot{m}_{H_2}}{\dot{m}} \right) - \frac{2\gamma M_x^2 \left( 1 + \frac{\gamma - 1}{2} M_x^2 \right)}{1 - M_x^2} \frac{\delta \dot{m}_{H_2}}{\dot{m}}. \quad (3.51)$$

In each of these equations,  $x$  denotes the property at the entrance to the differential control volume, (see figure 3.11). In addition,  $y$  (not to be confused with ratio of specific heats,  $\gamma$ ), is defined as the ratio of  $x$ -component injection velocity to combustor channel flow velocity at  $x$  (occurring also in the  $x$ -direction). The differential mass flow rate of hydrogen added to the flow, denoted by  $\delta \dot{m}_{H_2}$ , is calculated through the use of mixing and combustion efficiency models<sup>23</sup>. The hydraulic diameter of the flow,  $D_H$ , is defined as four times the cross sectional area divided by the perimeter. In a one-dimensional, constant rectangular geometry with unit vehicle width, this reduces to

$$D_h = \frac{4A_x}{P} = \frac{4w_{veh} h_{throat}}{2(w_{veh} + h_{throat})} = \frac{2h_{throat}}{1 + h_{throat}}. \quad (3.52)$$

The total enthalpy term,  $dH$ , is calculated taking into account the enthalpy changes due to the chemical reaction and the temperature difference between the injection total temperature,  $T_{t_{H_2}}$ , and the mainstream temperature,  $T_x$ , i.e.

$$dH = dh_{pr} - \left[ \bar{c}_{p_{H_2}} (T_x - T_{t_{H_2}}) + \frac{u_x^2}{2} \right] \frac{\delta \dot{m}_{H_2}}{\dot{m}}, \quad (3.53)$$

---

<sup>23</sup> These models are governed by equations (3.65) through (3.71).

where  $dh_{pr}^{24}$  is the incremental heat release and  $u_x$  is the flow velocity at position  $x$  along the length of the combustor.

The wall heat loss ( $\delta Q_{wall}$ ) prediction technique chosen for this study is the Eckert reference enthalpy method which is specifically suggested by Heiser and Pratt for hypersonic airbreathing propulsion applications [3]. It is assumed in this prediction that average or reference enthalpies and temperatures in the boundary layer can represent the actual, varying properties in the boundary layer [3]. This method has proven to typically be within ten to twenty percent of the actual heat transfer value, and its advantage is that the heat transfer over the length of the combustor need be solved only once at the entrance to the combustor.

To begin with, the reference<sup>25</sup> enthalpy and recovery factors, in equations 3.50 and 3.51 respectively, must be solved such that

$$h^* = \frac{h_e + h_w}{2} + 0.22r \frac{u_e^2}{2} \quad (3.56)$$

and

$$r = \frac{h_{aw} - h_e}{\frac{u_e^2}{2}} \quad (3.57)$$

The reference enthalpy is a function of the static flow enthalpy,  $h_e$ , design static wall enthalpy,  $h_w$ , recovery factor,  $r$ , and flow velocity,  $u_e$ . Again, all of the enthalpies are found from empirical correlations as a function of static temperature. Once the reference enthalpy is found, the reference temperature,  $T^*$ , is found by iteratively substituting values of temperature into the enthalpy polynomial program until Since this method is only applied at the combustor entrance, station “5” can replace the subscript “e” in the previous and following equations (see figure 3.10). The desired wall enthalpy is a function of the desired static design temperature,  $T_w$ . This value is typically chosen based on material limitations, which for this study was selected as 1088 °K. The recovery factor represents how the adiabatic wall enthalpy,  $h_{aw}$ , influences the reference enthalpy value. The adiabatic wall enthalpy is a function of the total temperature, where the total temperature is found by bringing the flow adiabatically to rest at the wall *without* cooling (see equation (3.12)). This can be visualized in figure 3.14.

---

<sup>24</sup> The incremental heat release is calculated by equation (3.71).

<sup>25</sup> The average or reference states are denoted by \*.

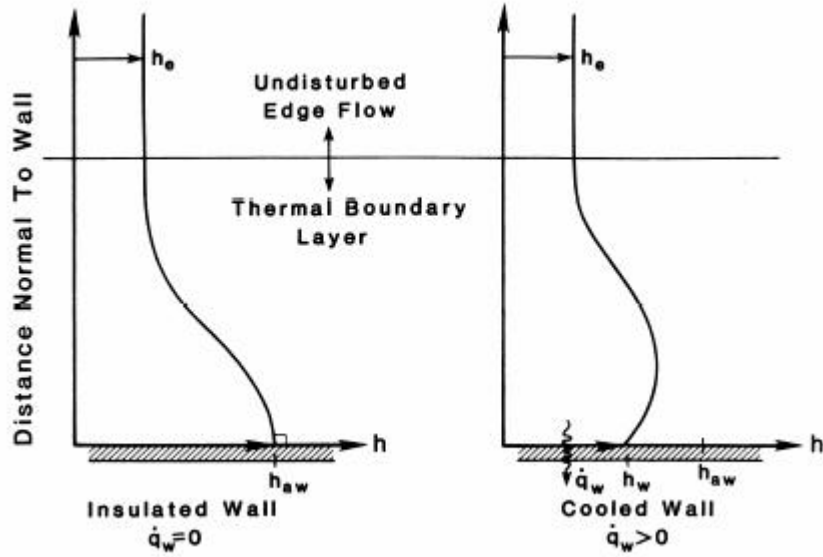


Figure 3.14. Wall enthalpies with and without heat transfer [3].

The differential amount of heat that must be removed,  $\delta Q_{wall}$ , is calculated by

$$\delta Q_{wall} = \frac{\dot{q}_{wall} A_x dx}{h_e} \quad (3.58)$$

where the convective wall heat flux in turbulent flow,  $\dot{q}_{wall}$ , is defined as

$$\dot{q}_{wall} = \frac{0.0287 P_e u_e (h_{aw} - h_w)}{RT^* \text{Pr}^{*2/5} \text{Re}_x^{*1/5}} \quad (3.59)$$

In this equation, the reference Reynolds and Prandtl numbers are

$$\text{Re}_x^* = \frac{P_e u_e L_{comb}}{RT^* \mu^*} \quad (3.60)$$

and

$$\text{Pr}^* = r^{1/3} \quad (3.61)$$

where

$$\mu^* = 1.46(10^{-6}) \frac{T^{*3/2}}{T^* + 111} \quad (3.62)$$

Now, in order to calculate how much energy the hydrogen, entering the combustor at 600 °K, can absorb starting from an initial liquid storage temperature,  $T_{tank}$ , which is below the vaporization temperature of 20.35 °K, the following equation is used:

$$h_{fc} = c_{p_{liqH_2}} (T_{vapH_2} - T_{tank}) + h_{vapH_2} + c_{p_{H_2 100}} (100 - T_{vapH_2}) + c_{p_{H_2 400}} (400 - 100) + c_{p_{H_2 600}} (T_{H_2} - 400). \quad (3.63)$$

As a result, the total flow rate of hydrogen needed,  $\dot{m}_{H_2, need}$ , to cool the combustor is found using.

$$\dot{m}_{H_2, need} = \frac{1.5 \dot{Q}_{wall}}{h_{fc}}. \quad (3.64)$$

An additional 0.5 is added to the necessary flow rate to account for the cooling needed in the nozzle. This approximation eliminates the requirement of iterating between combustor and, thus, results in a non-thermally balanced vehicle. However, the factor of 0.5 is representative of nozzle cooling requirements [46], and, hence, this approximation is deemed justified in order to avoid an additional computational burden which would indeed prove prohibitive for the mission-level system optimization envisioned. In addition, when  $\dot{m}_{H_2, need}$  exceeds the desired mass flow rate of fuel for propulsion, the excess fuel is returned to the tank.

Now, in order to model the injection process, incremental amounts of fuel are absorbed into the mixing layer, which, as previously mentioned, spans the entire flow area. The mass flow rate of the unabsorbed hydrogen stream at any axial combustor location is calculated as

$$\dot{m}_{H_2}(x) = \dot{m}_{air5} f_{st} \phi (1 - \eta_M(x)) \quad (3.65)$$

where  $\phi$  is the equivalence ratio given in equation (3.46), and  $\eta_M$  is the mixing efficiency given by

$$\eta_M(x) = \frac{1 - e^{-\frac{Ax}{L_m}}}{1 - e^{-A}} \quad (3.66)$$

where  $A$  is a fit parameter for near-field mixing and  $L_m$  is the distance for minor mixant to be depleted. Typically,  $A$  varies from 1 to 5, and for this analysis is chosen to be 4.5 [9, 47]. From the above equation, the mixing efficiency equals unity when combustor length equals the length for the minor mixant to be depleted, i.e. when  $x = L_m$ . If the equivalence ratio is less than or equal to one, the fuel is

considered the minor mixant, otherwise, the air is considered the minor mixant. The axial distance at which the minor mixant is depleted is given by

$$L_m \cong 0.179bC_m e^{1.72\phi} \quad \phi \leq 1 \quad (3.67)$$

and

$$L_m \cong 3.333bC_m e^{-1.204\phi} \quad \phi > 1 \quad (3.68)$$

Where  $b = A_{Throat}$  and  $C_m$  is the mixing constant [9]. The mixing constant usually varies between 25 and 60 and is chosen to be  $C_m = 47$  for this analysis. With the mass flow rate of the unabsorbed hydrogen stream known at each step, the amount of fuel absorbed into the mixing layer can be calculated by

$$\delta \dot{m}_{H_2} = \dot{m}_{H_2,x} - \dot{m}_{H_2,x+dx} \quad (3.69)$$

It should be noted that immediate and continuous absorption starting at the entrance to the combustor is assumed for this study. This assumption, of course, disregards physical injector positioning or ignition delay contributions.

With a known mixing model, a combustion efficiency model is required to calculate the incremental energy released by the fuel. It is assumed that, contrary to the mixing efficiency, the maximum value that the combustion efficiency can ever reach is 0.9. As seen in figure 3.15, the combustion efficiency is also an exponential function; however, it grows at a slower rate than the mixing efficiency. The relations for the combustion efficiency model and the incremental energy release at a given axial location are described by, respectively,

$$\eta_b(x) = 1 - e^{\frac{-Bx}{L_m}} \quad (3.70)$$

and

$$dh_{pr} = \eta_b(x+dx)h_{pr} - \eta_b(x)h_{pr} \quad (3.71)$$

The coefficient  $B$  is a fit parameter set to 2.3 to provide the characteristics shown in figure 3.12.

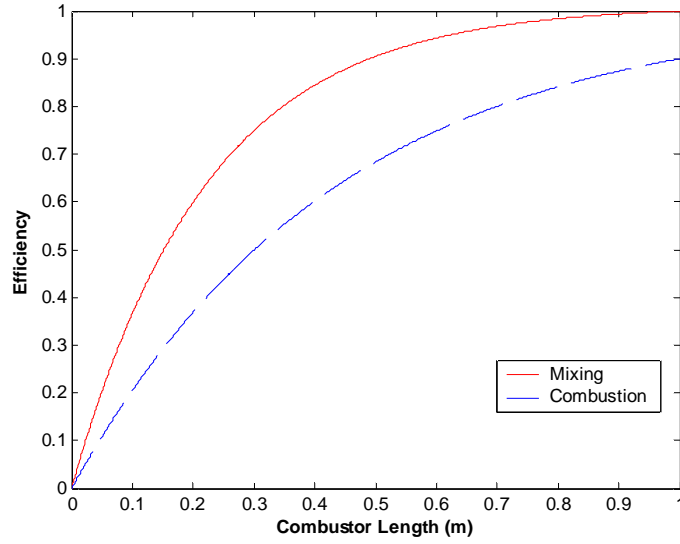


**Figure 3.15.** Mixing and combustion efficiencies versus combustor length [9].

### 3.3.3 Combustor Loss Mechanisms

Unlike the inlet, the introduction of hydrogen to the flow introduces new mechanisms for loss. In addition to friction, heat transfer, fuel/air mixing, and incomplete combustion occur. The sum of these individual losses is the total loss attributed to the combustor, i.e.

$$\dot{S}_{irr_{comb}} = \dot{S}_{irr_{frict}} + \dot{S}_{irr_{ht}} + \dot{S}_{irr_{inc\ comb}} + \dot{S}_{irr_{mix}}. \quad (3.72)$$

The entropy generation rate due to irreversibility for each mechanism is calculated at each differential step and summed over the length of the combustor, given by

$$d\dot{S}_{irr_{frict}} = \frac{\dot{m} C_f u_x^2 dA_{surf}}{2T_x A_x}, \quad (3.73)$$

$$d\dot{S}_{irr_{ht}} = \delta\dot{Q}_{wall} \left( \frac{1}{T_{H_2}} - \frac{1}{T_w} \right), \quad (3.74)$$

$$d\dot{S}_{irr_{inc\ comb}} = \dot{m}_{H_2} dh_{pr} \left( \frac{1}{T_{H_2}} - \frac{1}{T_x} \right), \quad (3.75)$$

and

$$d\dot{S}_{irr_{mix}} = \frac{\delta\dot{Q}_{wall}}{T_w} - \frac{\dot{m}_{H_2} dh_{pr}}{T_x} - d\dot{S}_{irr_{fric}} + \sum_1^j \dot{m}_j \left( c_{p_j} \ln \frac{T_{x+dx}}{T_x} - R \ln \frac{P_{x+dx}}{P_x} - R \ln \frac{x_{j_{x+dx}}}{x_{j_x}} \right). \quad (3.76)$$

The mass fraction,  $x_j$ , is calculated from

$$x_j = \frac{y_j M_{w_j}}{M_w}, \quad (3.77)$$

where  $y_j$  is the mole fraction and  $M_{w_j}$  is the molecular weight of each constituent in the main stream. Three different control volumes are selected to calculate the irreversibility rates in the above equations. The rate of entropy produced by heat transfer is calculated based on a control volume containing the combustor walls, while that for incomplete combustion losses are determined with a control volume surrounding the mixing layer interface. The rates of entropy generation due to mixing and friction losses are determined using the differential element as shown in figure 3.13.

Now, in order to calculate the mole fractions the mixing model specifies the mass flow rate of hydrogen at position  $x$  in the main stream, all of which is assumed reacted by the time the flow exits the differential control volume, at position  $x + dx$ . Thus, using the molecular weights, the molar flow rates are known and used to calculate the reaction coordinate rate,  $\dot{\xi}$ , from

$$\dot{m}_{H_{2_{out}}} = \dot{m}_{H_{2_{in}}} + \nu_{H_2} \dot{\xi} \quad (3.78)$$

where  $\nu_{H_2}$  is the stoichiometric coefficient of hydrogen equal to 1. With complete combustion,  $\dot{m}_{H_{2_{out}}}$  is zero and from the mixing model,

$$\dot{m}_{H_{2_{in}}} = \dot{m}_{H_{2_x}} - \dot{m}_{H_{2_{x+dx}}} = \delta \dot{m}_{H_2}. \quad (3.79)$$

Thus, from the reaction mechanism, the resulting reaction coordinate rate is found to be

$$\dot{\xi} = \frac{\dot{m}_{H_{2_{x+dx}}} - \dot{m}_{H_{2_x}}}{-1} = \delta \dot{m}_{H_2}. \quad (3.80)$$

The remaining molar flow rates can be computed using

$$\dot{m}_{O_{2_{x+dx}}} = \dot{m}_{O_{2_x}} + (-0.5) \dot{\xi}, \quad (3.81)$$

$$\dot{m}_{N_{2,x+dx}} = \dot{m}_{N_{2,x}}, \quad (3.82)$$

$$\dot{m}_{H_2O_{x+dx}} = \dot{m}_{H_2O_x} + 1\dot{m}, \quad (3.83)$$

and

$$y_j = \frac{\dot{m}_j}{\sum_1^j \dot{m}_j}. \quad (3.84)$$

where the values -0.5 and 1 in equations (3.81) and (3.83), respectively, are the stoichiometric coefficients of O<sub>2</sub> and H<sub>2</sub>O, respectively. With these equations, each differential element is solved until the conditions at the entrance to the nozzle are known. To be sure that the combustor is providing adequate conditions for expansion, however, certain combustor constraints must be met.

### 3.3.4 Combustor Constraints

In addition to the imposed range, there is an added constraint on combustor length. The length may not exceed that which is required for the minor mixant to be depleted. This essentially ensures that reactions are occurring throughout the length of the combustor. Without this constraint, friction and heat transfer losses would continue after combustion has ceased, resulting in an undesirable combustor length. Secondly, the Mach number exiting the combustor must be greater than unity. A subsonic exit Mach number would produce catastrophic circumstances, since the nozzle is designed strictly for supersonic operation.

## 3.4 Nozzle Component Model

The final component of the propulsion sub-system is responsible for relieving the high temperatures and pressures exiting the combustor and converting them into a velocity much greater than that at the inlet. In supersonic flow, this is accomplished by an expansion process through a diverging channel which is conventionally axially symmetric. However, as expressed in Chapter 1, these tend to be too bulky and create excessive drag during hypersonic flight. Thus, free expansion surfaces are utilized instead. How flows are modeled through this process and the primary influences on nozzle design are the subject of the next discussion.

### 3.4.1 Nozzle Design and Variables

When the constituents from the combustor enter the nozzle, chemical reactions are ceased, i.e. frozen chemical equilibrium is assumed; and, thus, the mole and mass fractions are constant throughout the length of the nozzle. A schematic of the nozzle is presented in figure 3.16. The products of combustion enter at position “6” and exit at position “7”. As in the combustor, heat transfer and friction affect the flow through the nozzle.

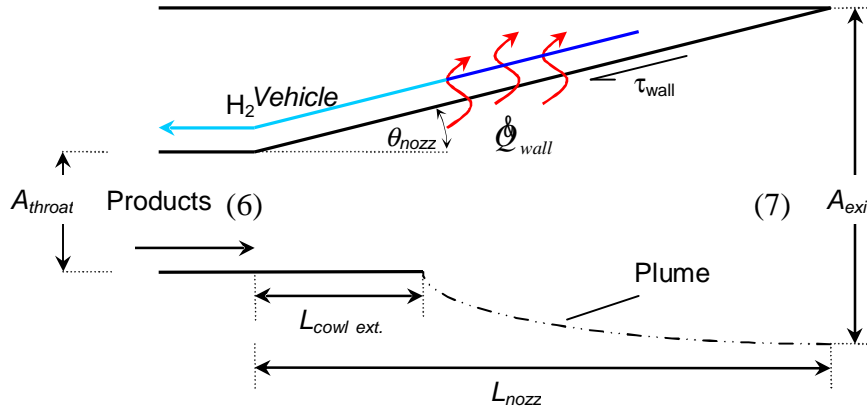


Figure 3.16. Nozzle schematic.

There are two independent design decision variables in the nozzle as shown in table 3.8. The first is the nozzle expansion angle. This variable determines what value of area relief per unit length is provided to the flow by the free expansion surface and is fixed to fall between 8 and 18 degrees. Below 8 degrees, the nozzle does not produce any appreciable thrust; and, above 18 degrees, experimental results reveal operating conditions which deviate from predicted values [48].

Table 3.8. Nozzle design decision variables.

Variable	Symbol	Imposed Limits
Nozzle expansion angle [°]	$\theta_{nozz}$	$8 \leq \theta_{nozz} \leq 18$
Percent nozzle length	$\%_{nozz}$	$0 \leq \%_{nozz} \leq 0.25$

The second variable is what percentage the cowl extension is of the total nozzle length or

$$\%_{nozz} = \frac{L_{cowl\ ext.}}{L_{nozz}} \quad (3.85)$$

This variable, in one-dimensional flow, impacts the force and moment imparted on the vehicle by the pressure inside the nozzle. Figure 3.17 shows this relationship. In addition, the cowl length (see figure 3.16) affects the position at which the *plume* starts, which is discussed in the following section. This

length is chosen as a percentage of nozzle length because the latter varies, and the cowl extension rarely exceeds twenty-five percent of the nozzle length of hypersonic vehicle concepts due to cooling and weight restrictions [5, 47]. Furthermore, although the length of the nozzle can vary, it is not an independent (or decision) variable because the total vehicle length is assumed fixed, and since the inlet and combustor lengths vary, they dictate the nozzle length. A sample of the the effect of cowl extension into the nozzle on trim and lift for an otherwise fixed geometry is shown in figure 3.17.

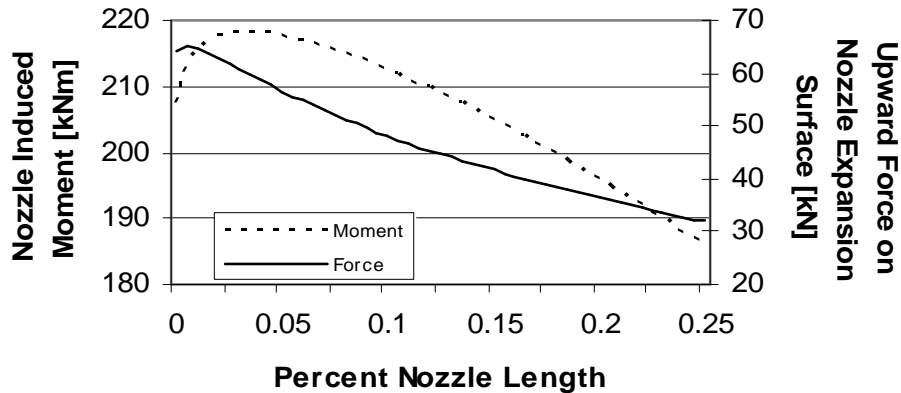


Figure 3.17 The influences of cowl length on vehicle force and moment balances.

### 3.4.2 Nozzle Solution Procedure

Again, the differential marching scheme provided by Shapiro [42] is used to calculate the flow properties in the nozzle. Unlike the combustor, however, mass is no longer being added and area change must be taken into account. A differential control volume for the nozzle is shown in figure 3.18. The area change is exaggerated to illustrate the geometric influences.

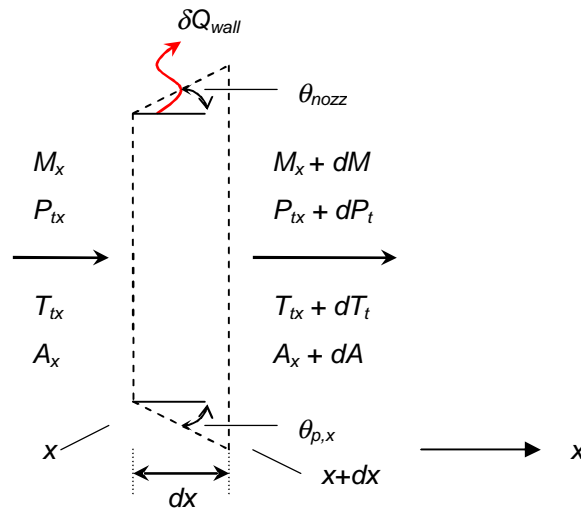


Figure 3.18. Nozzle differential element.

The influences of heat transfer and friction on Mach number are given as functions of total pressure and total temperature change. These relationships are as follows:

$$\frac{dM}{M_x} = \frac{\left(1 + \frac{\gamma-1}{2} M_x^2\right)}{1 - M_x^2} \left[ -\frac{dA}{A_x} + \frac{1 + \gamma M_x^2}{2} \frac{dT_t}{T_{t,x}} + 2\gamma M_x^2 C_f \frac{dx}{D_h} \right], \quad (3.86)$$

$$\frac{dP_t}{P_{t,x}} = -\frac{\gamma M_x^2}{2} \left( \frac{dT_t}{T_{t,x}} + \frac{4C_f dx}{D_h} \right), \quad (3.87)$$

and

$$\frac{dT_t}{T_{t,x}} = \frac{1}{\left(1 + \frac{\gamma-1}{2} M_x^2\right)} \frac{-\delta Q_{wall}}{c_p T_x}, \quad (3.88)$$

where the coefficient of friction for the nozzle is assumed fixed at 0.005, which is a third of the value assumed in the combustor, as suggested by Riggins [46].

Again, the heat transfer in the nozzle ( $\delta Q_{wall}$ ) is calculated based on the Eckert reference enthalpy method. Since this method is dependent on the conditions at the entrance to the nozzle, similar to the combustor, this method tends to approximately double the actual value of heat transfer in the nozzle [46]. As a result, the heat transfer is driven to zero at the nozzle exit, and an average value of  $\delta Q_{wall} = Q_{eck} dx/2$  is assumed removed from each differential step. This provides a heat loss in the nozzle consistent with the assumption made for heat loss in the combustor, and once again costly iterations are avoided. A more accurate method of modeling, not employed here, would be to provide an exponential decaying function with an average value of  $Q_{eck}/2$ , in which the majority of the nozzle heat loss occurs closest to the combustor exit and asymptotically approaches zero at the nozzle exit.

Now, returning to equation (3.86), the area change per differential step is given by

$$dA = dx \left( \tan(\theta_{p,x}) + \tan(\theta_{nozz}) \right). \quad (3.89)$$

During internal expansion, i.e. along the cowl extension before the plume begins, the plume angle is equal to zero and the only area relief available to the nozzle is due to the upper surface geometry. In addition, two separate hydraulic diameters must be specified for the internal and external expansions, since in the case of internal expansion, the flow is surrounded by four walls, as illustrated in the three

dimensional representation of figure 3.19. The internal hydraulic diameter can be written per unit width of the vehicle as

$$D_h = \frac{4A_x}{P_x} = \frac{4w_{veh}h_x}{2(w_{veh} + h_x)} = \frac{2h_x}{1 + h_x}. \quad (3.90)$$

The external hydraulic diameter is

$$D_h = \frac{4A_x}{P_x} = \frac{4w_{veh}h_x}{w_{veh}} = 4h_x, \quad (3.91)$$

with  $P_x$  equal to the perimeter of the flow cross-sectional area  $A_x$ .

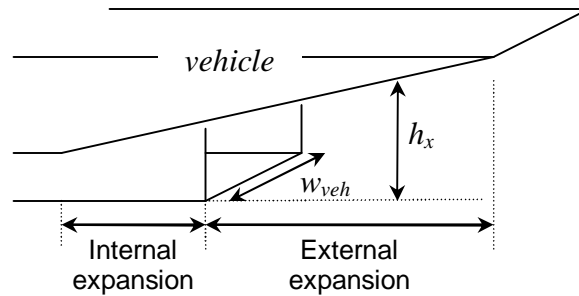


**Figure 3.19.** Three-dimensional nozzle view.

Finally, how the plane angle changes along the length of the nozzle must be addressed. To begin with, a plume results from the large pressure gradient between the flow exiting the internal section of the nozzle, or combustor if there is no extension, and the near freestream flow conditions just below the cowl extension. Thus, as the flow exits the internal portion of the nozzle, the flow inside immediately expands through a corner centered expansion and the flow below the cowl turns acutely (through an oblique shock). This can be modeled as two flows along an imaginary boundary which dictates their behavior. For example, the nozzle flow expands through turning angle of  $\nu_{p,x}$ , while the oblique shock compresses the flow under the cowl through the same angle. This process is illustrated in figure 3.20. This continues along the length of the nozzle at every incremental step until the two pressures equalize. Smaller and smaller expansions and oblique shocks occur along the nozzle length until a parabolic plume shape emerges (see figure 3.13). The details of this process are given in Del Guidice, Dash, and Kalben [49].

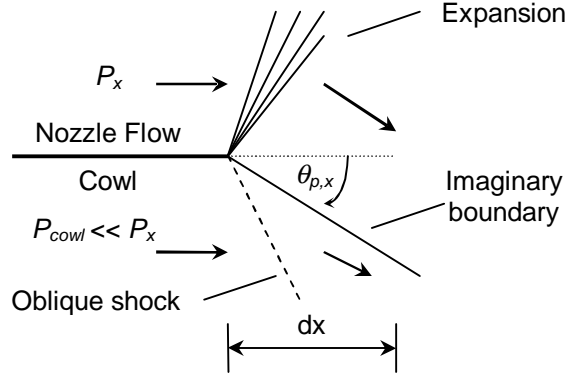


**Figure 3.20.** Plume interaction for a differential element.

From figure 3.20, finding  $\theta_{p,x}$  at every step can be accomplished by iteratively solving simultaneously the oblique shock and Prandtl-Meyer equations until they agree upon an angle. However, since the solution of the Prandtl-Meyer equations already involves iteration and is thus computationally expensive, this is an undesirable approach for purposes of large-scale optimization. Fortunately, an approach based on the Modified Newtonian theory can be substituted to produce the same results.

Modified Newtonian theory, which is more accurate than Newtonian theory, provides a relationship for matching the nozzle and freestream pressures by introducing a non-dimensional pressure coefficient,  $C_{p,com}$  [50]. Thus, the pressures are equalized when  $P_x = P_{cowl,x}$ . With the pressure of the nozzle flow known from equations 3.86 through 3.88, the pressure under the cowl is equal when

$$P_x = P_{cowl} \left[ 1 + \frac{\gamma M_{cowl}^2}{2} C_{p,com}(\gamma_{cowl}, M_{cowl}, \theta_{p,x}) \right]. \quad (3.92)$$

The pressure coefficient, as shown, is a function of external specific heat ratio, Mach number, and plume expansion angle, and thus, the plume angle can be found iteratively with the following relation for the pressure coefficient:

$$C_{p,com} = \frac{2 \sin^2(\theta_{plume})}{\gamma M_{cowl}^2} \left\{ \left[ \frac{(\gamma+1)^2 M_{cowl}^2}{4\gamma M_{cowl}^2 - 2(\gamma-1)} \right]^{\frac{\gamma}{\gamma-1}} \left[ \frac{2\gamma M_{cowl}^2 - (\gamma-1)}{\gamma+1} \right] - 1 \right\} \quad (3.93)$$

What results is a linear plume shape at each differential step. The sum of these yields a parabolic shape like that shown in figure 3.16.

### 3.4.3 Nozzle Loss Mechanisms

The two factors responsible for generating entropy in the nozzle are friction and heat transfer. An entropy balance yields

$$\dot{S}_{irr, nozz} = \frac{\dot{m}_{mix}}{MW_{mix}} \left( \sum_1^j y_j s_{j_7} - \sum_1^j y_j s_{j_6} - R \ln \frac{P_7}{P_6} \right) + \frac{\dot{Q}_{wall}}{T_w} \quad (3.94)$$

where the individual molecular entropy values referenced from the JANAF tables are used to find the molar specific entropy at both the inlet and exit of the nozzle. As in the combustor,  $T_w$  is assumed to be roughly 1100 8K. Because the plume boundary is essentially imaginary, the losses associated with the shock/expansion process and drag associated with the increased exhaust area are drastically smaller than if a physical boundary were present and, thus, their contributions are neglected [46].

### 3.4.4 Nozzle Constraints

Two constraints are placed upon the nozzle. This first is with regard to the plume. A problem of finding the plume angle with either shock-expansion iterations or through the Modified Newtonian theory is that above certain pressure ratios,  $P_x/P_{cowl}$ , there exists no angle which can equalize the pressures. This relates to the discussion regarding maximum expansion angles in Section 3.1.2. As a result, when pressure ratios exceed a specified value (see figure 3.21), a plume angle of 75 degrees is assumed. This value is chosen to keep the area change reasonable for the one-dimensional flow assumptions discussed previously. As angles approach 90 degrees, the area change becomes infinite, as can be discovered from equation (3.83). To resolve this issue, the more general compressible pressure coefficient from Newtonian theory, shown below, is utilized, i.e.

$$C_{p, com} = 2 \sin^2(\theta_{p,x}) \quad (3.95)$$

In this method, the maximum allowable pressure ratio can easily be found from

$$\frac{P_x}{P_{cowl}} = \left\{ 1 + \frac{\gamma M_{cowl}^2}{2} [2 \sin^2(75^\circ)] \right\}. \quad (3.96)$$

Thus, at each Mach number underneath the cowl, the maximum pressure ratio is known, and a total solution for the flow can now be performed. Figure 3.21 shows the pressure ratio limit over the Mach 3 to Mach 12 flight regime. Note that since the flow Mach number under the cowl is not equal to the

freestream flow Mach number (due to the forebody/inlet shocks and varying vehicle angles of attack) a continuous range of values must be considered.

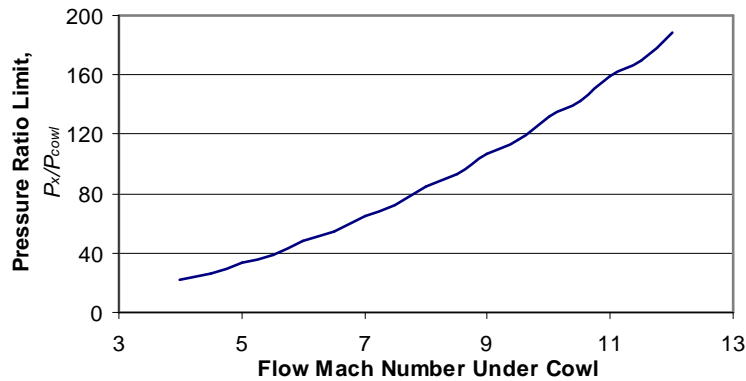


**Figure 3.21.** Pressure ratio limit vs. beneath cowl flow Mach number.

The second constraint requires that the pressure in the nozzle does not fall below 400 Pa. This constraint guarantees that excessive (unrealistic) backpressures are avoided.

### 3.4.5 Nozzle Design Considerations

Initially, a two-dimensional program was developed to model the flow in the nozzle using the method of characteristics [41]. The goal of undertaking this approach began while trying to understand why the undersurfaces of many conceptual vehicles were curved [5]. This method is often used to calculate axisymmetric nozzle contours and can do the same for free expansion scramjets. Shown in figure 3.22, multiple characteristic lines, or Mach waves, as was discussed with regard to Prandtl-Meyer expansions, are drawn to accurately describe the flow direction and Mach number in each region between the lines. In essence, in two-dimensional flow, the Prandtl-Meyer equations are assigned a finite length for which they are valid. They are utilized to model the initial fan, and the reflections of that fan off the cowl surface determine many interesting nozzle attributes. The upper surface contour is shaped based on the cancellation of reflecting waves, i.e. a flat nozzle surface would yield undesirable reflections, whereas the curved surface in the figure is contoured necessarily to cancel these reflecting waves. For example, in the figure described, the ideal cowl length, the length at which the last fan is reflected, is roughly 3.3 meters, of an assumed eight meter nozzle. Eight meters is not necessarily the ideal length, since an extended length could provide more vehicle lift. It is simply the length needed to correct the final expansion wave and align the flow to the axial direction. In addition, in actuality, the

maximum cowl extension length that can be used for the vehicle is often limited by its overall weight and the ability to cool it [46].

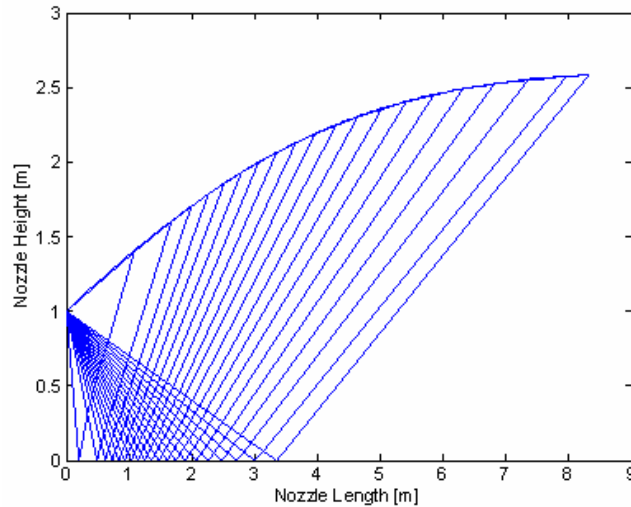


**Figure 3.22.** 2-D method of characteristics applied to a nozzle with 25° nozzle entrance expansion angle and 1 meter throat height.

Ultimately, the program required too much computational time and had to be abandoned. In addition, the method of characteristics is based on irrotational, isentropic flow, and thus must be modified from its current form to include heat transfer and frictional effects (loss mechanisms). This technique is also employed for the design of isentropic inlets, and thus, a curved forebody and inlet geometry would result.

### 3.5 Airframe Sub-system Model

The primary objective of the aerodynamic or airframe sub-system is to guarantee that forces and moments on the aircraft are balanced throughout the entire mission. As a result, detailed force accounting, center of mass, and lift and drag calculations are just a few of the computations performed by this sub-system to guarantee steady and level flight. In addition to describing how these calculations are made, this section also discusses the loss mechanisms for which the aerodynamics of the airframe sub-system is responsible.

### 3.5.1 Atmospheric Flight

Figure 3.23 shows the forces acting on a hypersonic vehicle at a flight path angle of  $\nu$ . These forces are the thrust,  $T$ , drag,  $D$ , lift,  $L$ , and weight,  $W$ . The drag acts along the direction of vehicle velocity,  $V$ , while the lift is perpendicular. The thrust acts along the vehicle centerline. The vehicle weight of course, equal to the mass multiplied by the gravitational constant, always acts in the downward vertical direction. The angle of attack,  $\alpha$ , is the angle at which the vehicle centerline is aligned to the direction of the velocity. Both the angle of attack and the flight path angle are greatly exaggerated in the figure. Combined they do not exceed five degrees in this study because of the sensitivity of inlet shock tailoring system.

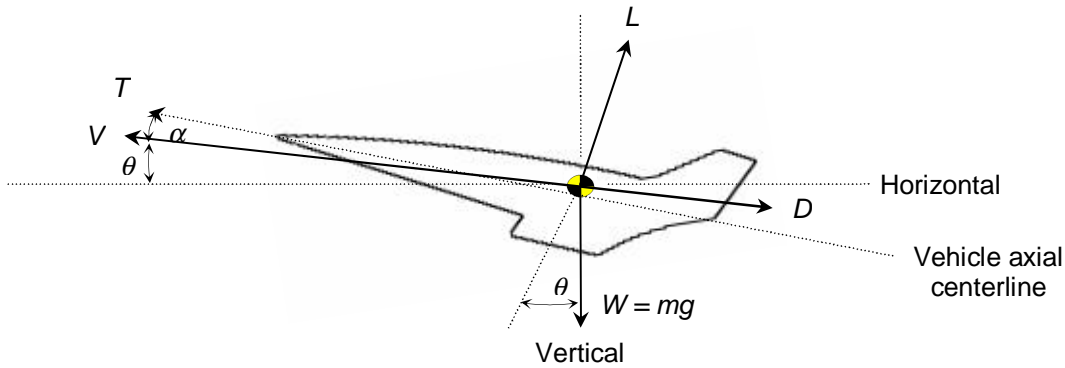


**Figure 3.23.** Forces acting on an aerospace vehicle during flight.

The lift and drag of a body can be calculated from the relations given below, assuming that the lift and drag coefficients,  $C_L$  and  $C_D$ , are known. Thus,

$$L = q_0 C_L S \quad (3.97)$$

and

$$D = q_0 C_D S \quad (3.98)$$

In the previous equations,  $S$  is the reference area and  $q_0$  is the dynamic pressure expressed as

$$q_0 = \frac{\rho_0 V_0^2}{2}. \quad (3.99)$$

For the flight condition known as cruise, the flight path angle and angle of attack are both nearly zero; therefore, the thrust and drag act in the horizontal direction, and the lift and weight act in the vertical direction. Thus, to maintain steady, level flight, it is necessary that the lift equal the weight and the

thrust equal the drag. These balances become slightly more complicated when accelerations, climbs, and turns are necessary. How to handle these situations is discussed thoroughly in Chapter 4.

For hypersonic vehicles, it is desirable to obtain the maximum amount of lift with a minimum reference area; thus, vehicles are typically designed to fly near their highest allowable dynamic pressure [3]. The consequences that accompany a large design dynamic pressure are that the drag and skin friction are comparatively large as well. The range of dynamic pressures for hypersonic vehicles is approximately 20,000 – 90,000 Pa, where the upper bound is typically governed by airframe structural integrity and the lower bound by unreasonable areas required to attain a specified lift. Taking into consideration these facts, a design dynamic pressure of 85,000 Pa was chosen for this study.

A great deal of analysis is required to calculate the lift and drag of a hypersonic vehicle, particularly because at such high speeds the integrated vehicle fuselage/engine itself provides lift. This is quite different from conventional aircraft in which the majority of the lift is attributed to the wings. Thus, force accounting, or resolving all of the forces on the vehicle, is necessary to compute the required thrust and lift for the aircraft to perform its mission.

### 3.5.2 Force Accounting

Various methods of force accounting in hypersonic propulsion are discussed in the literature [51, 52]. The goal of each of these is to ensure that all forces acting on the vehicle are taken into account, and none is counted multiple times. Typically, the vehicle forces due to streamthrust, pressure, and friction are charged either to the propulsion or airframe sub-systems, the division of which is represented by the dotted line in figure 3.24, where the  $x$ -component is considered parallel to the vehicle axial centerline, and the  $y$ -component is perpendicular. If the forces under consideration are charged to the airframe, they are resolved into  $x$  and  $y$ -components. If they are charged to the propulsion sub-system, only the  $y$ -component is considered, and the  $x$ -component is assumed taken into account by the streamthrusts,  $F_1$  and  $F_7$  in the figure below. The choice of sub-system interface in this study only affects the assumption stated above.

All of the forces shown in figure 3.24, except for the nozzle pressure force,  $F_{n,p}$ , are assumed to act at the center of their respective locations. For example, while the pressure force due to the forebody,  $F_{fb,p}$ , acts along the entire forebody surface, a net force is assumed to act at the midpoint of the forebody in the direction normal to the surface. This assumption simplifies the force and moment balance

equations. The nozzle is a special case because the pressure along its length varies, and thus its pressure forces and moment contributions are calculated at each differential step.

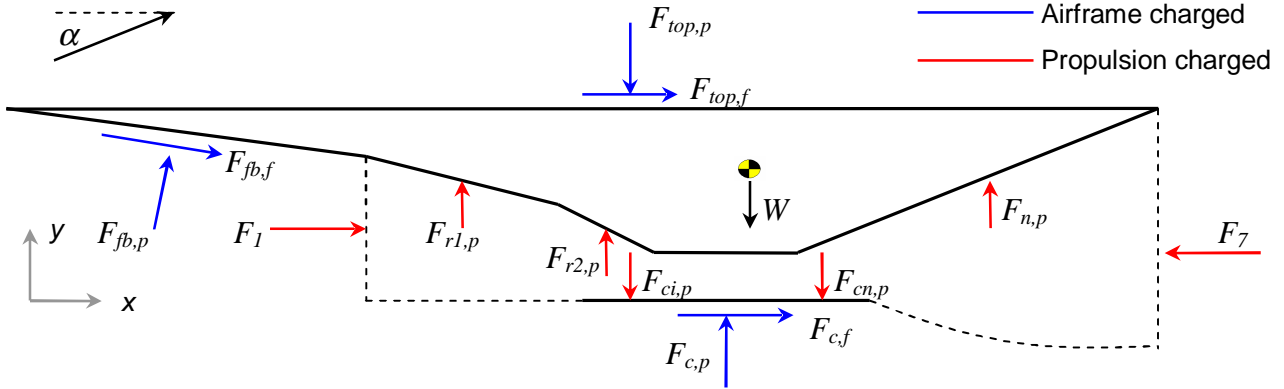


Figure 3.24. Resolved force accounting.

The three types of forces mentioned previously are pressure, frictional, and streamthrust, the relationships for which are given, respectively, by

$$F_{i,p} = P_i A_i, \quad (3.100)$$

$$F_{i,\tau} = \frac{1}{2} \rho V_i^2 C_f A_i, \quad (3.101)$$

and

$$F_{i,st} = \rho V_i^2 A_i + P_i A_i \quad (3.102)$$

The friction coefficient is assumed to be 0.001 for all surfaces, and the subscript  $i$  indicates the location of the action [46]. For a one-dimensional approach, the surface area in equations (3.100) and (3.101) reduces to the length of the vehicle, while the area in equation (3.102) reduces to the height of the cross section. With all of the properties known from the solution of each of the propulsion components, a force balance can be performed on the overall system. These equations are presented below, i.e.

$$L_{veh} = \left( \sum F_{p_y} + \sum F_{f_y} \right) \cos \alpha - \left( \sum F_{p_x} + \sum F_{f_x} \right) \sin \alpha, \quad (3.103)$$

$$D_{veh} = \left( \sum F_{p_y} + \sum F_{f_y} \right) \sin \alpha + \left( \sum F_{p_x} + \sum F_{f_x} \right) \cos \alpha, \quad (3.104)$$

and

$$T_{veh} = (F_7 - F_1)\cos\alpha . \quad (3.105)$$

Thus, for a given mission segment, all of the forces acting on the vehicle are known. To maintain level flight, however, the moments about the vehicle center of gravity must be considered as well. The general relationship between the vehicle forces and its moment is expressed as

$$M_{veh} = \sum F_i d_i \quad (3.106)$$

In the above equation,  $d_i$  represents the distance between the line of action of the force and the vehicle's center of gravity. For example, the forebody moment due to the pressure force, acting at the center of the forebody length  $(x_{fb}, y_{fb})$ , is given by

$$M_{fb_p} = F_{fb_{p_x}}(y_{fb} - y_{cg}) + F_{fb_{p_y}}(x_{cg} - x_{fb}). \quad (3.107)$$

As a result, the calculation of the vehicle's center of mass is essential.

In this study, the empty weight of the vehicle is fixed while the volume is dependent on the optimization process. Essentially, the design/decision variables dictate the geometry of the vehicle, and whatever the volume of that geometry is compared to a baseline value results in a proportional weight density. Additional weight is dependent on the amount of fuel necessary to accomplish all mission segments and is discussed in the following chapter. The vehicle volume is specifically calculated by integrating the individual line segments of the vehicle geometry, using equation (3.108), and adding and subtracting necessary values, as illustrated in figure 3.26.

$$\forall_{veh} = \int_{x_1}^{x_2} f_{12}(x)dx - \int_{x_1}^{x_3} f_{13}(x)dx - \int_{x_3}^{x_4} f_{34}(x)dx - \int_{x_4}^{x_5} f_{45}(x)dx - \int_{x_6}^{x_2} f_{62}(x)dx, \quad (3.108)$$

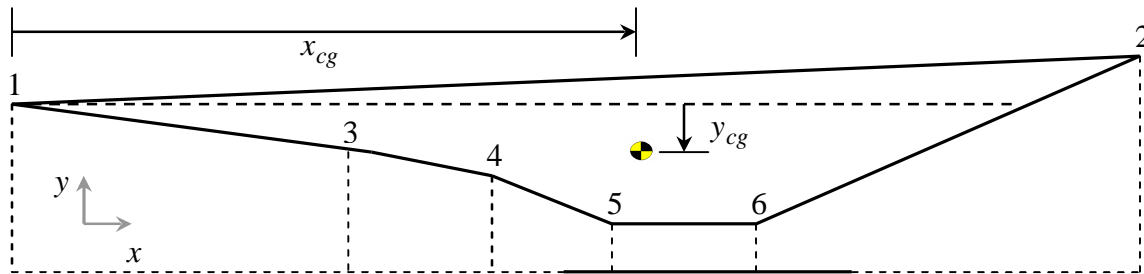


**Figure 3.25.** Illustration of integration technique [9].

The centroid of the vehicle, corresponding to the center of gravity because a uniform constant density is assumed, is determined by the *method of composite areas* [9]. The body is broken into five

simple shapes, either rectangles or triangles, whose centroids are easily calculated and the sum of which approximately comprise the vehicle. This is illustrated in figure 3.26.

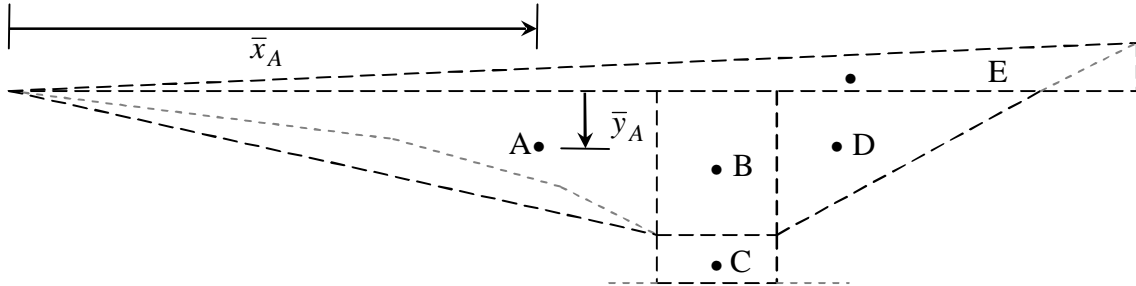


**Figure 3.26.** The five composite areas of the vehicle [9].

The coordinates of the individual centers of gravity are denoted by  $(\bar{x}_i, \bar{y}_i)$ , and the resulting overall center of gravity for the  $x$  and  $y$ -directions are given by

$$x_{cg} = \frac{\sum A_i \bar{x}_i}{A_i} \quad (3.109)$$

and

$$y_{cg} = \frac{\sum A_i \bar{y}_i}{A_i} \quad (3.110)$$

Thus, the vehicle volume's volume and center of gravity are known.

### 3.5.3 Lift and Trim

After the vehicle forces and moments are resolved, there is often a need to supplement the lift of the vehicle as well as trim the moment about the center of gravity. Consequently, a wing, assumed positioned at the center of gravity, and an elevon, positioned at the rear of the vehicle, are utilized to perform these tasks. These are illustrated in figure 3.27a.

To correctly model the amount of lift available from a reference area,  $S$ , the lift and drag coefficients must be known (see equations (3.97) and (3.98)). Consequently, a diamond airfoil shaped simple delta wing was chosen to meet the vehicle lift and trim requirements. The geometry is detailed in figure 3.27b. Using two-dimensional shock-expansion theory on the assumed inviscid geometry, the values of pressure at each surface are known for any angle of attack, given a thickness to chord ratio,  $t/c$ . For this analysis, a fixed thickness to chord ratio of five percent is assumed, while the maximum thickness occurs at half of the total chord length of the airfoil.

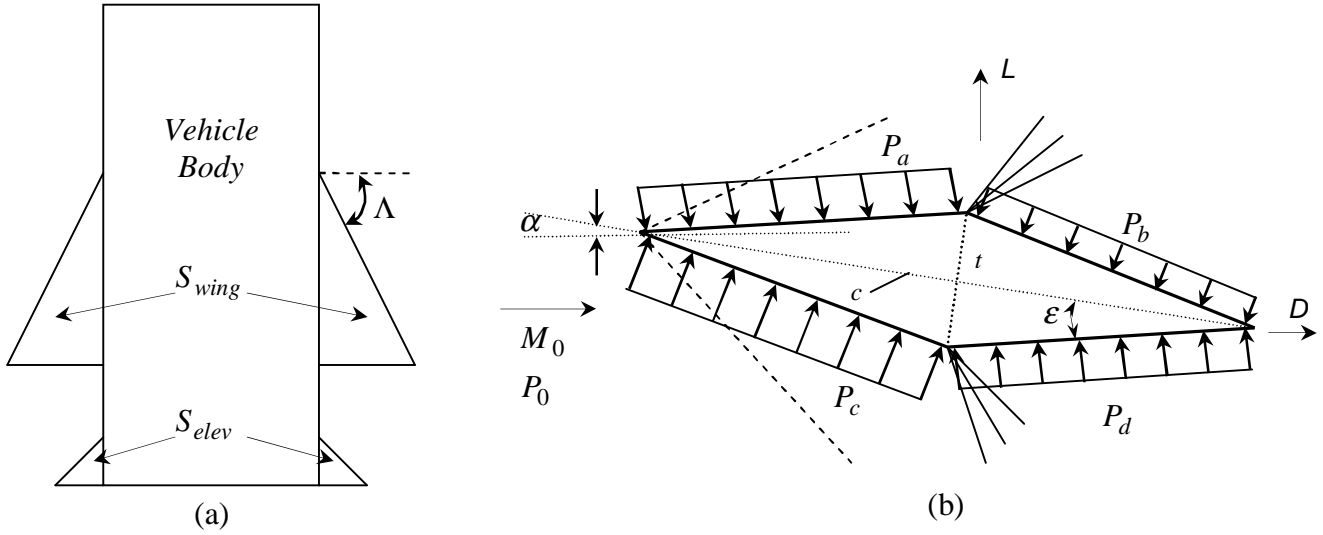


**Figure 3.27.** (a) Vehicle plan area and (b) elevon and wing cross-section detail [9].

As illustrated in the figure, at positive angles of attack the lower surfaces are subjected to higher pressures than the upper surfaces, resulting in lift. As would be expected, at zero angle of attack there is no lifting force, since the pressures on the top and bottom surfaces are equal. In addition, the drag results from the pressures on the front two surfaces necessarily being larger than on the back two, since the pressure on the back two surfaces is always the result of an expansion process. Thus, the lift and drag coefficients per unit span can be calculated by, respectively,

$$C_L = \frac{2l}{\gamma M_0^2 c} \left( \frac{P_c - P_b}{P_0} \cos(\alpha + \varepsilon) + \frac{P_d - P_a}{P_0} \cos(\alpha - \varepsilon) \right) \quad (3.111)$$

and

$$C_D = \frac{2l}{\gamma M_0^2 c} \left( \frac{P_c - P_b}{P_0} \sin(\alpha + \varepsilon) + \frac{P_d - P_a}{P_0} \sin(\alpha - \varepsilon) \right). \quad (3.112)$$

The chord length  $c$ , is determined by the law of cosines, where  $\varepsilon$  is in radians, and is written as

$$c = \sqrt{2}l(1 - \cos(\pi - 2\varepsilon))^{1/2}. \quad (3.113)$$

In this last equation,  $l$  is the length or one-dimensional area equivalent of each surface. The above relationships are contingent on the condition that  $\alpha > \varepsilon$ . In other cases, appropriate sign changes must be made. A detailed examination of this procedure is described by Anderson [53]. Consequently, the lift to drag ratio for the angles of attack and Mach numbers encountered in this study are plotted in

figure 3.28. In actuality, the Mach numbers encountered by the wing would be less than freestream conditions due to the assumed blunt leading edge bow shock that occurs from the vehicle having some finite width. However, since a detached shock calculation is much more involved and only the one-dimensional aspects are of concern in this study, it is assumed that the Mach numbers encountered by the wing and elevon are equal to the freestream. Bow shock concerns are addressed by the constraints.

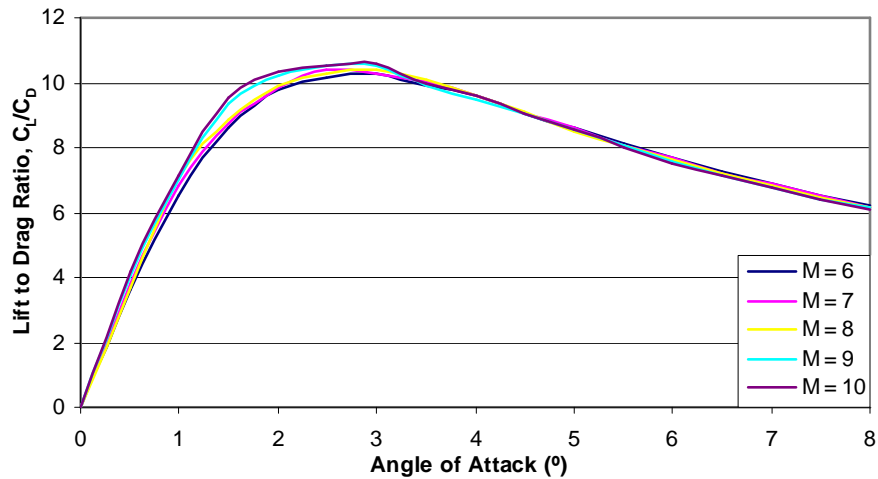


**Figure 3.28.** Lift to Drag ratio for the diamond airfoil at Mach numbers and angles of attack of interest.

The wing is assumed fixed on the vehicle at zero angle of attack with respect to the vehicle centerline. Thus, a positive flight angle of attack is necessary to generate lift from the wings. As various amounts of lift are required from the wings during different mission segments, and since the airframe itself without wings is capable of generating lift, the wing area is allowed to vary from mission segment to segment. In addition, the center of pressure of the wing is assumed to act through the center of gravity of the vehicle to induce no moment.

The elevon must provide a moment equal and opposite to the vehicle moment,  $M_{veh}$ , found in equation (3.106); otherwise, the vehicle may pitch uncontrollably about its center of gravity. Since this is obviously an undesirable situation, an elevon is introduced to cancel the pitching moment of the vehicle. This is accomplished by assigning an area to the elevon, fixing its axial location, and inclining or declining it until the force necessary to cancel the moment is found. The area is determined from the following relationship given by Bowcutt [25]:

$$S_{elev} = \frac{V_{elev} L_{veh}}{\left(1 - \frac{x_{cg}}{L_{veh}}\right)} \quad (3.114)$$

The elevon volume,  $V_{elev}$ , is assumed to be 0.04 [25]. The axial location of the elevon is one meter from the aft end of the vehicle, at a height equal to that of the nozzle free expansion surface. Thus, allowing the angle of incidence of the elevon,  $\omega$ , to vary, both upward and downward forces can be generated to cancel the vehicle moment and ensure stable flight.

### 3.5.4 Vehicle Mass Estimations

As previously mentioned, the estimated empty vehicle mass is based on several prospective hypersonic vehicles discussed by Curran and Murthy [5]. The empty mass of the vehicle is selected to be 5000 kg based on an estimate vehicle volume of 25 m<sup>3</sup> (with unit width). The takeoff<sup>26</sup> weight of the vehicle is assumed to be the sum of the empty mass and the fuel mass multiplied by the gravitational constant. So to estimate the takeoff vehicle mass, the fuel consumption over the mission must be estimated. The fuel mass fraction for each mission segment, a fraction of overall vehicle mass, is estimated by

$$\pi_f = \frac{m_{initial} - m_{final}}{m_{initial}} = 1 - \frac{m_{final}}{m_{initial}} \quad (3.115)$$

where  $m_{initial}$  and  $m_{final}$  are the masses of fuel at the initially and finally for each mission segment. Of course, how the mass changes from the beginning to the end of the mission varies depending on the type of constraints imposed in each mission segment, i.e. cruise, acceleration, etc. Estimating the takeoff fuel mass is accomplished by examining each mission segment and relating the sum of the fuel mass fractions of each mission segment to the empty mass by

$$m_{takeoff} = \frac{m_{empty}}{\left(1 - \sum \pi_f\right)} \quad (3.116)$$

Thus, an initial mass can be estimated. More specifics about the calculation of the mass fractions due to each of the vehicle constraints is discussed in the following chapter.

---

<sup>26</sup>“Takeoff” weight refers to the vehicle’s maximum weight (i.e. before any fuel begins to burn during the first mission segment) when the hypersonic vehicle is launched at Mach 6 (see Section 4.1). This varies from the traditional use of the term where the first mission segment is when an aircraft literally takes off from a runway.

### 3.5.5 Airframe Solution Procedure

Much like the inlet, the sequence of the airframe sub-system calculations can be made much clearer through the outline of a step-by-step procedure for solving the forces and moments of the vehicle. This process is as follows:

1. The forces on the vehicle, excluding those due to the wing and elevon, are found via equations (3.100) through (3.102) and knowledge of the flow properties through each component. The streamthrust exiting the vehicle is based on the initial assumption that the equivalence ratio in the combustor is  $\phi = 0.8$ .
2. Resolving these forces into  $x$  and  $y$ -components and calculating the overall vehicle moment from equation (3.106), the force needed from the elevon is known.
3. Depending on whether a clockwise or counterclockwise moment is required, the elevon is inclined or declined from a reference position originally aligned with the vehicle axial centerline until zero pitch is achieved.
4. The forces are now resolved into lift and drag coordinates aligned with the vehicle's direction of velocity.
5. The area of the wing, if any, necessary to provide level flight is calculated from the lift and drag coefficients of the diamond airfoil at the vehicle angle of attack. For cruise, the total lift must equal the weight of the vehicle. Thus,

$$L_{wing} = L_{total} - L_{veh} - L_{elev} \quad (3.118)$$

6. With the lift and drag of every component (now including the elevon and wing) known, and level and stable flight ensured, the thrust supplied from equation (3.105) is compared to the total drag of the vehicle,

$$D_{total} = D_{veh} + D_{wing} + D_{elev} \quad (3.119)$$

For a cruise condition, the thrust must equal the drag,  $T_{veh} = D_{total}$ .

7. Since rarely does the thrust meet the required value, the equivalence ratio is iteratively increased or decreased based on the requirement of the mission segment. This process is known as "throttling." Adjusting the amount of fuel delivered to the combustor necessarily changes the flow properties and, subsequently, the forces in both the combustor and nozzle. Consequently,

the solution procedures for these two components must be repeated for each equivalence ratio and, since the forces are changing, so must the lift, drag, wing, and elevon calculations.

All of this can be accomplished within a reasonable set of constraints guaranteeing that flight is possible. As a result, the variables for the airframe sub-system can be identified.

**Table 3.9.** Airframe decision (independent) and dependent sub-system variables.

Variable	Classification	Symbol	Imposed Limits
Angle of Attack [°]	Independent, operational	$\alpha$	$0.1 \leq \theta_{fb} \leq 6$
Wing planform area [m <sup>2</sup> ]	Dependent, operational	$S_{wing}$	$0 \leq S_{wing} \leq 0.10 S_{veh}$
Elevon deflection angle [°]	Dependent, operational	$\omega$	$0 \leq \omega \leq \omega_{max}$
Off-design forebody energy addition [kW] (see figure 3.11)	Dependent, operational	$\dot{Q}_{fb}^{\leftrightarrow}$	Shock-on-lip
Off-design ramp 1 energy addition [kW] (see figure 3.11)	Dependent, operational	$\dot{Q}_{r1}^{\leftrightarrow}$	Shock-on-lip

Each of the variables in table 3.9 depends on the angle of attack. It should be noted, however, that all of the analyses presented previously are for a single angle of attack, which may or may not result in a “best” vehicle configuration. Therefore, both the propulsion and airframe sub-systems must be iteratively solved through a range of angles of attack to ensure that a “best” configuration emerges. How this “best” configuration is defined, as well as the propulsive and aerodynamic requirements of thrust and lift for acceleration, climb, and turn mission segments are discussed in the next chapter.

### 3.5.6 Aerodynamic Loss Mechanisms

For an exergy approach to vehicle design to be complete, the entropy generated due to irreversibilities generated by the airframe sub-system must be determined. The three primary causes of entropy generation in the airframe are due to friction, shocks, and energy addition across a finite temperature difference to maintain a shock-on-lip operating condition. Again, the entropy generation due to shocks is given by equation (3.22). The shocks produced in the airframe sub-system are the forebody, external cowl, top surface, and tail oblique shocks. The entropy generation rate due to the energy addition is found from equation (3.44), while that due to friction for a given surface is

$$\dot{\mathcal{S}}_{irr_{fric}} = \frac{F_f V}{T}, \quad (3.120)$$

where  $F_f$  is the local frictional force,  $V$  is the local flow velocity, and  $T$  is the local flow temperature [54]. The local frictional force is defined as

$$F_f = c_f q_0 A_s \quad (3.121)$$

and is a function of friction coefficient (again assumed to be 0.001 for all surfaces), the local flow dynamic pressure,  $q_0$ , and the local surface area,  $A_s$ . For a unit width vehicle, the surface area reduces to its length. The overall entropy generation rate for the airframe sub-system can now be expressed as

$$\dot{\mathcal{S}}_{irr_{aero}} = \sum \dot{\mathcal{S}}_{irr_{fric}} + \sum \dot{\mathcal{S}}_{irr_{shocks}} + \sum \dot{\mathcal{S}}_{irr_{nrg}} \quad (3.122)$$

No penalty is associated with morphing the wing and pitching the elevon, as it is assumed that the related irreversibilities are small compared to the friction and shock contributions of the rest of the airframe.

### 3.5.7 Airframe Sub-system Constraints

To ensure a viable airframe sub-system design, numerous constraints must be met. From the discussion of Prandtl-Meyer expansions, maximum inclination angles are placed upon the elevon to prevent flow separation. For Mach 6, the maximum angle is 34 degrees while at Mach 10 the maximum expansion angle drops to 22 degrees. These restrictions, however, must be more stringent not only to ensure that the flow is smooth but also to help deter long convergence times during the computational process. During preliminary evaluations it was shown that these limits far exceed the necessary operational range.

The only fixed parameter in this study is the vehicle length,  $L_{veh}$ . Its value is 24m, selected based on a survey of vehicles surveyed in Curran and Murthy [5]. The reference area of the vehicle,  $S_{veh}$ , is estimated based on the assumption that a vehicle of 24m in length would be 4m wide, resulting in a reference area of 96m<sup>2</sup>. Consequently, a relatively small variable wing area can be defined as 10 percent of the vehicle reference area, or 9.6 m<sup>2</sup>.

Other constraints include a minimum sweep angle  $\Lambda$  (see figure 3.27) which is set to 60 degrees. As a result, the model ensures that the position of the wings at maximum area do not fall outside of the

*Mach cone*, which is the distance at which a wing would encounter multiple Mach numbers due to the blunt leading edge bow shock [2]. Furthermore, the lower limit placed on the angle of attack, 0.1 degrees, guarantees that a forebody expansion, as opposed to the desired oblique shock, cannot occur. Consequently, this constraint can limit the ability of the vehicle to develop a downward force with the wings, since the wings are fixed on the vehicle aligned with the vehicle centerline.

# Chapter 4

## Mission-Level Synthesis/Design Challenge

As stated in the thesis objectives, the primary goal of this research is to examine the usefulness of an exergy approach to the synthesis/design of a hypersonic vehicle. When a vehicle is evaluated over the course of various sets of constraints, or mission segments, the ideal synthesis/design will be a compromise able to meet all mission segment operational requirements while yielding a “best” performance measure. Consequently, this chapter is dedicated to detailing the segments which comprise the mission and introducing the methods and criteria for performance assessment.

### 4.1 Mission Overview

An overall vehicle mission must be defined to facilitate the analysis in this study. Consequently, a scramjet vehicle mission was chosen based on the following two primary factors: the mission’s potential as a future military application and the ability of the highly integrated vehicle to operate over the range selected. Keeping these aspects in mind, the following mission illustrated in figure 4.1 was developed with the assistance of Moorhouse [55].

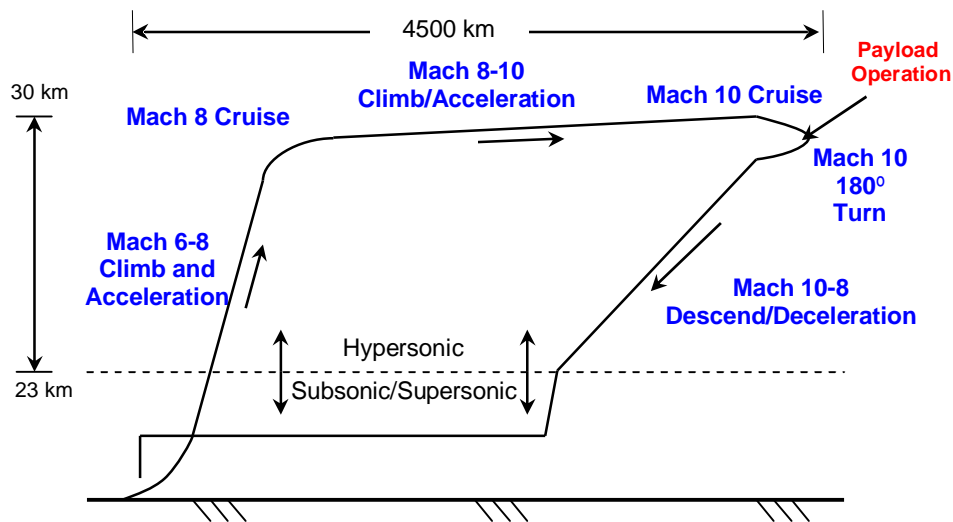


Figure 4.1. Total scramjet vehicle mission.

The total mission consists of six segments, shown in blue, with a payload operation assumed to occur during the fifth mission segment. As illustrated, the scramjet operation begins at Mach 6. This necessarily assumes an initial stage (or stages) of propulsion (e.g., turbojet or ramjet) not specifically addressed in this study. During each segment, the mass of the vehicle is considered constant. In essence, the thrust requirements are based on the initial mass at the beginning of each segment, and that thrust is sustained throughout the duration of the segment. In actuality, of course, the mass of the vehicle is constantly changing due to the consumption of the fuel, and consequently the vehicle performance requirements change as well. The consequences of such an assumption are addressed in the results presented in Chapter 5. The constraints for these segments as well as their general details are shown in table 4.1.

**Table 4.1.** Mission segment details.

Segment	Description
1	Accelerate and climb from Mach 6 (at 23.2km) to Mach 8 (at 26.9km), t = 90s
2	Mach 8 cruise for 600s
3	Accelerate and climb from Mach 8 (at 26.9km) to Mach 10 (at 30.0km), t = 90s
4	Mach 10 cruise for 600s
5	Perform a 180°, 2g sustained turn at Mach 10
6	Descend and decelerate to Mach 6

**Table 4.2.** Air and vehicle flight envelope data for a dynamic pressure of 85kPa.

Mach Number	6	7	8	9	10
Temperature [°K]	219.8	221.8	223.5	225.1	226.5
Pressure [Pa]	3378	2475	1901	1502	1204
Density [kg/m <sup>3</sup> ]	0.0533	0.0387	0.0295	0.0231	0.0184
Velocity [m/s]	1787	2094	2403	2712	3023
Altitude [km]	23.18	25.20	26.93	28.51	29.96

Since it is assumed that constant dynamic pressure is maintained, the properties of air at altitude and the necessary velocities associated with maintaining a constant dynamic pressure of 85kPa are specified in table 4.2. Depending on the desired performance criterion, the associated dependent ranges, times, fuel mass fractions, and changes in altitude and velocity must be established for each

mission segment. These can be associated with flight along a constant dynamic pressure as described by Markell [9]. How to find these details is discussed in the following sections.

#### 4.1.1 Climb/Acceleration and Descend/Deceleration

Table 4.1 shows that acceleration or deceleration is necessarily coupled with a change in altitude to maintain a constant dynamic pressure. To find the net thrust, or thrust minus drag, required for a specific mission segment, the following flight equation (energy balance) is used:

$$\{T - D\}V = W \frac{dh}{dt} + \frac{W}{g} \frac{d}{dt} \left( \frac{V^2}{2} \right). \quad (4.1)$$

Here, Newton's second law is applied to the vehicle illustrated in figure 4.2, from which a relationship can be realized in the form of potential and kinetic energies. In the above equation,  $h$  is the altitude,  $W$  is the weight, and  $g$  is the gravitational constant.

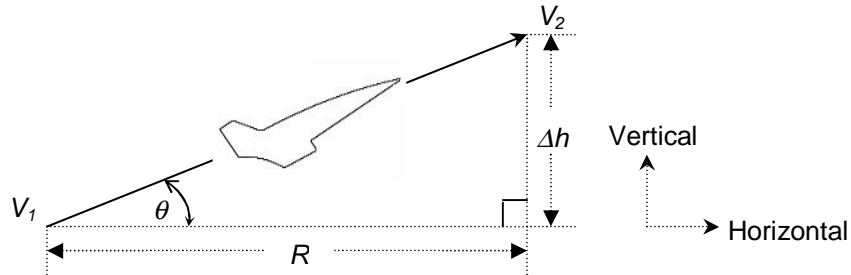


Figure 4.2. Acceleration detail.

Since the weight is assumed constant over each mission segment, approximations are made for the changes in altitude and velocity over the segment. As a result, the net thrust required to go from an initial to a final velocity can be written as

$$T - D = \frac{W_i}{\bar{V}_{21}} \left( \frac{h_2 - h_1}{t_{21}} \right) + \frac{W_i}{\bar{V}_{21} g} \left( \frac{V_2^2 - V_1^2}{2} \right), \quad (4.2)$$

where  $\bar{V}_{21}$  is the average velocity,  $t_{ms}$  is the total time required for the segment, and  $W_i$  is the initial weight at the beginning of the segment. With initial and final velocities and altitudes known via table 4.1, the range covered by the aircraft during the segment can be found using Pythagorean's theorem, with the length of the hypotenuse in figure 4.2 equal to  $\bar{V}_{21} t_{ms}$ , or via the tangent trigonometric function,  $\tan(\theta) = \Delta h/R$ . Thus, a time or inclination angle ( $\theta$ ) requirement can constrain the system. From

equation 4.2 and figure 4.2, one can reason that the larger the angle, the smaller the time and the greater the required net thrust. All accelerations in this mission are assumed to occur over a period of 90 seconds. Similarly, a deceleration can be accomplished with a negative inclination angle.

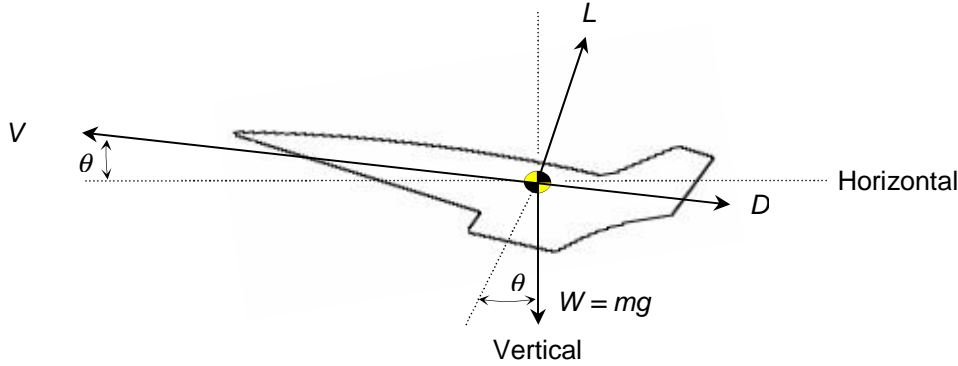


**Figure 4.3.** Forces acting on an aerospace vehicle during flight.

For an acceleration/climb mission segment, figure 3.19 can be represented as above, which shows that the total lift required by the vehicle, with wings if necessary, is dependent on the vehicle inclination angle according to equation 4.3. Again, the weight is assumed to be the weight at the beginning of the segment.

$$L_{total} = W_1 \cos(\theta) \tag{4.3}$$

An estimate of the mass fraction of fuel required is necessary for each mission segment to determine the total initial vehicle weight since it is not known how much fuel is burned in a segment until it is actually simulated. Essentially, an over-estimate is required which must account for the worst case vehicle design (the design that requires the most fuel to complete the mission segment). For a climb/acceleration segment, equation 4.4 is used [9]. In this equation, the final mass is related to the initial mass in terms of the velocity and altitude changes, lift and drag coefficients for the airframe, overall vehicle efficiency ( $\eta_o$ ), and lower heating value of the fuel ( $h_{pr}$ ), i.e.

$$\frac{m_2}{m_1} = \exp \left( - \frac{\left( \frac{V_2^2}{2} - \frac{V_1^2}{2} \right) + g \left( \frac{C_D}{C_L} R + (h_2 - h_1) \right)}{\eta_o h_{pr}} \right) \tag{4.4}$$

The overall vehicle efficiency is defined as

$$\eta_o = \frac{T_{veh} V_0}{\dot{m}_f h_{pr}}, \quad (4.5)$$

where  $T_{veh}$  is the thrust,  $V_0$  is the flight velocity, and  $\dot{m}_f$  is an estimate of the mass flow rate of fuel. Since these values are not known until the mission is flown, an estimate of the overall efficiency must be assumed as well.

For a typical descend/deceleration segment, it is assumed that the engine can be throttled back to recover the potential energy invested in the climb segments, and no fuel is assumed burned [40]. However, in this study, a long deceleration is suggested, and values derived from initial tests of the vehicle are used to help estimate the fuel mass fraction of the segment. The requirements characteristic of each mission segment are discussed in Section 4.1.4.

#### 4.1.2 Constant Altitude/Speed Cruise

As previously discussed, a cruise mission is defined as one which maintains level flight and constant velocity. Consequently, for small angles of attack, equation (4.2) reduces simply to

$$T_{veh} = D_{veh}. \quad (4.6)$$

In addition, inspection of figure 4.3 with no inclination angle yields the total vehicle lift for a cruise segment must be

$$L_{total} = W_1. \quad (4.7)$$

With no changes in velocity and altitude, equation (4.4) for the fuel mass fraction can also be simplified as

$$\frac{m_2}{m_1} = \exp\left(-\frac{gR}{\eta_o h_{pr} \frac{C_L}{C_D}}\right). \quad (4.8)$$

Again, the vehicle lift and drag coefficients and overall efficiency must be estimated for the cruise segment.

#### 4.1.3 Constant Altitude/Speed Turn

A constant altitude, constant velocity turn is accomplished by banking by an angle,  $\nu$ . The bank angle is related to a load factor,  $n$ , by the relationship

$$\cos(\nu) = \frac{1}{n}. \quad (4.9)$$

The load factor represents what multiple of the vehicle weight the total vehicle lift must provide in order to accomplish the turn. This is illustrated in figure 4.4. Knowing the load factor, the radius of curvature,  $R_c$ , can be determined using Pythagorean's theorem, i.e.

$$R_c = \frac{V^2}{g\sqrt{n^2 - 1}} \quad (4.10)$$

Alternatively, if a specific radius of curvature is desired, a load factor may be determined. The range traveled by the vehicle during the turn - the arc length - is calculated from  $R = R_c\psi$ , where  $\psi$  is the angle through which the turn is made. For cruise, the load factor is one, and equation (4.7) results. In this study, a load factor of two is desired for a 180 degree turn.

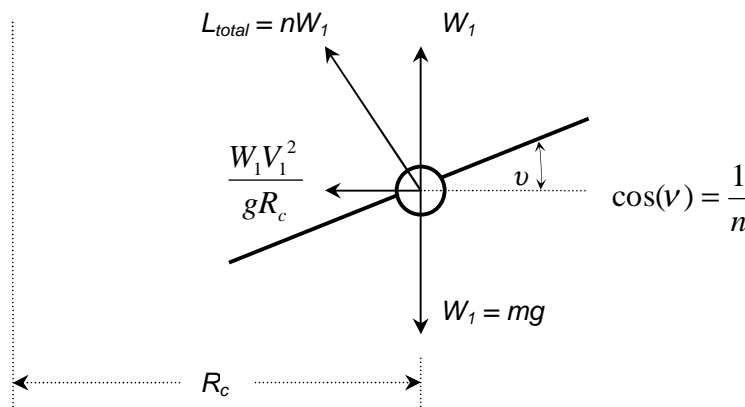


**Figure 4.4.** Force balance during a turn (tail view).

As illustrated, the required total lift for a turn is necessarily greater, implying also that the drag is greater than that for cruise and, thus, the thrust must be greater as well. Since no altitude or speed changes are occurring, both cruise equations for (4.6) and (4.8) for vehicle thrust and mass fuel fraction, respectively, still apply.

#### 4.1.4 Total Mission

Now that constraining flight characteristics (table 4.1) and general relationships (equations (4.1) through (4.10)) for the types of mission segments encountered in this study have been established, the details of each can be discussed. The specific values for the six mission segments in this study are described in table 4.3. These values are based on time and constant dynamic pressure constraints .

**Table 4.3.** Mission segment characteristics and constraining conditions.

No.	Mission Segment	$t_{ms}$ [s]	$T_{veh}-D_{veh}$ [kN]	$\theta$ [°]	$R$ [km]	$\Delta h$ [km]	$\Delta V$ [m/s]	$\pi_f^{27}$	$n$
0	Mach 6-8 Acceleration	90	43.47	1.14	189	3.75	616	0.0521	1
1	Mach 8 Cruise	600	0	0	1442	0	0	0.0651	1
2	Mach 8-10 Acceleration	90	36.73	0.71	244	3.03	620	0.0508	1
3	Mach 10 Cruise	600	0	0	1814	0	0	0.0812	1
4	Mach 10 Turn	559	0	0	1690	0	0	0.0759	2
5	Mach 10-8 Deceleration	533	-6.075	-0.12	1447	-3.03	-620	0.0300*	1
	<b>TOTALS</b>	<b>2472</b>	<b>-</b>	<b>-</b>	<b>6826</b>	<b>-</b>	<b>-</b>	<b>0.3551</b>	<b>-</b>

\*Based on program experimentation.

As illustrated, the total mission covers nearly 7000 km in roughly 41 minutes. How suitable these initial guesses for fuel mass fraction are will be discussed in the results. With the total mass fraction listed above and equation (3.116), the total takeoff mass of the vehicle is found to be 14080 kg. It can be seen that though the inclination angles for acceleration and deceleration mission segments are very small, the speed of the vehicle at each segment's respective Mach number allows for the completion of the segment requirements within the desired time frame. This implies that vehicle control in actual flight, i.e. maintaining a constant dynamic pressure, will indeed be challenging. With conventional aircraft, decelerations can be accomplished with negligible fuel use; however, the hypersonic vehicle must necessarily be constrained, for the geometry selected in this study, to allow only angles of attack greater than the forebody angle. If this constraint is ignored, undesirable expansions can occur in the inlet. Thus, a fuel mass fraction of 0.03 for the deceleration segment is selected based on preliminary runs of the program. The long range required for the turn is a consequence of selecting a small  $n$  value. As the vehicle is extremely sensitive to changes in flight conditions, a value of two was selected.

## 4.2 Program Optimization

Finding a useful and timely result rests on the selection of a suitable optimization routine and the criteria which it uses to determine the best ("optimal") vehicle synthesis/design. Thus, a background on optimization and the specific algorithm and performance measures employed are discussed next.

<sup>27</sup> The fuel mass fraction shown is what is (estimated to be) required for each individual segment. The estimated thrust value for each segment is based on the assumption that the vehicle carries all necessary fuel for the completion of the mission.

### 4.2.1 Optimization Background

The independent (decision) variables selected for this study are summarized in Section 4.3. These variables are varied within specified limits to find a “best” or “optimal” hypersonic vehicle configuration through the following procedure. The independent variables, hereby represented by a vector  $\overset{1}{x}$ , are used to create two systems of equations to represent the model of the system, i.e.

$$\overset{V}{H} = \begin{Bmatrix} \overset{V}{h}_1(\overset{V}{x}) \\ \overset{V}{h}_2(\overset{V}{x}) \\ \overset{V}{h}_3(\overset{V}{x}) \\ \mathbb{M} \\ \overset{V}{h}_n(\overset{V}{x}) \end{Bmatrix} = 0 \text{ and } \overset{V}{G} = \begin{Bmatrix} \overset{V}{g}_1(\overset{V}{x}) \\ \overset{V}{g}_2(\overset{V}{x}) \\ \overset{V}{g}_3(\overset{V}{x}) \\ \mathbb{M} \\ \overset{V}{g}_n(\overset{V}{x}) \end{Bmatrix} \leq 0 \quad (4.11a,b)$$

The vector of equality constraints  $\overset{V}{H}$  is composed of sub-vectors  $\overset{V}{h}_i$  each of which mathematically describes a phenomenon or set of phenomena, e.g., those in the inlet or combustor, usually within the realm of a particular discipline. The vector of inequality constraints  $\overset{1}{G}$  represents natural or artificial limitations imposed upon the system.

With engineering system and sub-system models defined, optimization subject to a desired set of constraints can now be performed. The system and sub-system models describe the set of nonlinear constraints implemented in the formulation of the optimization problem. The optimization problem is generally expressed as

$$\text{Minimize } f(\overset{V}{x}) \quad (4.12)$$

with respect to  $\overset{V}{x}$  and subject to the following equality and inequality constraints:

$$\overset{V}{H}(\overset{V}{x}) = 0 \quad (4.13)$$

and

$$\overset{V}{G}(\overset{V}{x}) \leq 0 \quad (4.14)$$

All equality constraints are active by definition whereas an inequality constraint  $g_j \leq 0$  is only active if  $g_j = 0$ . The function  $f(\overset{1}{x})$  is called the objective function.

### 4.2.2 Objective Functions

Three objective functions will be analyzed in this study. For the constraints imposed by the mission segments, the most desirable vehicle of fixed initial weight is the one which can accomplish the

entire mission using the least amount of fuel, in which case, the fuel is being used most efficiently (this is the minimum energy required).

The first objective function is a first law-based efficiency, as discussed in Chapter 2, is a typical evaluation criterion for vehicle synthesis/design. It is defined as a weighted average of the thrust efficiency<sup>28</sup> over the entire mission, or

$$\eta = \frac{\sum_{i=0}^5 \dot{m}_{f_i} t_i \eta_i}{\sum_{i=0}^5 \dot{m}_{f_i} t_i} \quad (4.15)$$

where again the mission segment thrust efficiency is as described in equation (4.5), or

$$\eta_i = \frac{T_i V_i}{\dot{m}_{f_i} h_{pr}} \quad (4.5)$$

where  $i$  indicates a value for a specific mission segment. This quantity is maximized (in actuality, its inverse is minimized), and at each mission segment, the velocity and heating value are fixed, in which case it is possible to see that increasing thrust and decreasing fuel mass flow rate tradeoff until an optimized value is reached.

The second objective function is fuel weight. Assuming fuel burn is the only impact to vehicle weight, the consumption, which is minimized in this case, can be defined as

$$W_{fuel} = g \sum_{i=0}^5 \dot{m}_{f_i} t_i \quad (4.16)$$

Here the mass flow rates of fuel for each of the segments are multiplied by the time of each segment and the gravitational constant ( $g$ ), and summed.

The third and final objective function is exergy based, and from the descriptions in Chapter 3, it is defined as

$$Ex_{Des} + Ex_{loss} = \sum_{i=0}^5 (T_{0,i} \dot{S}_{irr,total,i} + \dot{E}x_{fuel\ loss,i}) t_i \quad (4.17)$$

where

---

<sup>28</sup> The thrust efficiency is also referred to in the literature as the overall efficiency or the product of the thermal and propulsive efficiencies, i.e.  $\eta_o = \eta_{th} \eta_p$  where  $\eta_{th} = \frac{\dot{K}E}{\dot{m}_f h_{pr}}$ ,  $\eta_p = \frac{TV}{\dot{K}E}$  and  $\dot{K}E$  is the rate of kinetic energy added to the engine.

$$\dot{\mathcal{S}}_{irr,total} = \dot{\mathcal{S}}_{irr,inlet} + \dot{\mathcal{S}}_{irr,comb} + \dot{\mathcal{S}}_{irr,nozz} + \dot{\mathcal{S}}_{irr,aero} . \quad (4.18)$$

This objective function, which is minimized, includes all the losses associated with vehicle flight previously discussed as well as the exergy of the unmixed fuel mass (if any) that exits the combustor. Again, the advantage of an exergy approach specifically is that it can provide detailed information about tradeoffs being made among the vehicle components.

### 4.2.3 MooLENI Evolutionary Algorithm

Two popular optimization techniques typically applied to highly nonlinear problems, such as energy management in a hypersonic vehicle, are gradient-based and evolutionary algorithms. Gradient-based methods may prove to be unsatisfactory partly because energy system problems very typically involve a mix of discrete and continuous variables which make the space of optimal solutions discontinuous. Furthermore, for highly non-linear spaces with a large number of decision variables (degrees of freedom), gradient-based methods often get stuck in local optima. As a result, well conditioned evolutionary algorithms, capable of searching an entire synthesis/design space, tend to be more practical, particularly for energy system problems [56]. This is the optimization tool chosen for this study.

The evolutionary algorithm starts with a randomly generated initial population of possible solutions (within the specified limits of the problem). This population undergoes a series of operations in which, depending on how the individuals in the population fare with respect to the objective function, create a new population by means of mutation (slight changes in individuals from one generation to the next), crossover (creating individuals of the next generation, or children, with characteristics similar to two successful individuals, or parents, of the first generation), and selection (retaining “good” members of the population and discarding the “bad”). Evolutionary algorithms typically employ some sort of mechanism to preserve “diversity,” which helps ensure that the solution does not quickly arrive at a local optimum. Disadvantages of the evolutionary algorithm include that it can be very computationally expensive, i.e. requiring long convergence times to survey a solution space, and, due to the random nature of the process, often require multiple runs to give some assurance that a global optimum is found. However, the need for multiple optimization runs is not exclusive to randomly based algorithms such as evolutionary algorithms. Due to the difficulty and impracticality of establishing the sufficient and necessary conditions (i.e. the Karuch-Kuhn-Tucker conditions [57]) for a global optimum in these types of problems, even gradient-based algorithms require multiple runs with significantly varied initial

conditions (vectors) to establish with some degree of assurance that the optimum found is a global one or at the very least the “best” among a set of local ones. Ideally, it is the use of hybrid algorithms which use, for example, an evolutionary algorithm followed by a gradient-based algorithm which may produce the best results. Such an approach, however, was not possible here due to the software constraints under which this research work was labored.

The specific evolutionary algorithm selected for this study is the Queuing Multi-Objective Optimizer (QMOO), also known as MooLENI, designed by Leyland and Molyneaux at the Laboratoire d’Energetique Industrielle (Laboratory of Industrial Energy Systems, LENI) at the Ecole Polytechnique Federale de Lausanne (EPFL) [56]. This software was developed specifically for the challenges encountered in optimizing complex energy systems. QMOO creates groups of solutions which evolve quasi-independently insuring that diversity is maintained, while also aggressively preserving only the best solutions. In addition, clustering is utilized to identify and surpass local optima. Consequently, QMOO has proven a valuable tool for energy systems optimization in many applications [56].

### 4.2.3 Hypersonic Vehicle Model and Optimization Integration

The optimization process begins by QMOO randomly selecting an initial set of independent variables as summarized in table 4.4. Values for these variables are fed to the hypersonic vehicle program, upon successful completion of which, a reasonable objective function value is generated. For configurations in which the constraints of the vehicle program are not met, a severely penalized objective function is delivered to the optimizer in order to promote the choice of a better solution.

**Table 4.4.** Mission design and operational decision variables for the inlet, nozzle, combustor, and airframe.

	Variable	Classification	Symbol	Imposed Limits
Inlet	Forebody position [m]	Design, decision	$X_{fb}$	$0.35L_{veh} \leq X_{fb} \leq 0.65L_{veh}$
	Cowl position [m]	Design, decision	$X_{cowl}$	$0.45L_{veh} \leq X_{cowl} \leq 0.77L_{veh}$
	Ramp 1 position [m]	Design, decision	$X_{ramp1}$	$0.02L_{veh} \leq X_{ramp1} \leq 0.33L_{veh}$
	Forebody angle [°]	Design, decision	$\theta_{fb}$	$1 \leq \theta_{fb} \leq 6$
Comb.	Combustor length [m]	Design, decision	$L_{comb}$	$0.02L_{veh} \leq L_{comb} \leq 0.33L_{veh}$
Noz.	Nozzle expansion angle [°]	Design, decision	$\theta_{nozz}$	$8 \leq \theta_{nozz} \leq 18$
	Percent nozzle length	Design, decision	$\%_{nozz}$	$0 \leq \%_{nozz} \leq 0.25$
AF	Angle of attack [°]	Operational, decision	$\alpha_0$	$0.1 \leq \alpha_0 \leq 6$

The optimizer deals only with independent variable values and the objective function values. After ten generations, the optimizer outputs a file containing the state of the current population, i.e. the objective function value and associated independent variable values. The optimization is manually aborted when the user identifies that convergence has occurred. The coupling of the hypersonic vehicle model described in Chapter 3 and QMOO is possible because both were implemented in MATLAB™. Several Machines, ranging in performance, were used independently throughout this study. These included six processors with speeds ranging from 1.5 to 3.05 GHz, RAMs from of 512 to 1000 MB, and hard drives 10 to 80 GB hard drives.

# Chapter 5

## Results

Several investigations were performed for the integrated hypersonic vehicle flying the mission described in Chapter 4. These include the impact of objective function choice on vehicle geometry and fuel mass fraction as well as a discussion on the optimization process and a discussion of its results. In addition, the integrated hypersonic vehicle model itself is explored and compared to other models in the literature. Furthermore, the impact of mission segment discretization is addressed as is the performance of the integrated vehicle compared to vehicles optimized for a single mission segment. Of course, the usefulness of an exergy approach for overall vehicle synthesis/design is also examined. However, the discussion in this chapter begins with that of model validation and exploration.

### 5.1 Integrated Hypersonic Vehicle Model Validation and Exploration

Though there is little information in the literature on hypersonic vehicle performance (there appears to be none for which a mission-level analysis is performed), this section compares the results of the vehicle model developed and implemented in this research work to others where possible. In addition, vehicle component characteristics and performance are explored

#### 5.1.1 Engine Sub-system

To test the performance characteristics of the combustor, the model was verified by Markell against data supplied by Riggins [31]. This is the same eleven meter vehicle model with isentropic inlet and nozzle discussed in figure 2.9 of Chapter 2. A perfect gas, one dimensional flow is subject to Rayleigh heating and a high coefficient of friction within the combustor where heat released from fuel is a function of distance such that a constant combustion efficiency results. Table 5.1 shows the data for both models at the inlet entrance (zero meters), combustor entrance (five meters), nozzle entrance (six meters), and engine exit (eleven meters). To achieve isentropic flow, the inlet and nozzle were simulated with the shocks, heat transfer, and friction “turned off.” As shown in table 5.1, the differences between models are slight.

**Table 5.1.** Combustor model comparison/validation .

x (m)	Riggins Model [31]				Thesis Model [9]			
	M	T (K)	P (N/m <sup>2</sup> )	u (m/s)	M	T (K)	P (N/m <sup>2</sup> )	u (m/s)
0	12.0	200	1000	3400	12.0	200	1000	3400
5.0	6.22	679	70900	3260	6.26	674	70400	3260
6.0	1.72	4350	647000	2280	1.73	4340	646000	2290
11.0	5.12	1110	5500	3420	5.11	1120	5540	3420

Comparisons were also made for combustor length as a percentage of total length. The results of this comparison include combustor lengths for the thesis model ranging from 2.1 to 4.4 percent of the vehicle length. Bowcutt's [25] optimal Mach 10 accelerator vehicle had a combustor length of 1.8 percent of the vehicle length, while Riggins [46] vehicle combustor length was estimated as 5 percent of the vehicle length. Starkey's two-dimensional model utilized combustor lengths of 7.1 to 8.2 percent of the vehicle length for Mach 8 and Mach 10 periodic trajectory cruises [28]. It should be noted that these comparisons should be viewed qualitatively, since each vehicle is designed for a different purpose, and each utilizes its own unique combustor model. As a brief note on the equivalence ratio, they were found to vary from 0.14 to 0.84 for the various vehicle designs in this comparative study. Though 0.14 seems quite small, Bowcutt optimized a Mach 15 cruise vehicle with an equivalence ratio as low as 0.0675 [25].

As discussed in Chapter 3, though methods are incorporated to include the effects of combustor and nozzle cooling and fuel preheating, this model is not thermally balanced. No method is included to maintain the temperature of the stored hydrogen entering the preheating stage, which for this preliminary study is an acceptable simplification. However, the need for making the model thermally balanced is demonstrated by comparing the mass flow rates of fuel into the engine and the mass flow rates of fuel needed to cool the engine. For example, given in table 5.2 are the two mass flow rates during each mission segment for the optimized minimum exergy destruction vehicle. As seen in this table, the latter mission segments require cooling mass flow rates of hydrogen greater than that actually entering the engine, implying that the additional portion of unused fuel must be recirculated. As discussed in Chapter 3, the fuel temperature is elevated from below vaporization temperature to 600 8K, indicating that if no cooling system is utilized, then at a minimum the effects of recirculation should be considered (for example, see the work by Rancruel and von Spakovsky [8]). Carrying enough extra fuel to create a reservoir can be measured against the additional mass and energy required to include a

cooling system. However, the fact that it is the latter mission segments that require the larger mass flow rates may not bode well for a reservoir type system. Perhaps this problem can be alleviated by allowing for a variable fuel injection temperature. Though the properties entering the combustor would now fluctuate, this may provide the necessary cooling or highly reduce the required fuel recirculation mass flow rate.

**Table 5.2.** Required and actual mass flow rates of H<sub>2</sub>.

Segment	$\dot{m}_{fuel}$ [kg/s]	$\dot{m}_{cool}$ [kg/s]
6-8 Acceleration	1.555	0.2815
8 Cruise	0.5439	0.4622
8-10 Acceleration	2.289	0.6895
10 Cruise	0.6952	0.9265
10 Turn	0.7481	0.8651
10-8 Deceleration	0.4217	0.6926

Now, since a differential marching scheme to model flow properties is used here, one must consider the impact of step size on results. The smaller the step size, the more accurate the results, yet the larger the computational burden. To measure the effect of step size on the calculated results, two cases were examined in the nozzle. Fluid entering the nozzle through a 0.1 m<sup>2</sup> duct area was assumed to have the following properties: M = 1.5, T = 3200 K, P = 0.7 MPa,  $\gamma = 1.265$ , and R = 300.6 J/kg K. The exit area resulting from the differential analysis using the influence coefficient table (table 3.2 of chapter 3) is compared to the exit area computed with the same exit properties but with the isentropic flow relations given in equations (3.1) and (3.11) through (3.13). When these exit areas converge, the isentropic flow properties are found. For this investigation to be valid, the influence of heat transfer and friction are removed. The results are presented in table 5.3, with  $n$  being the number of steps used in the differential marching scheme.

As can be seen from this table, a step size based on 10,000 steps more accurately predicts the exit properties; however, the computational burden is unacceptable for the hundreds of thousands of mission-level integrated vehicle evaluations that are performed during the optimization process. With 1000 increments, on the other hand, the program over or under predicts the flow properties by roughly one percent, an acceptable error.

**Table 5.3.** Effects of step size on nozzle exit results.

Property	Entrance	Exit	
		$n = 1000^*$	$n = 10000$
$M$	1.5	5.331	5.302
$T$ [°K]	3200	872.0	879.8
$P$ [Pa]	700000	1406	1466
$A_{diff}$ [m <sup>2</sup> ]	0.1	6.971	7.050
$A_{isen}$ [m <sup>2</sup> ]	0.1	7.314	7.082
$t$ [s]	-	1.360	13.83

\*The step size utilized for this thesis work.

### 5.1.2 Airframe and Engine Sub-systems – Thermodynamic/Flow Conditions

Briefly, to explore the temperatures, pressures, Mach numbers, and general flow conditions over the hypersonic regime studied in this thesis work, some values of component *entrance/exit* conditions will be given for an initial (baseline) solution to the total mission optimized vehicle with a maximum thrust efficiency objective function. When meaningful, these values will be compared to the optimized vehicles presented in Section 5.2. Figure 5.1 shows the locations of the properties discussed while table 5.4 gives their values. The value given in the table is the value at the entrance to each component. For the inlet, the value in the table is given after the forebody energy addition and forebody shock.

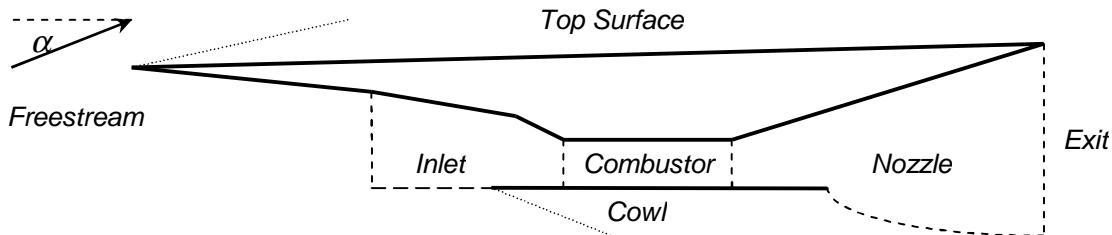


**Figure 5.1.** Hypersonic vehicle flow condition boundaries.

Much can be gained from examining and comparing the values given in table 5.4 over the various components and mission segments. For example, all of the top surface Mach numbers are less than the corresponding freestream Mach numbers for each mission segment, indicating that an oblique shock is occurring, or that the physical angle of the top surface is greater than the vehicle angle of attack. The constant specific heat ratio,  $\gamma$ , at the nozzle entrance and exit for each mission segment follows from the assumption that the nozzle flow is assumed to be frozen. The small change in flow

**Table 5.4.** Flow properties for a thrust efficiency-based objective function baseline vehicle over the entire hypersonic mission.

Mission Segment	Location	$M$	$V$ [km/s]	$P$ [kPa]	$P_t$ [kPa]	$T$ [K]	$T_t$ [K]	$\dot{m}$ [kg/s]	$\gamma$	$\alpha$ [°]
Mach 6 - 8 Acceleration	Freestream	7	2.094	2.475	10.25	221.8	2395	141.9	1.4	1.9
	Inlet	8.093	2.091	2.929	30.83	165.5	2333			
	Combustor	2.924	1.724	215.8	7.070	861.3	2334			
	Nozzle	1.203	1.129	846.2	1964	2206	2645	143.6	1.275	
	Exit	4.752	2.384	2.718	1894	631.0	2591			
	Top Surface	6.940	2.092	2.616	10.25	225.3	2396	141.9 <sup>29</sup>	1.4	
	Cowl	6.650	2.084	3.411	10.21	243.3	2395			
Mach 8 Cruise	Freestream	8	2.403	1.901	18.56	223.5	3084	124.1	1.4	1.6
	Inlet	8.261	2.394	2.714	32.65	208.1	3048			
	Combustor	2.888	1.963	219.8	6.819	1145	3055			
	Nozzle	1.478	1.443	626.8	2116	2396	3107	125.6	1.272	
	Exit	4.893	2.606	2.420	2118	712.9	3033			
	Top Surface	7.851	2.399	2.148	18.56	231.5	3085	124.1	1.4	
	Cowl	7.625	2.394	2.585	18.49	244.3	3085			
Mach 8 - 10 Acceleration	Freestream	9	2.712	1.502	31.70	225.1	3872	109.9	1.4	1.1
	Inlet	8.559	2.700	2.375	36.02	246.7	3861			
	Combustor	2.827	2.195	226.4	6.402	1494	3882			
	Nozzle	1.633	1.689	531.9	2256	2700	3663	111.2	1.268	
	Exit	5.019	2.853	2.174	2353	814.9	3562			
	Top Surface	8.670	2.706	1.917	31.64	241.4	3871	109.9	1.4	
	Cowl	8.676	2.706	1.907	31.61	241.1	3871			
Mach 10 Cruise	Freestream	10	3.023	1.204	51.10	226.5	4757	97.60	1.4	0.9
	Inlet	8.687	3.007	2.220	37.12	296.9	4778			
	Combustor	2.801	2.350	226.7	6.162	1872	4809			
	Nozzle	1.750	1.925	468.3	2380	3061	4297	98.74	1.264	
	Exit	5.122	3.112	2.007	2592	933.9	4164			
	Top Surface	9.529	3.016	1.654	50.93	248.3	4758	97.60	1.4	
	Cowl	9.676	3.018	1.496	50.99	241.1	4756			
Mach 10 Turn	Freestream	10	3.023	1.204	51.10	226.5	4757	97.54	1.4	2.1
	Inlet	7.911	2.966	3.025	27.47	348.3	4708			
	Combustor	2.946	2.476	210.1	7.116	1751	4790			
	Nozzle	1.811	1.967	450.3	2520	2981	4274	98.69	1.265	
	Exit	5.126	3.102	2.101	2715	925.6	4142			
	Top Surface	9.953	3.022	1.241	51.04	228.5	4756	97.54	1.4	
	Cowl	9.264	3.011	1.975	50.44	261.9	4757			
Mach 10 - 8 Deceleration	Freestream	9	2.712	1.502	31.70	225.1	3872	109.9	1.4	0.9
	Inlet	8.687	2.702	2.248	37.58	239.7	3857			
	Combustor	2.801	2.188	229.5	6.238	1512	3885			
	Nozzle	1.622	1.682	535.6	2235	2711	3666	111.2	1.268	
	Exit	5.020	2.855	2.156	2339	815.6	3564			
	Top Surface	8.613	2.705	2.000	31.61	244.5	3872	109.9	1.4	
	Cowl	8.735	2.707	1.827	31.67	238.1	3872			

properties from freestream to cowl is a result of the small oblique shock due to the angle of attack. Practically, if forebody, first, and second inlet ramps are meant to converge before the cowl lip to avoid

<sup>29</sup> The given mass flow rates and specific heat ratios for the top surface and cowl are the values used to calculate the exergy destruction due to the shocks and friction occurring at those surfaces.

high temperatures (as mentioned in Chapter 3), an expansion would occur right beneath the lip to follow the geometry of the cowl wall, yielding a similar flow Mach number as a consequence of an equal total flow turning angle (the angle of attack). However, property variations and total pressure losses would result from the irreversibilities associated with the forebody and inlet shocks, affecting frictional and pressure forces acting beneath the vehicle. The small static pressure change from freestream to inlet and the large static pressure change from inlet to combustor over each of the segments illustrate the purpose behind including the forebody in the airframe sub-system and inlet in the propulsion sub-system. Of course, their contributions to aerodynamic forces and moments on the vehicle should be examined as well. These effects will be discussed in Section 5.1.5.

The benefit of the shock-on-lip inlet design utilized for this thesis work presents itself in table 5.4. The angles of attack ( $\alpha$ ), none surpassing 2.1 degrees, illustrate the sensitivity of the vehicle as well as the capability of the inlet control system to maintaining relatively level flight throughout the mission segments. Furthermore, despite the large variation in freestream Mach number, the inlet Mach number varies through each mission segment between just Mach 7.91 and Mach 8.69. For a fixed geometry vehicle, this allows the greatest possibility of mass capture. The forebody angle and incoming Mach number (after flow manipulation via energy interaction) are both fixed entering the inlet. The reason for the variance in inlet Mach number is due to changing angle of attack. As a result, the need for a second energy interaction before the inlet ramp to maintain shock-on-lip becomes apparent. The trade-off of this design is that, though maximum flow is captured and the Mach number is constant, temperatures and pressures vary greatly at the inlet entrance (compare 165.5 °K for the Mach 6 to Mach 8 acceleration versus 348.3 °K for the Mach 10 turn). This model would not be feasible if the combustor entrance constraints, as identified in Chapter 3, could not be met. An in-depth audit of the shock-on-lip inlet design follows.

### **5.1.3 Airframe and Engine Sub-systems – Shock-on-Lip**

The unique model developed and implemented here for shock-on-lip manipulation involves both the airframe and engine subsystems, it is useful to investigate its overall performance and characteristics. Table 5.5 shows the exergy destruction of the flow manipulation or control sub-system as well as that for the total vehicle at each mission segment for the baseline vehicle described in the previous section. The potential benefit of this manipulation or control is immediately evident by inspecting the fraction of

total exergy destruction plus fuel exergy loss for which the inlet tailoring mechanism is responsible<sup>30</sup>. Except perhaps for the Mach 6 to Mach 8 acceleration, it is an insignificant contribution to the total exergy destruction plus fuel exergy loss of this system. However, it should be noted that no efficiency considerations associated with the energy (exergy) removal or addition process were taken into account, implying that an actual process may be, for example, as much as four times as demanding. This less efficient mechanism would nonetheless still account for less than five percent of the overall exergy destruction plus fuel exergy loss. This is far outweighed by the benefits of such control which significantly affects overall vehicle performance by avoiding shock ingestion or mass spillage at the engine inlet. Markell, for example, showed that mass spillage can cause a reduction in thrust of 50 percent for a Mach 9 designed vehicle geometry flying at Mach 7 [9]. Furthermore, the overall contribution of the tailoring system to the overall exergy destruction remains relatively constant from initial to final optimal solutions.

**Table 5.5.** Shock-on-lip exergy destruction [GJ] for the baseline thrust efficiency-based objective function vehicle.

Segment	Forebody Exergy Destruction	Ramp 1 Exergy Destruction	Total Inlet Tailoring Exergy Destruction	Total Vehicle Exergy Destruction	Inlet Tailoring Contribution [%]	Total Vehicle Exergy Destruction + Fuel Exergy Loss	Inlet Tailoring Contribution [%]
Mach 6-8 Accel.	0.2950	0	0.2950	5.215	5.66	15.67	1.88
Mach 8 Cruise	0.4177	0.0090	0.4268	25.93	1.65	33.34	1.28
Mach 8-10 Accel.	0.0030	0.0094	0.0124	4.733	0.26	21.16	0.06
Mach 10 Cruise	0.0766	0.0892	0.1658	27.63	0.60	40.53	0.41
Mach 10 Turn	0.2000	0.0031	0.2031	26.01	0.78	40.17	0.51
Mach 10-8 Decel.	0.0293	0.0893	0.1185	21.88	0.54	25.42	0.47
TOTAL	1.022	0.2000	1.222	111.4	1.10	176.3	0.69

The exergy destruction for the Mach 8 to Mach 10 acceleration and Mach 10 to Mach 8 decelerations might seem to imply that the necessary energy (exergy) exchanged with the flow for shock-on-lip control should be zero, since an average Mach 9 flight condition<sup>31</sup> is assumed for the segment. In other words, since the average freestream Mach number for these two segments is 9 (as

<sup>30</sup> Note that this exergy destruction translates directly into an amount of fuel exergy destroyed either for shock-on-lip control or for overcoming all the vehicle loss mechanisms due to system irreversibilities.

<sup>31</sup> Section 5.1.5 details the effects of assuming an average Mach number for an entire mission segment and mission segment discretization.

discussed in Chapter 4) and  $M_{Design} = 9$  after the control volume in front of the forebody and before the forebody oblique shock, then no energy exchange is required. The design segment (i.e. when the vehicle geometry is determined) occurs during the Mach 6 to Mach 8 acceleration for which the average Mach number is 7. Tailoring the Mach 7 flow to the design Mach 9 flow for the shock-on-lip required condition is the most demanding. Thus, a vehicle geometry is found which can accommodate this flow transition from Mach 7 to Mach 9. This results in a forebody angle, for example, which provides a shock-on-lip condition for Mach 9 at the angle of attack of the vehicle during this vehicle design mission segment and, thus, energy (exergy) must be exchanged with the flow prior to the forebody for each successive mission segment (e.g., the Mach 8-10 acceleration or Mach 10-8 deceleration) in order to maintain  $M_{Design} = 9$  for changing conditions of angle of attack and freestream Mach number.

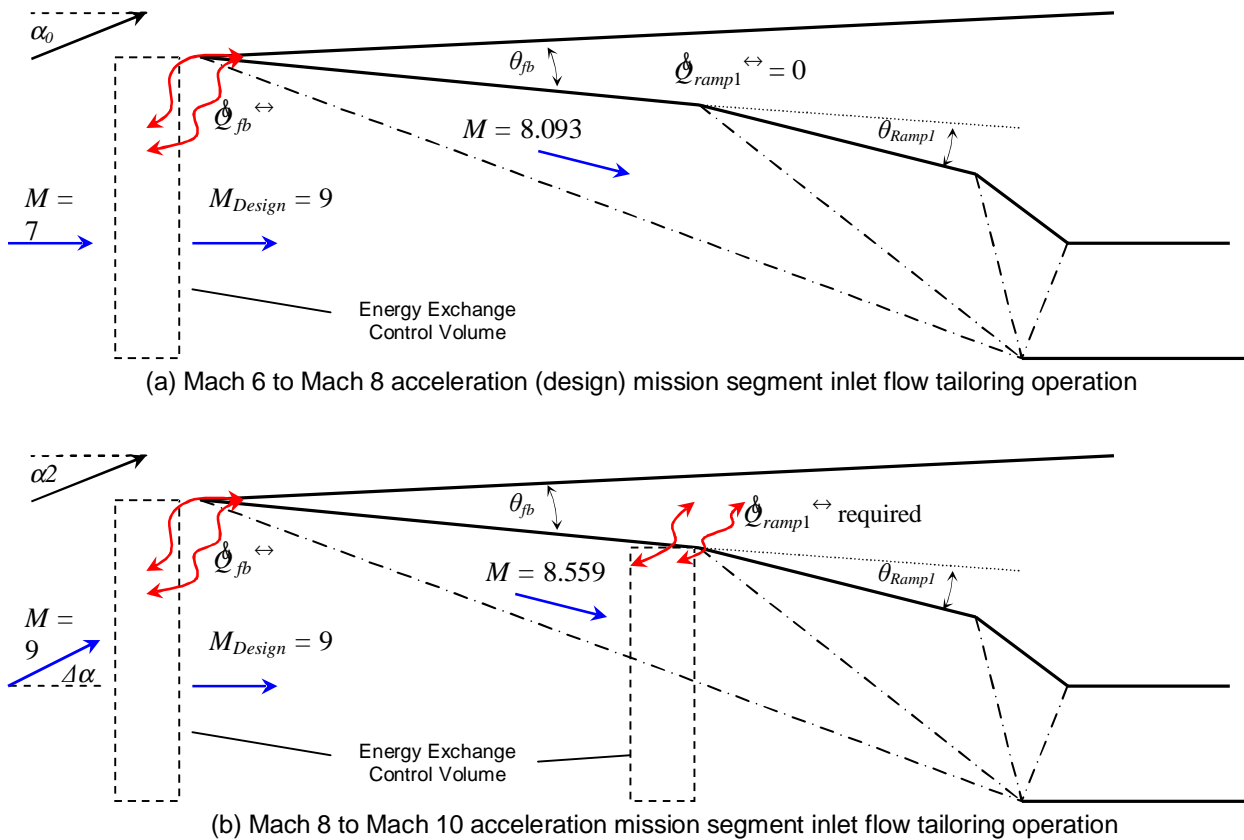


**Figure 5.2.** Inlet flow dynamics for shock-on-lip control for (a) Mach 6 to Mach 8 (design) and (b) Mach 8 to Mach 10 acceleration mission segments. Values given for the inlet Mach number are from the baseline thrust efficiency-based objective function vehicle described in table 5.4.

Figure 5.2<sup>32</sup> provides an illustration of the two specific operating conditions mentioned previously. The values for this discussion were drawn from vehicle properties given in table 5.4. For the Mach 6 to Mach 8 acceleration, the flow is brought from Mach 7 to Mach 9 via energy exchange. Since the vehicle geometry is designed during this mission segment, there is no need for a second energy exchange after the forebody shock and before the inlet. The first ramp shock will fall on the cowl lip with an entering inlet Mach number of 8.093. During the Mach 8 to Mach 10 acceleration, the freestream Mach number is already 9 (the average Mach number for the mission segment), yet it is at a different angle of attack. Energy exchange corrects this angle, and the flow is again at  $M_{Design} = 9$ . However, due to the change in angle of attack, a weaker forebody shock<sup>33</sup> causes the inlet Mach number to be 8.559, and thus energy is exchanged a second time to correct the flow. The difference between the two energy exchange control volumes is that the first brings the Mach number to a design Mach number, namely  $M_{Design} = 9$  while the second ensures shock-on-lip and is dependent on the geometry designed during the first mission segment.

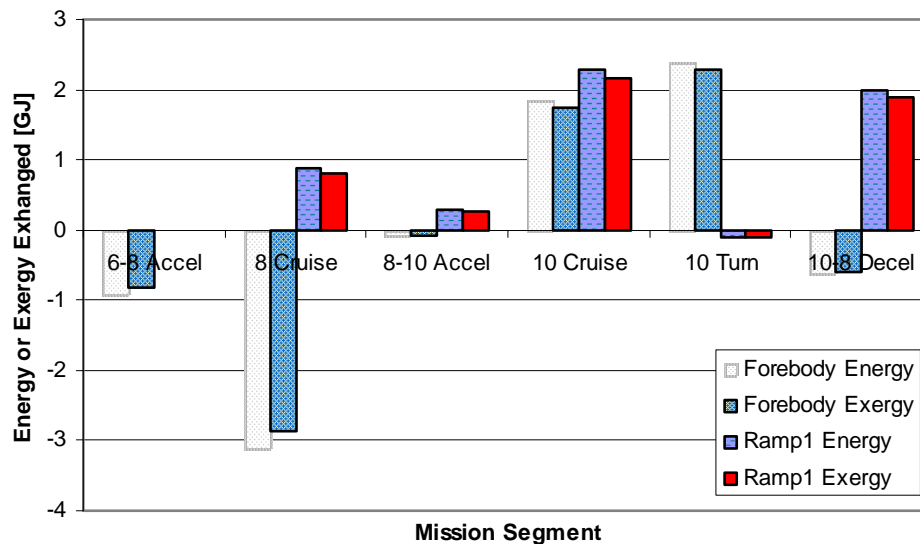


**Figure 5.3.** Required energy/exergy addition for the baseline thrust efficiency-based objective function vehicle.

Figure 5.3 shows energy/exergy addition or removal required to tailor the system to the desired shock-on-lip condition. Values above the horizontal axis correspond to energy/exergy being added, while those below indicate removal. Though its contribution to the overall exergy destroyed and lost is small, the magnitude of energy and somewhat less so the exergy which must be introduced or removed

<sup>32</sup> The angles in the figure were exaggerated for illustration, and again, though the control volume for the first ramp energy exchange is drawn to cross the forebody oblique shock, it is assumed to interact only with the flow after it.

<sup>33</sup> A weaker oblique shock is evident from the result that the inlet Mach number for the Mach 8 to Mach 10 acceleration segment is greater than the inlet Mach number for the Mach 6 to Mach 8 acceleration segment.

is significant. However, the net exchange only represents a small fraction (on the order of 2 - 4%) of the total fuel exergy or exergy consumed. Nonetheless, since its magnitude is not negligible, designing and producing a flight-worthy physical mechanism capable of the dynamic energy/exergy exchange needed is indeed a difficult task. Even so, its potential benefits make it a challenge worth exploring.

### 5.1.4 Airframe and Engine Sub-systems – Airframe and Propulsive Trim Effects

Much like Section 5.1.2, the following discussion focuses on presenting typical forces on the vehicle throughout the hypersonic regime. These include propulsive and airframe contributions with respect to vehicle trim considerations. When possible, these values will be compared to the literature. Again, the following values are from the baseline vehicle for the thrust efficiency-based objective function.

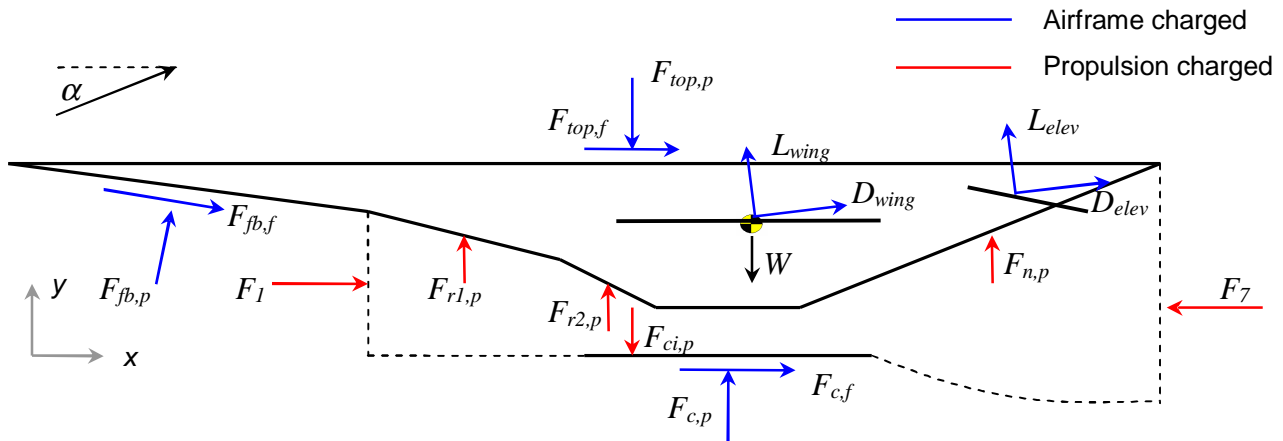


**Figure 5.4.** Airframe and propulsive forces acting on the hypersonic vehicle.

Figure 5.4 illustrates the forces acting on the hypersonic vehicle. Not shown is the force acting downward on the cowl extension inside the nozzle. As the pressure forces on the nozzle ramp and cowl extension surface are the same, the force and moment contributions of the cowl extension in the nozzle are subtracted from the much larger force and moment contributions of the nozzle ramp, thus the force given for the nozzle ramp is an effective force. Again, since the wing center of pressure is assumed to pass through the vehicle center of mass, no moment is attributed to the wing. Also, the friction and pressure forces acting within the propulsion sub-system along the vehicle centerline (the  $x$ -direction as given in figure 5.3) are captured as part of the inlet and exit streamthrusts,  $F_1$  and  $F_7$ , respectively.

**Table 5.6.** Breakdown of moments due to surface forces for the baseline thrust efficiency-based objective function vehicle. For the vehicle shown in figure 5.4, positive values indicate a clockwise (nose-up) moment.

	Moment Location	Mach 6-8 Accel.	Mach 8 Cruise	Mach 8-10 Accel.	Mach 10 Cruise	Mach 10 Turn	Mach 10-8 Decel.
Propulsive	Stream Thrust In, $M_I$	-224.1	-224.1	-223.6	-220.9	-220.7	-223.6
	Stream Thrust Out, $M_7$	209.1	198.3	237.3	213.2	190.6	210.4
	Inlet Ramp 1 Pressure, $M_{r1,p}$	124.8	120.5	113.1	108.9	125.7	110.2
	Inlet Ramp 2 Pressure, $M_{r2,p}$	-60.1	-58.0	-54.5	-52.4	-60.5	-53.1
	Cowl Lip Pressure, $M_{ci,p}$	205.2	198.0	185.9	179.0	206.6	181.2
	Nozzle Ramp, $M_{n,p}$	-310.1	-257.1	-273.5	-238.3	-249.1	-235.0
Airframe	Top Surface Friction, $M_{top,f}$	1.6	1.7	1.9	1.9	1.6	1.9
	Top Surface Pressure, $M_{top,p}$	-106.5	-87.5	-78.1	-67.4	-50.6	-81.5
	Forebody Friction, $M_{fb,f}$	-0.1	-0.1	-0.1	-0.1	-0.1	-0.1
	Forebody Pressure, $M_{fb,p}$	245.7	227.7	199.2	186.3	253.7	188.6
	Under Cowl Friction, $M_{cf}$	-0.3	-0.3	-0.3	-0.3	-0.3	-0.3
	Under Cowl Pressure, $M_{c,p}$	-14.2	-10.8	-7.9	-6.2	-8.2	-7.6
Totals	Propulsive	-55.2	-22.4	-15.3	-10.5	-7.5	-9.9
	Airframe	126.2	130.8	114.7	114.3	196.1	101.0
	Untrimmed	71.0	108.4	99.4	103.8	188.6	91.2
	Elevon Trim, $M_{elev}$	-71.0	-108.6	-99.5	-104.0	-188.7	-91.2

Table 5.6 gives the values for the pitching moments caused by the forces illustrated in figure 5.4, as well as the moment provided by the elevon to trim the vehicle. Figure 5.5 shows pitching moment distributions for the Mach 6 to Mach 8 acceleration, Mach 10 cruise and Mach 10 turn mission segments to better facilitate the following discussion. Throughout the mission, the pitching moment for the propulsion sub-system produces a nose-down moment, while the airframe sub-system induces a nose-up moment. In every case, the primary contributor to the total untrimmed moment is the airframe sub-system; however, the magnitude ratio decreases significantly as the flight Mach number increases. For example, the ratio of propulsion to airframe sub-system moments is 44 percent for the Mach 6 to Mach 8 acceleration segment, but falls to only 4 percent (arguably negligible) during the Mach 10 turn. This is due to the trend that the total airframe sub-system moment increases and the total propulsion sub-system moment decreases with increasing Mach number. This is interesting because, consistently, the largest overall pitching moment for each segment is induced by the nozzle pressure force (part of the propulsion sub-system). The fact that all elevon moments are negative (as a result of the dominance of the airframe subsystem) indicates that all elevon deflection angles must be positive relative to the flow.

Also evident is that the airframe frictional forces along the top surface, forebody, and lower cowl surface induce negligible moments in all mission segments (they are therefore omitted from figure 5.5).

The sensitivity of the vehicle to angle of attack is once again revealed by examining the forebody pressure moment for the Mach 10 cruise and Mach 10 turn segments. Though the angles of attack vary only by 1.1 degrees (see table 5.4), the pitching moment is 36 percent greater for the Mach 10 turn. This is, of course, somewhat dependent on the inlet flow tailoring system as well. The elevon model used for trimming vehicle pitching moment was indeed successful, as demonstrated by the difference in total untrimmed moment and elevon provided moment. This is in fact a consequence of allowing the elevon angle to vary in increments of 0.1 degrees within the solution procedure. The elevon's value, however, should be assessed only after considering its contribution to lift and drag as well. This discussion follows shortly.

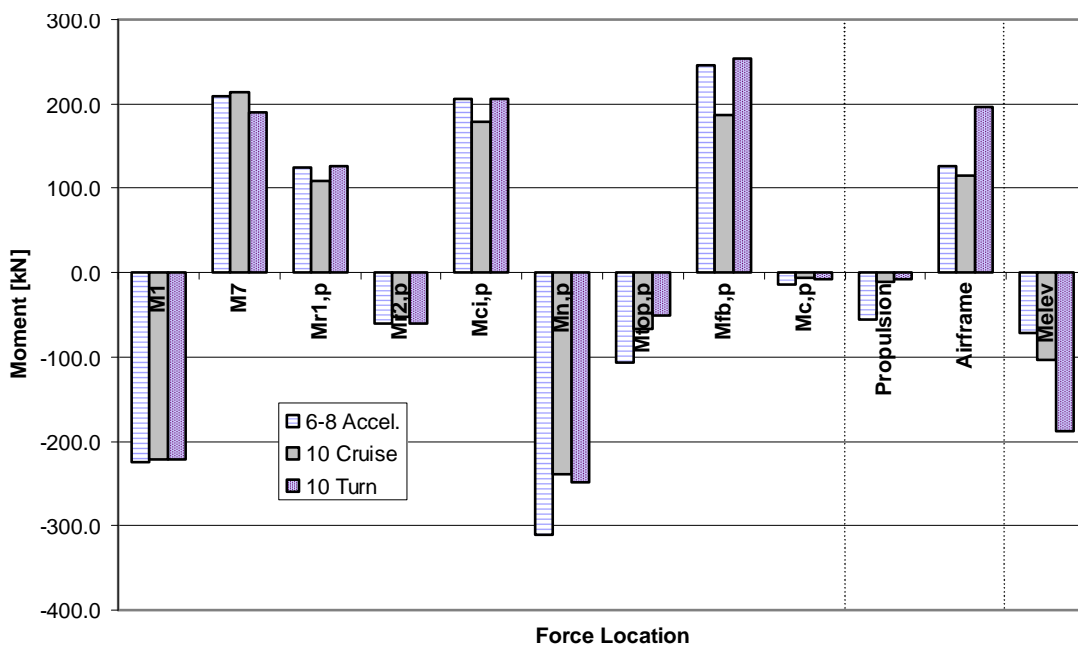


**Figure 5.5.** Airframe and propulsive moments acting on the hypersonic vehicle. Positive values indicate a nose-up pitching moment.

The consistent nose-down trim requirement is not uncommon. NASA's X-43, introduced in Chapter 1, utilizes an 800 lb slab of dense tungsten (which composes 29 percent of the vehicle's gross weight) placed in the forebody of the vehicle to shift the center of gravity forward [58]. Assuming this mass does not translate, an elevon would still likely be needed for trim during multiple mission segments. However, if the moment is partially trimmed by rearranging the center of gravity, such that the elevon need only traverse small positive and negative angles, then the drag on the vehicle can necessarily be reduced, since the elevon drag coefficient increases with deflection angle from a minimum value of  $C_{D0}$  at zero inclination to the flow. To measure the benefit of this approach, the

savings in drag reduction must be compared to the effect of increasing the gross vehicle takeoff weight (if necessary). For these reasons, the exploration of an internally translating mass would likely be worthwhile. In this case, the drag reduction would have to be compared to the effect of increasing the vehicle volume, if necessary, to accommodate translation, in addition to the possibly increased initial weight.

Comparing the results in table 5.3 and figure 5.4 to the literature, the following qualitative conclusions can be drawn. In all studies, the contribution and sub-system location of pitching moments shifts as flight Mach number varies, all of which is a drastic change from conventional aircraft. These shifts are more pronounced in the literature and include circumstances in which the propulsion sub-system can be much larger [59]. This is likely a result of different force accounting methods. For example, including the above forebody moments in the propulsion sub-system (as in a nose-to-tail force accounting method) could greatly change the airframe/propulsion sub-system pitching moment distribution. It is difficult, however, to make distinct comparisons to the literature since, for example, the distribution of moments given by Bowcutt not only include the nose-to-tail force accounting system, but also traverse a different range of Mach numbers with a different vehicle geometry, center of gravity, etc. [59]. All vehicles in the literature do consistently traverse small angles of attack (less than 8 or 10 degrees) [5, 25, 59]. The vehicles in this thesis work do not exceed 2.5 degrees. This is a result of the inlet tailoring mechanism. Because the flow is manipulated prior to the forebody shock, larger angles of attack need not be traveled to adjust for the effect of flow spillage on vehicle thrust. Consequently, relatively few changes in pitching moment location and distribution occur for the optimum vehicles (compared to their respective baselines). This is not the case for the thrust and drag as will be demonstrated in Section 5.2.3.

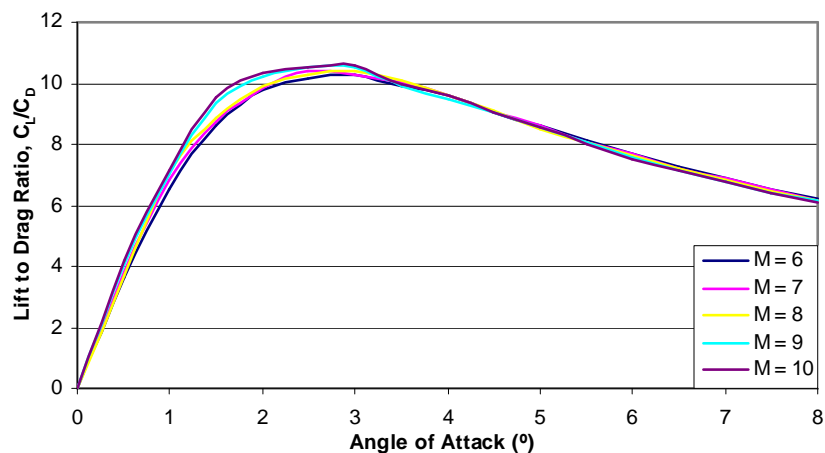


Figure 5.6. Lift to drag ratio for the diamond airfoil.

The lift-to-drag ratio of the diamond airfoil wing and elevon models is plotted in figure 5.6 (initially introduced in Section 3.4.3). At each Mach number, as illustrated, the maximum lift-to-drag ratio occurs between two and three degrees angle of attack, with a ratio value slightly greater than ten. This is consistent with the same diamond airfoil modeled by Bowcutt [25] in which his Mach 15 maximum lift to drag ratio of 10.1 corresponded to an angle of attack of 2.5 degrees. Bowcutt’s integrated hypersonic vehicle traversed angles of attack up to eight degrees, again showing the need for a sensitive vehicle control system. While Bowcutt maintained shock-on-lip, the mission consisted of a single cruise segment; thus, a single geometry always satisfied the constraint.

### 5.1.5 Airframe and Engine Sub-systems – Airframe and Propulsive Lift and Drag Effects

Much like Section 5.1.2, the following discussion focuses on presenting typical forces on the vehicle throughout the hypersonic regime. These include propulsive and airframe contributions to the lift and drag for the baseline vehicle previously discussed. The breakdown of contributors to the overall vehicle drag (consisting of airframe body, wing, elevon, and weight components), dependent variables of interest, and vehicle actual and required thrust, are given in table 5.7. A plot of the drag contributions for each mission segment is given in Figure 5.7.

**Table 5.7.** Breakdown of overall vehicle drag for the baseline thrust efficiency-based objective function vehicle.

		Mach 6-8 Accel.	Mach 8 Cruise	Mach 8-10 Accel.	Mach 10 Cruise	Mach 10 Turn	Mach 10-8 Decel.
Dependent Variables	Equivalence Ratio	0.42	0.18	0.76	0.26	0.30	0.14
	Wing Area, [m <sup>2</sup> ]	6.59	6.57	2.96	4.16	9.116	4.64
	Elevon Angle [°]	3.56	5.12	4.86	4.96	6.78	4.59
Drag [kN]	Body	7.650	6.437	5.991	5.487	3.837	5.852
	Elevon	0.867	1.556	1.389	1.471	3.285	1.234
	Wing	1.299	1.042	0.360	0.440	1.543	0.533
	Weight	1.205	0	0.687	0	0	-0.077
	Total	11.020	9.035	8.427	7.398	8.665	7.542
Vehicle Performance [kN]	Thrust	55.035	9.014	48.486	8.241	8.621	2.293
	Thrust - Drag	44.015	-0.021	40.059	0.843	-0.044	-5.249
	Required Thrust - Drag	43.656	0	39.614	0	0	-5.330

As one would expect, the equivalence ratios are greatest for the two acceleration mission segments, in which a positive net thrust (thrust minus drag) is required. The last two rows of table 5.7 show the actual and required thrust minus drag for a segment. The required value is based on Equations (4.1) and (4.2) and given in table 4.3<sup>34</sup>. The actual thrust minus drag is calculated by the program. The fact that these two values are not equal is not an indication of fair or poor vehicle performance but is an artifact of the program code which governs that the equivalence ratio can only vary in increments of 0.02. The difference between the last two rows of table 5.6 should always converge to zero; however, as indicated, adequate results can be gained in a much timelier manner by the employed method of throttling.

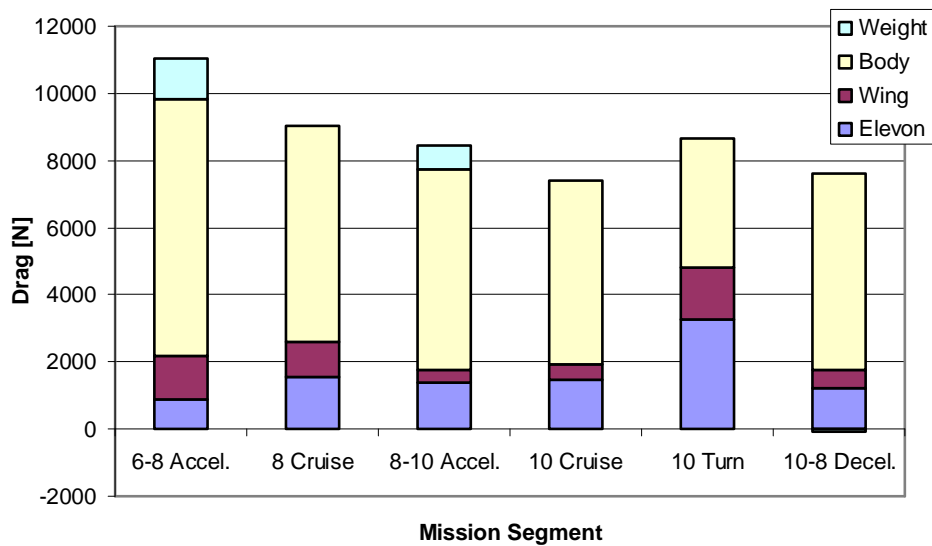


**Figure 5.7.** Component contributions to overall vehicle drag per mission segment for the baseline thrust efficiency-based objective function vehicle.

As shown in figure 5.7, the largest drag occurs during the initial segment. This is to be expected since the initial segment has the largest thrust minus drag requirement due to the inclination angle (to maintain constant dynamic pressure) and the fact that the fuel mass is the greatest (since none is assumed burned at the beginning of the segment). The weight component of drag is due to the inclination/declination angles required during each respective climb/descend mission segment. As expected, this component reduces overall drag (or reduces the necessary thrust required) for the Mach 10 to Mach 8 deceleration, which requires a negative thrust minus drag value to decelerate. Also evident is

<sup>34</sup> These values will not correspond (with the exception of the initial mission segment) due to the fact that table 4.3 shows values based on the assumption that the total estimated mass fraction of fuel is burned during each segment. Fuel usage will, of course, depend on how efficiently the vehicle can utilize it and thus will vary as the vehicle is optimized.

that the wing and elevon components of drag for the Mach 10 turn account for 56 percent of the drag, while in all other segments they total less than 30 percent. This result is the combination of the increased load factor for the turn (reference Section 4.1.3) and that the largest trimming moment is required (see figure 5.5). As indicated in table 5.6, the largest wing area and elevon deflection angle are required during this segment. As will be shown, this is the case for all of the optimized vehicles. The larger drag contribution of the elevon (and hence larger lift, since both elevon and wing are diamond airfoils) implies that there exists opportunity for further geometric optimization between the wing and elevon. For this research, as described in Chapter 3, the elevon area and location are fixed while the wing is attached to the vehicle at fixed angle of attack (zero) and acts through the vehicle center of gravity. Varying these parameters one might find only a wing *or* elevon is necessary. However, this would prove a multi-iterative solution procedure beyond the scope of this thesis work. The assumptions used here facilitated the speedy and accurate iteration and resolution of vehicle forces.

Table 5.8 shows the contributions of propulsion and airframe sub-systems to overall vehicle lift for the baseline thrust efficiency-based objective function vehicle geometry. The effective weight for each segment is the amount of lift the vehicle must provide based on the load factor. As given in table 4.3, the load factor for all mission segments but the turn is one. For all of these segments, the lift required is equal to the weight of the vehicle. For the turn, the lift required is double the weight (load factor equal to two). The total lift and effective weight are equal in all cases because unlike the iterative trim and throttling processes, the wing area is solved to precisely yield the lift needed (in the form of a wing area solved to several decimal places), so long as the required area is less than the maximum value (again constrained to be less than 9.6 m<sup>2</sup>).

**Table 5.8.** Propulsion and airframe sub-system contributions to overall vehicle lift for the baseline thrust efficiency-based objective function vehicle.

	Mach 6-8 Accel.	Mach 8 Cruise	Mach 8-10 Accel.	Mach 10 Cruise	Mach 10 Turn	Mach 10-8 Decel.
Propulsive Lift [kN]	69.065	58.138	61.078	54.003	57.172	53.361
Airframe Lift [kN]	-8.240	1.155	-5.650	-0.738	40.589	-9.192
Total Lift [kN]	60.825	59.293	55.428	53.265	97.761	44.169
Effective Weight [kN]	60.825	59.293	55.428	53.265	97.761	44.169

In almost all segments shown in table 5.8, the propulsive lift compensates for the negative lift caused by the vehicle airframe. To understand this phenomenon, a breakdown of vehicle lift by each individual force (see figure 5.4) is given in table 5.9 for the Mach 6 to Mach 8 acceleration mission

segment. Decomposing the airframe and propulsion sub-system forces, it is evident that the shock occurring on the top surface of the vehicle is responsible for the negative lift of the airframe. This contribution could be diminished by either allowing the vehicle to traverse larger angles of attack or promoting a vehicle geometry in which the forebody nose angle is reduced. Also evident is that the frictional contributions to lift are negligible. The distribution of lift for the optimal vehicles is discussed in Section 5.2.1.

**Table 5.9.** Breakdown of vehicle lift (by force) showing contributions to overall vehicle lift for the baseline thrust efficiency-based objective function vehicle.

Sub-system	Location (force)		Lift [kN]
Airframe	Body	Top Surface Pressure ( $F_{top,p}$ )	-62.822
		Top Surface Friction ( $F_{top,f}$ )	0.012
		Forebody Pressure ( $F_{fb,p}$ )	26.860
		Forebody Friction ( $F_{fb,f}$ )	-0.068
		Under Cowl Pressure ( $F_{c,p}$ )	6.566
		Under Cowl Friction ( $F_{c,f}$ )	0.203
	Elevon		8.587
	Wing		12.422
	Total		-8.240
Propulsion	Ramp 1 Pressure ( $F_{r1,p}$ )		49.575
	Ramp 2 Pressure ( $F_{r2,p}$ )		101.334
	Inside Cowl Pressure ( $F_{ci,p}$ )		-142.581
	Nozzle Ramp ( $F_{n,p}$ )		60.738
	Total		69.065
Total			60.825

Again, the choice of force accounting system impacts the distribution of lift for the two sub-systems. As an illustration, figure 5.8 shows the airframe and propulsion sub-system contributions to lift in three different force accounting systems for the Mach 6 to Mach 8 acceleration mission segment (again for the baseline thrust efficiency-based objective function vehicle). For the nose-to-tail force accounting system, the forebody contributions are considered a part of the propulsion sub-system, while for the cowl to tail force accounting system, the inlet ramps are transferred to the airframe. Essentially, figure 5.8 shows that though the categorization of forces may vary, the end result is the same.

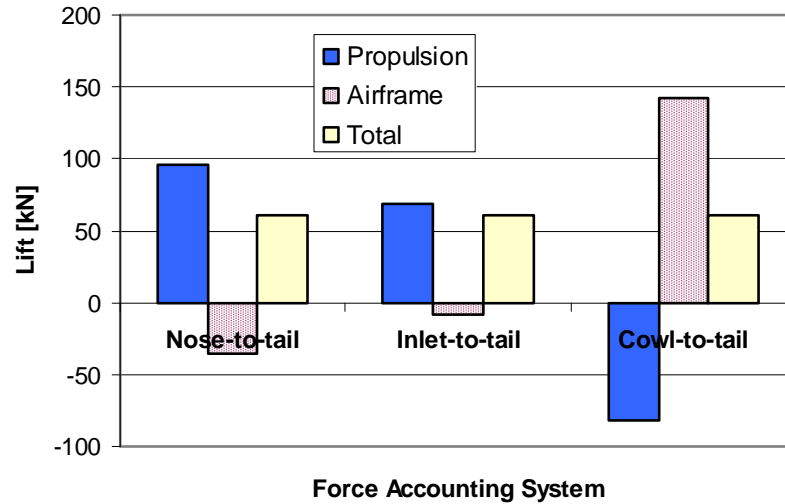


**Figure 5.8.** Breakdown of sub-system charged lift for nose-, inlet-, and cowl-to-tail force accounting systems. Values are given for the Mach 6 to Mach 8 acceleration segment of the baseline thrust efficiency-based objective function vehicle.

### 5.1.5 Effects of Single Segment Discretizations

This section examines the effects discretizing two non-optimized mission segments to observe any variations in vehicle performance predictions when compared to the non-discretized case. Ultimately, the need of a mission-level analysis is to utilize as many mission segments as needed to adequately, with varying degrees of fidelity, model the continuous mission which the aircraft must fly in going from point A to point B. In this thesis work, it was assumed that six segments were adequate for determining, for example, how the fuel burned affects total aircraft mass. One might reason that six segment approximation, as opposed to a higher number approximation, necessarily requires a larger initial fuel mass since the mass fraction assumed at the beginning of each mission segment is fixed for the entire segment, and, hence, more mass is being carried along throughout each mission segment than is needed. However, in a highly integrated vehicle, it is difficult to know a priori how a change of mass may impact the vehicle performance. For example, a lighter mass might require a smaller wing area, reducing vehicle drag, or if the wing area is already negligible, reduce the angle of attack of the vehicle, resulting in any number of possibilities regarding vehicle performance. Thus, a sensitivity study into the effect of further discretizations (i.e. more mission segments) on vehicle performance is performed here.

Two cases, a Mach 8 to Mach 10 acceleration and a Mach 10 cruise are broken into one, two, and four segments to attempt to understand the effect of further discretization on the two types of

mission segments considered in this study. For the Mach 8 to Mach 10 acceleration, the ninety second acceleration is broken into two 45 and four 22.5 sec segments. The effects on mission specific constraints are illustrated in table 5.9<sup>35</sup> (the development of which are governed by equations (4.1) through (4.10) as described in Chapter 4). It should be noted that the vehicle geometries flown in these segments are not optimized, i.e. a single working set of design variable values is used although the angle of attack selected happens to correspond to that which destroys the least exergy.

**Table 5.10.** Effects of further discretizations on mission specific constraining equations for the Mach 8 to Mach 10 acceleration mission segment.

No.	Mission Segment	$t_{ms}$ [s]	$T_{veh} \cdot D_{veh}$ [kN]	$\theta$ [°]	$R$ [km]	$\Delta h$ [km]	$\Delta V$ [m/s]	$M_{avg}$ [m/s]
1	Mach 8-10 Acceleration	90	36.87	0.71	244.5	3.03	620	9
	TOTAL	90	-	-	244.5	3.03	620	-
1	Mach 8-9 Acceleration	45	36.60	0.78	116.0	1.58	309	8.5
2	Mach 9-10 Acceleration	45	36.80	0.64	129.8	1.45	311	9.5
	TOTAL	90	-	-	245.8	3.03	620	-
1	Mach 8-8.5 Acceleration	22.5	36.80	0.82	55.9	0.80	154	8.25
2	Mach 8.5-9 Acceleration	22.5	36.16	0.76	59.2	0.78	155	8.75
3	Mach 9-9.5 Acceleration	22.5	35.53	0.68	62.8	0.74	155	9.25
4	Mach 9.5-10 Acceleration	22.5	35.73	0.61	66.2	0.71	156	9.75
	TOTAL	90	-	-	244.1	3.03	620	-

As to the Mach 10 cruise, it is simply broken into two 300 and four 150 sec segments, requiring no modified constraint equations because constant altitude and speed is maintained (again, this is how cruise is defined in this study). The segments were limited to a maximum of four based on the time required to perform the evaluations, implying that having a program capable of accommodating real time updates or highly discretized evaluations would require either very simplified models or much greater computing power. A number of variables including fuel usage and exergy destruction plus fuel exergy loss for the different cases are shown in table 5.11.

The Mach 8 to Mach 10 acceleration is somewhat affected by further discretizations though the effects are slight. A fuel savings of one to two percent results for each set of successive discretizations.

<sup>35</sup> A 5000kg vehicle empty mass is assumed to carry only the fuel mass necessary for the segment in this discretization study. For example, the fuel mass fraction given by table 4.3 for the Mach 8 to Mach 10 acceleration is  $\pi_f = 0.0508$ . This differs from the optimizations performed in which the empty mass of the vehicle is 4000kg and the fuel mass fraction is the sum of the fuel mass fractions required for the segment of interest and the segments that follow.

**Table 5.11.** Effects of further discretizations on a number of variables including fuel usage and exergy destruction plus fuel exergy loss.

No.	Mission Segment	$\alpha$ [°]	$\phi$	$\dot{m}_{air}$ [kg/s]	$S_{wing}^*$ [m <sup>2</sup> ]	Fuel Used [kg]	$EX_{DES} + EX_{FUELLOSS}$ [GJ]
Mach 8-10 Acceleration							
1	Mach 8-10 Acceleration	0.8	0.74	107.7	4.736	210.5	14.39
	TOTAL	-	-	-	-	210.5	14.39
1	Mach 8-9 Acceleration	1.068	0.64	113.7	1.696	96.12	6.149
2	Mach 9-10 Acceleration	0.7	0.84	100.8	3.974	111.8	8.193
	TOTAL	-	-	-	-	207.8	14.34
1	Mach 8-8.5 Acceleration	1.068	0.58	117.3	4.354	44.93	2.786
2	Mach 8.5-9 Acceleration	1.0	0.68	110.1	0.9121	49.47	3.263
3	Mach 9-9.5 Acceleration	0.8	0.78	103.7	2.273	53.42	3.777
4	Mach 9.5-10 Acceleration	0.7	0.88	97.95	0.6090	56.94	4.315
	TOTAL	-	-	-	-	204.8	14.14
Mach 10 Cruise							
1	Mach 10 Cruise	1.030	0.28	104.5	0.3776	515.2	39.16
	TOTAL	-	-	-	-	515.2	39.16
1	Mach 10 Cruise	1.030	0.28	104.5	0.3776	257.6	19.58
2	Mach 10 Cruise	0.9	0.28	104.5	1.538	257.6	19.72
	TOTAL	-	-	-	-	515.2	39.30
1	Mach 10 Cruise	1.030	0.28	104.5	0.3778	128.8	9.790
2	Mach 10 Cruise	0.9	0.28	104.5	3.314	128.8	9.860
3	Mach 10 Cruise	0.9	0.28	104.5	1.538	128.8	9.922
4	Mach 10 Cruise	0.8	0.28	104.5	3.852	128.8	9.980
	TOTAL	-	-	-	-	515.2	39.55

\*As indicated earlier, wing planform area is allowed to vary throughout the mission or in this case across a mission segment which is further discretized. This is necessary due to the highly constrained nature of the mission and to the difficulties of a fixed-wing geometry being able to meet all of the mission constraints.

This coincides with the slightly decreasing total exergy destruction plus fuel exergy loss values. Also noticeable is how the assumption of an average altitude affects the mass flow rates of air and equivalence ratios. As the density of air decreases, so does the mass flow rate. To maintain adequate thrust, the equivalence ratio increases accordingly. Though the totals change only slightly, the fuel usage and exergy destruction plus fuel exergy loss for each discretized part of the whole is noticeably greater the higher the average Mach number. The opposite trend is seen for the angle of attack. How

these particular values of  $\alpha$  were chosen (or for that matter,  $\varphi$ ,  $\eta_{air}$ , and  $S_{wing}$ ) is as follows. The vehicle flying the four-segmented mission segment is input into the optimization program until a set of values for  $\alpha$  is found that can meet all four sub-segments. The two-segmented and single mission segments are then simulated with the same set of values until the particular value or values that work(s) is(are) found.

Now, as to the Mach 10 cruise segment, very slight but consistent changes also occurred. Contrary to the acceleration segment discretization, more exergy is destroyed and lost as the segment discretization progresses though these changes are much more subtle. Most of the values for the cruise segment remained unchanged for the discretization although variations in angle of attack and wing area did occur. Furthermore, for both the cruise and acceleration segments, having a variable wing area greatly facilitates level flight.

Finally, the initial assumption of a six segment mission operating at average velocities and Mach numbers does not appear to hinder the results, as improved accuracy only totaled a few percent. However, discretization does provide insight into the parts of the segment which are the most and the least demanding.

## **5.2 Mission-Level Optimization of the Integrated Hypersonic Vehicle**

This section specifically details results of the optimization of the mission discussed in Chapter 4. The emphasis is placed on the role of the objective function in determining vehicle geometry, and hence, the integrated vehicle, which in turn translates into performance and fuel economy.

### **5.2.1 Objective Function and Vehicle Synthesis/Design**

Multiple optimizations were performed for each of the three objective functions presented in Chapter 4. The results of these optimizations are given in table 5.12.

As can be seen in table 5.12, the best thrust efficiency result yielded a vehicle with a 34.52 percent overall efficiency. The resulting best minimum fuel mass objective is 1717 kg, while that for the least exergy destroyed plus fuel exergy lost objective is 140.0 GJ. Multiple optimizations were, as mentioned in Chapter 4, required in order to have some confidence in the so called “globality” of the optimums found. This is, of course, not a proof of “globality” but simply an indicator that, due to the randomness of the evolutionary algorithm used, finding a better solution is not likely. This table

furthermore shows that none of the objective functions was exactly repeatable, though for the thrust efficiency and fuel mass objectives, two results very close to each other were found. A discussion of the optimization process is provided in Section 5.3. For now, the impact of objective function on vehicle design will be discussed.

**Table 5.12.** Integrated hypersonic vehicle objective function values.

Run	Maximum Thrust Efficiency [%]	Minimum Fuel Mass [kg]	Minimum Exergy Destroyed Plus Fuel Exergy Lost [GJ]
1	34.52	1717	140.0
2	34.48	1720	142.3
3	32.97	1744	143.1

Table 5.13 shows the decision variable values for each of the best performing objective functions. Note that the optimal design value for the single operational variable ( $\alpha_0$ ) is that for the Mach 6 to Mach 8 acceleration mission segment. Simply looking at the numbers, it is difficult to draw any conclusions since the minimum fuel mass and minimum exergy objectives are both similar and different. To help clarify, the vehicle geometries are plotted in figure 5.9. As illustrated, the minimum exergy and minimum fuel mass vehicle shapes are nearly identical, while the maximized first law efficiency results in a much broader vehicle. The plots show that the centers of mass are overlapping for the fuel mass and exergy cases, while the center of mass for the thrust efficiency objective is higher and more forward. The effect produced is a nozzle which begins sooner, resulting in a larger exit area, which enables the vehicle with this geometry to produce more thrust, as desired by the objective function. Consequently, the frontal area is necessarily bigger, which causes a larger ingestion of air, resulting in a stronger forebody shock and increased vehicle drag.

**Table 5.13.** Optimum decision variables for the best performing runs of each objective function.

Obj. Fun.	$X_{fb}$ [m]	$X_{cowl}$ [m]	$X_{ramp1}$ [m]	$\theta_{fb}$ [°]	$L_{comb}$ [m]	$v_{nozz}$ [°]	$\%a_{nozz}$ [%]	$\alpha_0$ [°]
Maximum First Law	8.909	13.75	3.258	1.790	0.568	17.43	0.0063	1.687
Minimum Fuel Mass	8.717	14.21	3.932	1.000	0.5000	16.67	0.5020	1.884
Minimum Exergy Destroyed Plus Fuel Exergy Lost	8.544	14.05	3.516	1.266	1.064	16.92	0.0100	2.129

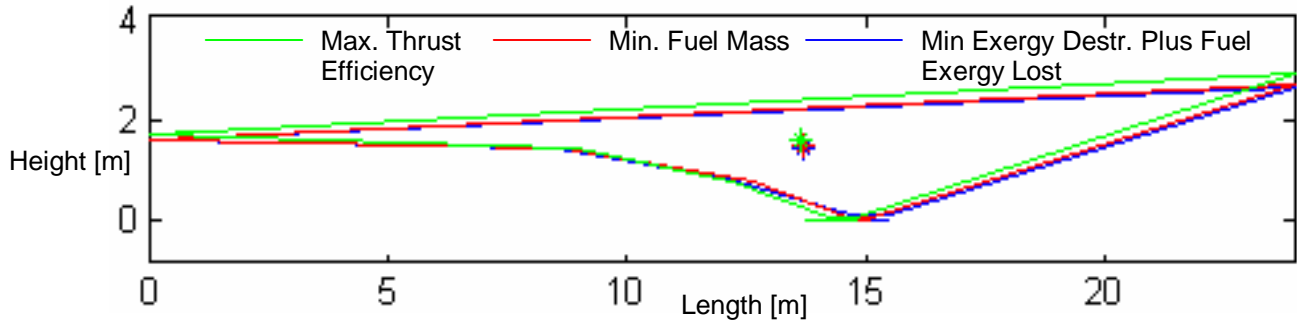


Figure 5.9. Optimum vehicle geometry for each of the three objective functions.

Table 5.14. Mission segment optimum operational variable values.

Segment	$\alpha$ [°]	$\phi$	$S_{wing}$ [m <sup>2</sup> ]	$Q_{fb}$ [GJ]	$Q_{rl}$ [GJ]	$\omega_{elev}$ [°]	$\dot{m}_{cool}$ [kg/s]
Maximum Thrust Efficiency							
6-8 Accel.	1.687 <sup>36</sup>	0.42 <sup>37</sup>	9.556	-0.776	0	3.619	0.2822
8 Cruise	1.4	0.18	9.393	-2.601	0.416	4.399	0.4636
8-10 Accel.	0.9	0.76	5.662	-0.0851	0.193	4.769	0.6835
10 Cruise	0.7	0.26	5.952	1.364	1.774	4.749	0.917
10 Turn	1.9	0.28	9.410	2.157	-0.356	6.462	0.8731
10-8 Decel.	0.8	0.16	4.863	-0.574	1.288	4.129	0.6865
Minimum Fuel Mass							
6-8 Accel.	1.884	0.46	8.913	-0.7271	0	4.519	0.2649
8 Cruise	1.8	0.16	1.306	-2.326	1.159	5.230	0.4325
8-10 Accel.	1.1	0.82	1.504	-0.08985	0.1845	5.130	0.6441
10 Cruise	0.9	0.24	0.2408	1.187	2.711	4.989	0.8639
10 Turn	2.1	0.28	7.246	2.040	-3.466	6.640	0.8208
10-8 Decel.	1.0	0.14	0.4557	-0.6044	1.233	4.490	0.6471
Minimum Exergy Destroyed Plus Exergy Fuel Lost							
6-8 Accel.	2.129	0.40	0.1710	-0.7358	0	4.529	0.2815
8 Cruise	1.6	0.16	0.6670	-2.620	0.7300	4.439	0.4622
8-10 Accel.	0.8	0.76	1.028	0.1451	0.3104	4.149	0.6895
10 Cruise	0.6	0.26	4.207	0.8091	2.622	4.239	0.9265
10 Turn	2.2	0.28	2.114	1.955	-0.1140	6.519	0.8651
10-8 Decel.	0.7	0.14	3.717	-0.9298	1.979	3.750	0.6926

The only significant difference between the exergy and fuel mass cases is that the combustor for the exergy case is double the length. This, as will be illustrated, allows less fuel exergy to be lost in the

<sup>36</sup> The first angle of attack has more significant digits because it is decided by the algorithm. The other angles are found by inputting values within the range required in increments of 0.1 degrees. This is discussed further in section 5.3.

<sup>37</sup> Again, the thrust required by the constraining equations is found by throttling the equivalence ratio in increments of 0.02.

mixing layer of the combustor (recall from Chapter 3 that fuel mixing is a function of combustor length). The specific vehicle volumes are 23.59, 20.96, and 21.48 m<sup>3</sup> for the best performing thrust efficiency, fuel mass, and exergy objectives, respectively. For a fixed mass, this essentially means that a less dense vehicle is produced by the thrust efficiency objective function. How each of these vehicles performs with respect to its optimum operational variable values over each of the mission segments is seen in table 5.15.

Some trends are immediately noticeable. For example, the minimum fuel mass objective tends to fly at the highest angles of attack. Similarly, during the acceleration missions, the minimum fuel mass objective utilizes the largest equivalence ratios, followed by the exergy and then thrust efficiency cases. The body shape of the thrust efficiency vehicle in general promotes a less aerodynamic form, as indicated by the wing areas. More times than not, the thrust efficiency objective pushes the wing area near its maximum allowable area of 9.6 m<sup>2</sup>, thus incurring the associated drag penalty. Another interesting result is that all of the elevon deflection angles are positive and within the range of three to seven degrees. Therefore, a net unidirectional moment is always acting on the vehicle. The relatively small angles which are traversed by the vehicle elevon and angles of attack further demonstrate the sensitivity of the integrated vehicle to slight changes in flight conditions as well as the need for a precision control system.

At first glance, the lower equivalence ratios during acceleration of the thrust efficiency vehicle design seem to imply that less fuel is burned during those segments; however, careful attention must be paid the resulting mass flow rates of air promoted by the geometries of each of the respective vehicles. Table 5.15 illustrates this relationship. The broad body of the thrust efficiency objective requires a larger thrust, via a larger mass flow rate, to meet the constraining mission requirements given in table 4.3, while the numbers for the minimum fuel mass and minimum exergy cases which are almost the same, are less.

**Table 5.15** Optimum vehicle characteristics for each mission segment.

Obj. Fun.	Max. First Law		Min. Fuel Mass		Min. Exergy Destroyed Plus Fuel Exergy Loss		
	Segment	$\dot{m}_{air}$ [kg/s]	Thrust [kN]	$\dot{m}_{air}$ [kg/s]	Thrust [kN]	$\dot{m}_{air}$ [kg/s]	Thrust [kN]
6-8 Accel.		139.6	55.35	130.8	53.54	132.4	55.85
8 Cruise		122.1	13.13	114.4	9.015	115.8	9.850
8-10 Accel.		108.2	49.26	101.3	47.98	102.6	47.81
10 Cruise		96.01	9.789	89.97	7.430	91.06	8.040
10 Turn		95.97	10.13	89.92	8.975	91.00	8.346
10-8 Decel.		108.2	5.638	101.4	3.012	102.6	2.177

The total drag (decomposed by airframe component) on the optimized vehicles over the mission is shown in figure 5.10. As expected, the maximized thrust efficiency vehicle (obj1 in figure 5.10), with broader body, is subjected to the largest amount of drag throughout the mission. The exergy vehicle (obj3) has the least drag in all segments but the deceleration and Mach 10 cruise. In all cases, like the baseline vehicle discussed earlier, the body accounts for the majority of the drag. Also, as the wing areas given in table 5.13 imply, the wing is a significant contributor to drag for every mission segment for the maximum thrust efficiency vehicle, while this is not the case for the minimum fuel mass and exergy objective functions.

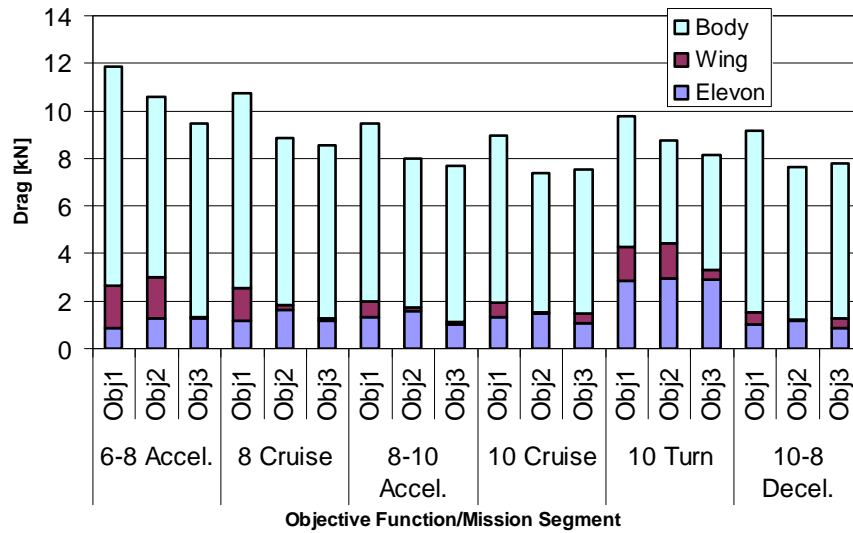


**Figure 5.10.** Drag contribution by airframe component for the optimum vehicles. Obj1, Obj2, and Obj3 are the maximized thrust efficiency, minimum fuel mass, and minimum exergy objective functions, respectively.

Figure 5.11 shows the lift provided by each airframe component. This figure shows that the mission segments which produce little wing drag for the minimum fuel mass and minimum exergy objective function vehicles also add lift, as expected. For the Mach 10 turn, the elevon is the majority contributor to lift. In fact, it is a very significant contributor in every mission segment for all objective functions, again illustrating the need to trim the nose-up pitching moment on the vehicles. This is the case for all three objective functions because the vehicle is at its highest angle of attack during this segment (see table 5.14), thus minimizing the shock occurring on the top surface of the vehicle. The minimum exergy objective function vehicle nearly has positive lift from the vehicle body as it is at the highest angle of attack of all vehicles, and has a slender body like the minimum fuel mass vehicle.

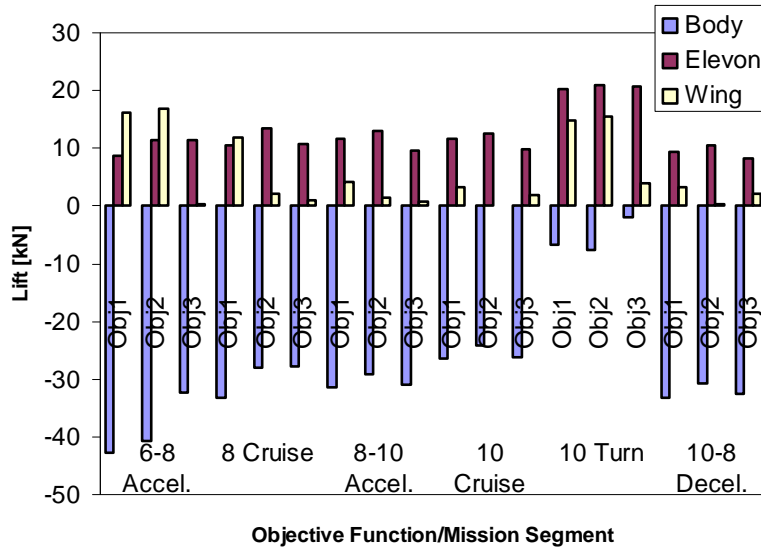


Figure 5.11. Lift contribution by airframe component for the optimum vehicles.

### 5.2.2 Objective Function and Vehicle Mission Segment Exergy Destruction Plus Fuel Exergy Loss

Figure 5.12 shows that the minimum fuel mass and minimum exergy destruction plus fuel exergy loss use similar amounts of exergy consistently in each mission segment, while the best performing maximum thrust efficiency objective function destroys and loses much more exergy per mission segment more times than not. The thrust efficiency objective performs comparably to the exergy and fuel mass objectives only during acceleration segments. In terms of the mission segment trends, each of the objective functions display similar performance characteristics, i.e. the smallest amount of exergy is destroyed during the Mach 6 to Mach 8 acceleration segment for each.

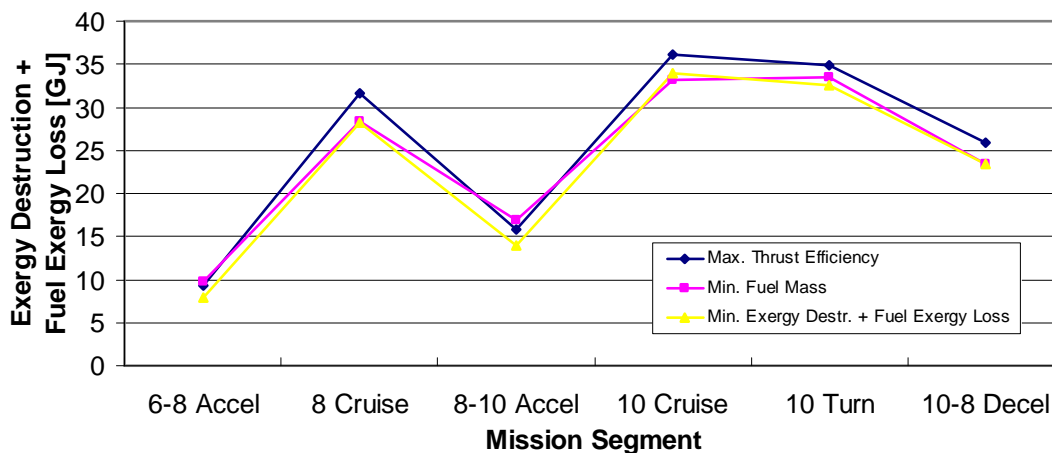
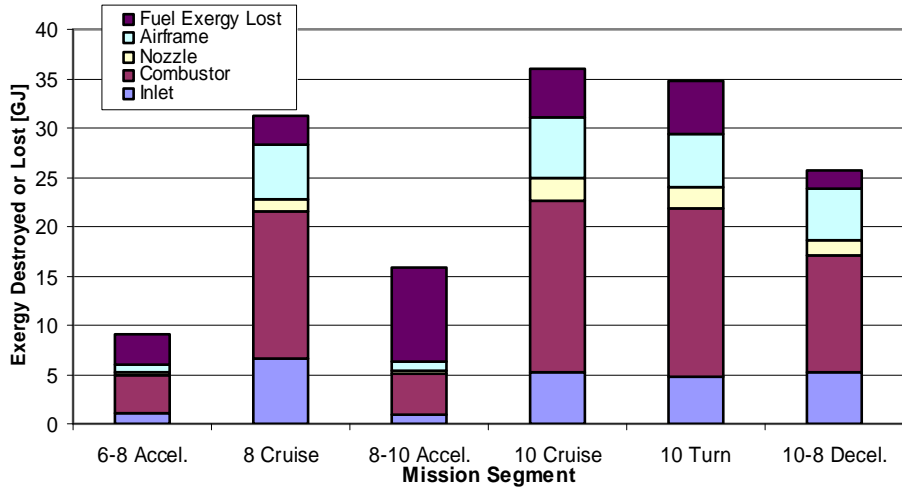
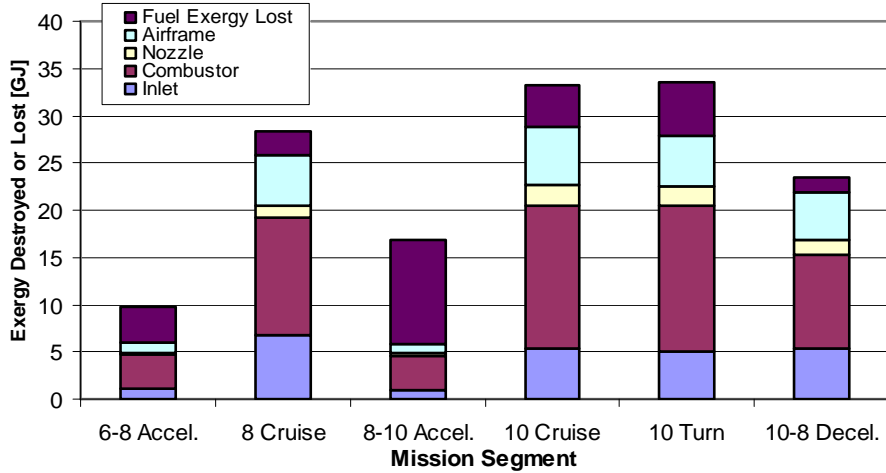


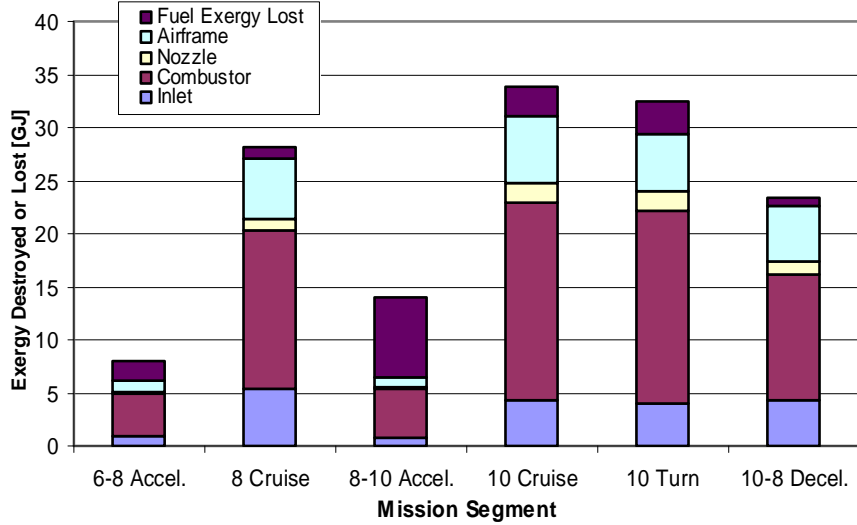
Figure 5.12. Exergy destruction plus fuel exergy loss per mission segment.



(a) Maximum Thrust Efficiency



(b) Minimum Fuel Mass



(c) Minimum Exergy Destroyed Plus Fuel Exergy Loss

Figure 5.13. Exergy destroyed plus fuel exergy lost per mission segment for the best performing integrated vehicles.

For a more detailed breakdown of the exergy destroyed or lost, figure 5.13 shows where the exergy destruction and loss occur (i.e. in the inlet, combustor, etc.) during each mission segment. For all of the objective functions, the combustor consistently proves to be the largest source of loss, except for the case of the Mach 8 to Mach 10 acceleration, in which case the fuel exergy loss is the greatest. For all three objective functions, the inlet, nozzle, and airframe consistently destroy similar amounts of exergy.

Comparing objective functions, the thrust efficiency and exergy objectives both have their largest exergy destruction and fuel loss occur during the Mach 10 cruise mission segment, while the most demanding segment for the fuel mass objective function is the Mach 10 turn. Perhaps the most interesting result is that while the minimum fuel mass and minimum exergy vehicles both destroy and lose similar amounts of exergy, there is an obvious difference in where these occur. In each mission segment the exergy destroyed by the combustor is larger for the minimum exergy vehicle, while in a similar manner, the fuel exergy lost is much greater for the minimum fuel mass vehicle. In essence, there are two ways to arrive at the same efficiency of fuel use. A discussion of how the fuel mass is used for each of the objective functions is discussed next.

### 5.2.3 Objective Function and Vehicle Fuel Consumption

Since each of the vehicles begin the mission with the same gross weight, the best vehicle will burn the least fuel, and have more mass available for payload. This indicates that the fuel is being used most efficiently by meeting the constraints of the mission with the least exergy expended. The minimum fuel consumption should necessarily find the optimal vehicle configuration. How the more traditionally used thrust efficiency objective and the more informative exergy objectives compare to the minimum fuel mass objective is of interest here. The results are presented in table 5.16 and figure 5.14.

Note that there is not one objective function which uses the least fuel mass in all mission segments. Consistent with the conclusion that was drawn from the previous discussion on segment exergy destruction and fuel exergy loss, the thrust efficiency vehicle consumes comparable quantities of fuel to those of the other two objective functions during the accelerations. Due to its poor performance in the other segments, however, the optimized thrust efficiency objective results in a vehicle using 11.1 percent more fuel than the minimum fuel case, from which one can conclude that *the thrust efficiency objective is insufficient when performing an integrated vehicle synthesis/design*. The exergy and minimum fuel cases, on the other hand, are much more alike. The best minimum exergy calculation

yielded a spent fuel mass of 1732, just 15 kg larger than the best performing minimum fuel mass case. This difference is less than one percent, leading to the conclusion that *exergy destruction plus fuel exergy loss and minimum fuel mass objective functions are equivalent in this case.*

**Table 5.16.** Fuel mass used per mission segment.

Mission	Max. First Law [kg]	Min. Fuel Mass [kg]	Min. Exergy Destroyed + Fuel Exergy Lost [kg]
6-8 Accel.	155.0	159.0	139.9
8 Cruise	387.1	322.4	326.4
8-10 Accel.	217.2	219.6	206.0
10 Cruise	439.7	380.4	417.1
10 Turn	441.0	413.2	418.2
10-8 Decel.	270.8	222.0	224.8
Total	1910.8	1716.7	1732.4

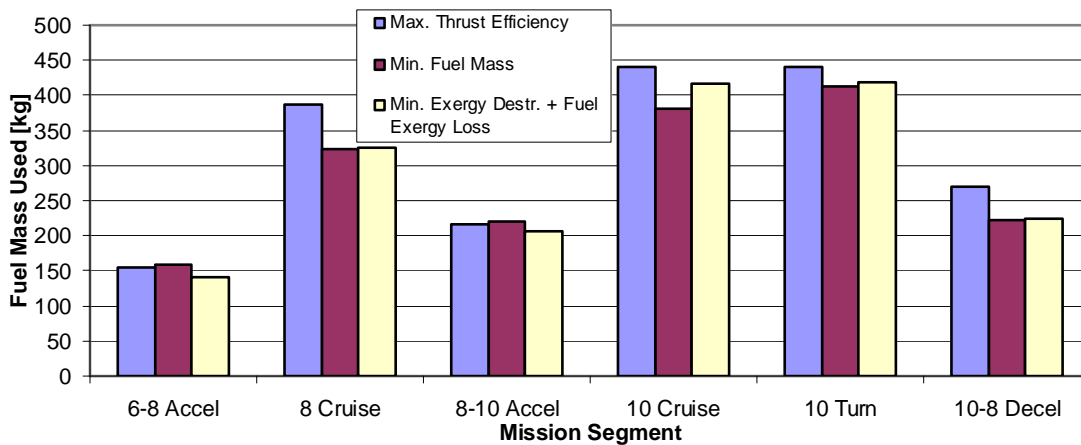


**Figure 5.14.** Fuel mass used per mission segment for each of the objective functions.

Table 5.17 shows the fuel mass fraction predicted by equations (3.116), (4.4), and (4.8) as well as the fuel mass fractions realized during the optimization of each of the objective functions. The estimates were closest to the performance for the thrust efficiency case, but for all three cases proved to be over-predictions. In this study, the empty mass is fixed at 4000 kg for a fuel mass fraction assumed of 0.3551. Thus, using equation (3.111), the gross takeoff weight of the vehicle is 6202 kg. The implication here is that, for a fixed initial vehicle mass, both the minimum fuel mass and minimum exergy cases allow for significantly more payload mass. However, if it is assumed that the payload is included in the empty mass of the vehicle, it also implies that the takeoff weight may be reduced through an iterative process since not all of the assumed fuel mass is needed.

**Table 5.17.** Optimum actual mass fractions versus the predicted mass fractions for the integrated hypersonic vehicle.

Mission Segment	Fuel Mass Fraction, $\pi_f$			
	Assumed	Max. Thrust Efficiency	Min. Fuel Mass	Min. Exergy Destroyed + Fuel Exergy Lost
Mach 6-8 Acceleration	0.0521	0.0250	0.0256	0.0226
Mach 8 Cruise	0.0651	0.0624	0.0520	0.0526
Mach 8-10 Acceleration	0.0508	0.0350	0.0354	0.0332
Mach 10 Cruise	0.0812	0.0709	0.0613	0.0673
Mach 10 Turn	0.0759	0.0711	0.0666	0.0674
Mach 10-8 Deceleration	0.0300	0.0437	0.0358	0.0362
TOTALS	0.3551	0.3081	0.2768	0.2793

Equations (4.4) and (4.8) indicate that the choice of lift to drag ratio,  $C_L/C_D$ , and mission segment overall efficiency,  $\eta_0$ , highly impact the resulting mass fraction estimations. Consequently, improved guesses, if desired, can be found by altering these quantities after initial data have been collected (i.e. substitute the optimum quantities from table 5.17 in place of the assumed quantities). It is likely, however, that a substantial decrease in the initial fuel mass, which in turn greatly reduces gross vehicle takeoff weight, may create a vehicle incapable of meeting all of the mission segment constraints due to the sensitivity of the model in general.

### 5.2.4 Vehicle Evolution

During the optimization process, the initial and final solutions were saved to illustrate the changes promoted by the objective functions. The best way to view the impact of each objective function optimization is through the vehicle plots shown in figure 5.15.

As seen in figure 5.15, the optimal thrust efficiency objective function drives the vehicle center of mass upward and toward the nose, increasing the vehicle volume, which is the opposite trend observed for the other two objective functions. The nose of the thrust efficiency vehicle remains constant, while the noses of the other two objective functions are driven downward (capturing less air), a result of the sleeker bodies needing less thrust to meet the mission constraints. In all cases, the cowl extension into the nozzle is nearly eliminated, implying that perhaps it is not entirely necessary in the quasi one-dimensional models developed here.

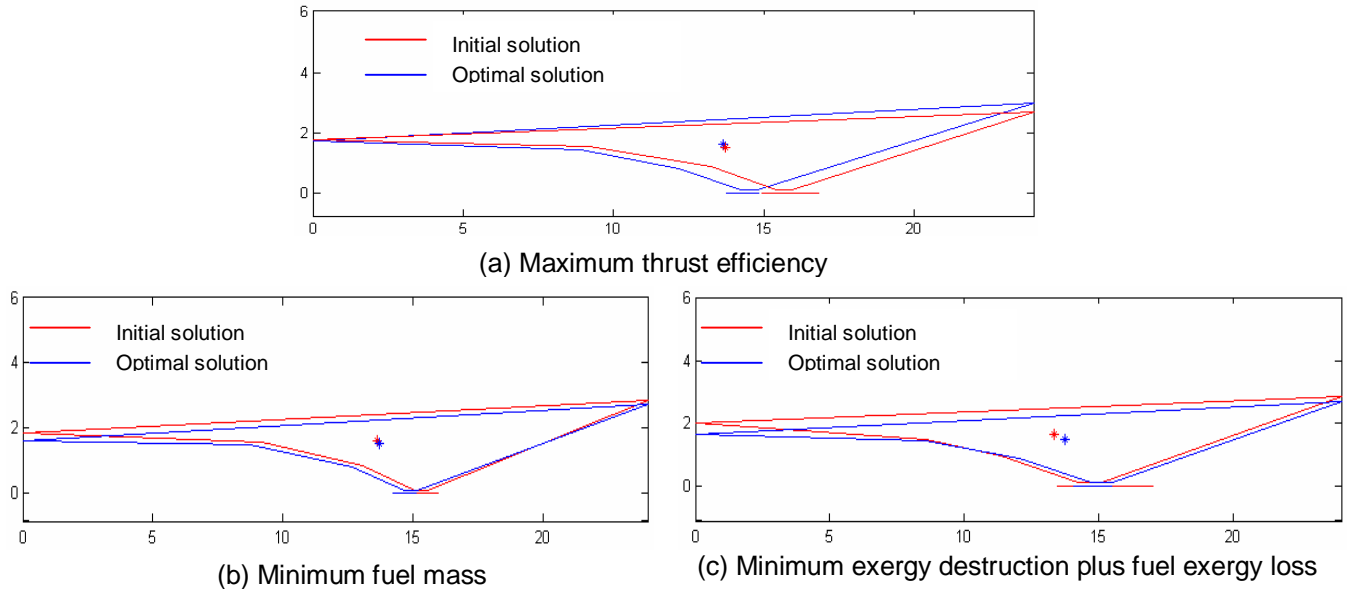


**Figure 5.15.** Vehicle geometry evolutions from the initial to the optimal solution for each objective function.

Table 5.18 quantitatively shows some tendencies for the objective functions. The fuel usage and exergy destroyed plus fuel exergy lost decreases significantly for all vehicles though it appears only small changes in geometry occur. This is a further indication of the level of integration of the engine and airframe. The vehicle volume increases for the maximum thrust efficiency vehicle and decreases for the other two. The same trend occurs with thrust. As expected, the maximum thrust efficiency vehicle increases thrust while decreasing fuel usage; however, it does so while decreasing fuel usage by more than 20 percent. The minimum fuel mass and exergy vehicles decrease fuel usage and thrust as they simultaneously decrease vehicle drag. *Since drag is neither directly nor indirectly accounted for in the maximum thrust efficiency objective function, it cannot produce the same fuel economy as the minimum fuel mass and exergy objective function vehicles for this mission-level analysis.*

**Table 5.18.** Mission characteristics for initial and optimal solutions.

		Max. Thrust Efficiency		Min. Fuel Mass		Min. Exergy Destroyed + Fuel Lost	
		Initial	Optimal	Initial	Optimal	Initial	Optimal
Vehicle Volume [m <sup>3</sup> ]		21.03	23.59	22.59	20.96	25.26	21.48
Fuel Consumption [kg]		2528	1911	1902	1717	2197	1732
Exergy Destruction [GJ]		201.3	153.7	157.6	145.2	166.2	140.0
Thrust [kN]	6-8 Accel.	54.73	55.35	54.84	53.54	56.19	55.85
	8 Cruise	12.25	13.13	10.38	9.015	11.06	9.85
	8-10 Accel.	47.84	49.26	48.47	47.98	48.78	47.81
	10 Cruise	9.263	9.789	8.817	7.430	9.951	8.040
	10 Turn	9.942	10.13	10.46	8.975	10.72	8.346
	10-8 Decel.	4.813	5.638	3.934	3.012	4.010	2.177

### 5.3 The Optimization Process

As in any optimization procedure, the interpretation of results depends highly on the software utilized. Consequently, this section is dedicated to surveying the overall characteristics and performance of the Queuing Multi-Objective Optimizer (QMOO). The optimum objective function value for each integrated vehicle along with the values of the other objective functions (not used to optimize the vehicle) are given in table 5.19 for each of the three optimizations conducted per vehicle.

**Table 5.19.** Objective function performance.

Objective Function	Max. Thrust Efficiency			Min. Fuel Mass			Min. Exergy Destroyed + Fuel Exergy Lost		
	1	2	3	1	2	3	1	2	3
Run									
First Law Efficiency [%]	<b>34.52*</b>	<b>34.48</b>	<b>32.97</b>	29.38	26.40	26.41	28.76	29.89	26.57
Fuel Mass [kg]	1911	1911	2227	<b>1717</b>	<b>1720</b>	<b>1744</b>	1732	1797	1801
Exergy Destruction [GJ]	153.7	151.1	166.2	145.2	139.3	140.2	<b>140.0</b>	<b>142.3</b>	<b>143.1</b>

\*Bold values represent the values of the objective function for which the system was optimized.

What should be noted immediately is that the minimum weight and minimum exergy destroyed plus fuel exergy lost optimizations for the best of the three runs in effectively the same result, i.e. within less than one percent of each other with respect to fuel usage. A closer result than this is not likely due to the nature of the optimization algorithm used, i.e. an evolutionary algorithm (EA). As mentioned in Chapter 4, to more closely pinpoint the actual optimum requires, for example, a hybrid algorithm which would take the results of the EA as the starting point for a gradient-based algorithm. It should also be noted that the minimum overall fuel mass consumed (run 1 for the minimum fuel mass objective), is associated with an exergy destruction plus exergy fuel loss value of 145.2 GJ, which has two implications. The first is that the 1717 kg of fuel consumed may be close to but is not the global minimum, which the following discussion will show is a reasonable conclusion. The second and more interesting, however, is that even though the minimum exergy destruction and minimum fuel consumption essentially coincide in terms of fuel usage, the fact that in one case 1732kg of fuel are burned and 140GJ of exergy destroyed or lost while in the other 1717 kg are burned and 145.2 GJ destroyed or lost implies that there is some importance or weighting to be placed on where the exergy is destroyed. Recalling from figure 5.12 that the minimum fuel mass consistently had fewer losses in the combustor and more fuel exergy lost, while the minimum exergy destroyed plus fuel exergy lost

objective function had the opposite trend, the result would imply that minimizing losses in the combustor is preferred over losses in fuel exergy out the back of the vehicle. However it could also be and may more likely be a numerical artifact of the vehicle models employed, specifically since all of these values differ only by small percentages starting from initial solutions which were significantly different. There is no obvious physical reason for one type of exergy destruction being more significant than any other, which is one of the principal benefits of utilizing an exergy approach to establish a universal currency for comparison of dissimilar loss mechanisms.

Now addressing the issue of a global minimum, table 5.20 shows a portion of the final population from the results file generated by QMOO for two different analyses. The first set is from the minimum exergy integrated hypersonic vehicle model used in this thesis, while the second set is from a non-related supersonic vehicle morphing wing study (minimum fuel burned for a mission segment) [60]. While just a sample of the total population is shown, these are representative portions of the actual solution file. For example, the total population of the case studied in this thesis is given in the first and is 128; the number of feasible solutions total only eleven or less than ten percent. For the study in [60], the population size is 70, all of which are feasible results. Essentially, the integrated hypersonic vehicle study in this thesis is so highly constrained that only isolated pockets of feasible points exist in the solution space, whereas for the morphing wing study there is a continuous distribution of such points. Feasible and infeasible results are differentiated, respectively, by those which contribute to moving the population toward the optimal solution and those which do not.

**Table 5.20.** Samples of results populations for sparse and dense optimal solution spaces.

Sparse Optimal Surface			Dense Optimal Surface		
Min. Exergy Destruction Plus Fuel Exergy Loss Population Sample [GJ]			Min. Fuel Usage Population Sample [kg] [60]		
5.0000E+15	5.0000E+15	5.0000E+15	5.5966E+02	5.9854E+02	6.1114E+02
5.0000E+15	5.0000E+15	5.0000E+15	5.4164E+02	5.3917E+02	5.6801E+02
5.0000E+15	5.0000E+15	5.0000E+15	5.9471E+02	5.5250E+02	5.7282E+02
5.0000E+15	1.4005E+02	5.0000E+15	5.7131E+02	5.8799E+02	5.7668E+02
5.0000E+15	5.0000E+15	5.0000E+15	5.7147E+02	5.5866E+02	5.5966E+02
1.4008E+02	5.0000E+15	5.0000E+15	5.9706E+02	5.7667E+02	5.4164E+02
5.0000E+15	5.0000E+15	5.0000E+15	5.8924E+02	5.6730E+02	6.0444E+02

The optimization algorithm breaks the solutions into groups or clusters, which evolve semi-independently toward optimal solutions, as discussed in the previous chapter. For this study, the largest number of clusters suggested by QMOO’s designers, i.e. eight, was employed. As part of the results file, one can view the cluster associated with each population member. What actually occurs is that all

so-called infeasible members are given the maximum exergy destruction plus fuel exergy loss value of  $5E+15$  GJ. In fact, all of the feasible solutions (again comprising less than ten percent of the population) were generated by cluster number one, indicating that the algorithm is forced to operate on this integrated vehicle model extremely inefficiently. Throughout this study, the largest number of groups to find feasible solutions was two. No experimentation was performed to observe the effect of varying population size and number of groups, which, as this analysis indicates, could provide valuable information for future investigations.

Again, there is also no guarantee that the evolutionary algorithm fully explores an island of solutions, since its next generation is produced based on mutation, cross-over, and selection. This essentially suggests that a gradient-based method, coupled with a genetic (evolutionary) algorithm, would provide the best means for optimization.

As mentioned earlier, one can see that the best value of minimum exergy destruction plus fuel exergy loss was found during the minimum fuel mass optimization process. In fact, initially, the minimum exergy destruction plus fuel exergy loss objective function was returning values of exergy destruction and fuel consumption much greater than those presented in the previous sections. It was only through the narrowing of the independent decision variables that the isolated solution spaces containing the better results were found. The variable ranges before and after constraint adjustment are illustrated in table 5.21. Having to make these adjustments is *not* a desirable result because, in general, the location of the best solution is typically not initially known! The reduced constraint limits allowed the program to run faster and find more solutions by searching less of the design space, and, as will be demonstrated in Section 5.5, permitted further exploration of vehicle performance capabilities.

**Table 5.21.** Decision variable constraint limits before and after range narrowing.

Variable	Initial Constraint Limits	Reduced Constraint Limits
Forebody position [m]	$8.4 \leq X_{fb} \leq 15.6$	$8.4 \leq X_{fb} \leq 12$
Cowl position [m]	$10.8 \leq X_{cowl} \leq 18.48$	$10.8 \leq X_{cowl} \leq 17$
Ramp 1 position [m]	$0.48 \leq X_{ramp1} \leq 7.92$	$1.0 \leq X_{ramp1} \leq 5.0$
Forebody angle [°]	$1.0 \leq \theta_{fb} \leq 6.0$	$1.0 \leq \theta_{fb} \leq 6.0$
Combustor length [m]	$0.50 \leq L_{comb} \leq 7.92$	$0.50 \leq L_{comb} \leq 2.5$
Nozzle expansion angle [°]	$8 \leq \theta_{nozz} \leq 18$	$8 \leq \theta_{nozz} \leq 18$
Percent nozzle length	$0 \leq \%_{nozz} \leq 25$	$0 \leq \%_{nozz} \leq 25$
Angle of attack [°]	$0.1 \leq \alpha_0 \leq 6$	$0.5 \leq \alpha_0 \leq 2.5$

As noted in table 5.14, the first angle of attack is given to more significant digits because it is chosen by the optimization program. The other angles are found by iteratively increasing angles of attack in 0.1 degree intervals through the entire range of possible solutions, i.e. 0.1 to 6 degrees, for every mission segment after the first. This is a highly undesirable situation because for each new angle of attack, the shock-on-lip calculation must be repeated. Again, due to the highly integrated nature of the program, the combustor now has new properties at its entrance, and thus the rest of the vehicle performance characteristics are affected and must be recalculated, including the throttling process (also an iterative process in which the combustor, nozzle and airframe must be resolved). This translates into a complete run of *one mission segment* in which 60 possible angles of attack are used to recalculate the segment requiring 60 times the time in which the algorithm may substitute a single successful variable. Though the overall process takes significantly longer, it does not always require the maximum amount of time mentioned above because it is possible for a simulation infeasibility to occur at any point in the simulation process so that the rest of the calculations are abandoned and the next angle of attack is substituted. In addition, the iterative process for the angle of attack of the second mission segment is not begun until an operable set of decision variables successfully completes the first mission segment. The iterative process to find the angle of attack for the third mission segment is not begun until the second mission segment is completed successfully, and so on.

Ultimately, what is desirable is to let the algorithm choose each of the angles of attack, primarily since they are independent variables. If done in this fashion, once an initial solution is found, the time for optimization would be reduced dramatically because not all 60 possibilities would have to be iteratively evaluated. The problem with allowing the algorithm to select all of the angles of attack is this: so few solutions exist that once a set of variables is found which are capable of meeting the initial design mission segment the chances of algorithm chosen angles of attack succeeding for each of the second, third, fourth, fifth, and sixth mission segments are hopelessly small. With six mission segments in a highly sparse solution space, the probability of making a single successful trip through the entire mission approaches zero. Markell [9] attempted this approach for a three segment partial mission without success; the algorithm exceeded several thousand generations without achieving a single feasible solution.

In essence, the compromise made is that the long time required to optimize the vehicle via the iterative method is faster overall than waiting for an initial solution to be found with the optimization algorithm determined variable values for the angle of attack. One possibility for improvement would be

to use the iterative method to isolate areas of interest in the optimal solution space, then to further constrain the range of angles of attack for each mission segment. A brief discussion on generations and computational time follows.

**Table 5.22.** Solutions (initial/optimal), generations (initial/optimal) and computation time for the minimum fuel mass objective function.

Run	Minimum Fuel Mass [kg]		
	Obj. Fun.	Generations	Time [days]
1	1902/1717	42/490	9
2	2221/1720	205/380	8
3	2231/1744	590/920	6

Table 5.22 shows the initial and final solutions, the resulting generation number, and the computational time required for optimization of the minimum fuel mass case. QMOO operates without generating large matrices, and consequently, performance is proportional to processor speed. Again, these optimizations were all performed on similar Machines, ranging in processor speed from two to three gigahertz. There is no method for predicting the amount of time or the number of generations for the optimization to occur, and the program does not stop itself; the results file, like that shown in table 5.20, must be consulted to confirm that all the successful objective function values are similar and unchanging from one generation to the next, for several consecutive generations. This genetic algorithm in particular generates seemingly random numbers of populations, ranging from 100 to 130 members (in this study), which contain varying numbers of feasible members. Typically, the larger the number of successful population members (potential optimal solutions), the faster the convergence to an optimal solution. In every case, the initial solution was found on the first day, typically within a few hours, with the remainder of the time dedicated to converging to an optimal solution. Examine, for instance, the second minimum fuel mass run. The first 205 generations were performed in less than one day, while the remaining 175 needed seven days to converge. The angle of attack iteration method consumed the majority of time during in the optimal solution convergence process.

A particular shortcoming of QMOO is that there is no method to limit the number of significant digits assigned to the decision variables. Every decision variable value assigned by the optimizer has fifteen significant digits. The disadvantage of this is as follows. For values from one to six with one significant digit, i.e. integer values, there are only six values to explore. Each added decimal place

creates a factor of ten more values to explore in order to traverse the entire space. QMOO will create populations from one generation to the next in which the decision variables only differ in the latter significant digits, for example, from the twelfth through fifteenth decimal places. This is an incredible waste of computational time. Much time was spent unsuccessfully exploring the possibility of decreasing the number of significant digits.

## **5.4 Total Mission and Mission Segment Optimization Comparisons**

The discussion that follows is dedicated to two primary comparisons. The first compares the combined performance of integrated vehicles optimized for each individual mission segment (on an exergy basis) to the performance of the single vehicle geometries found for the three objective functions based on mission-level optimizations. This is essentially a comparison of the three optimized mission-level vehicles performances (each of a single geometry) to a hypothetical vehicle able to change its entire geometry (to improve performance) at each mission segment. The second comparison is made based on flying each of the vehicles optimized for the individual mission segments through the entire mission and comparing their performance to the three optimized mission-level vehicles.

### **5.4.1 Combined Single Segment Optimized Vehicle Performance versus Mission-Level Optimized Vehicle Performance**

This section makes a comparison between the combined performance of a set of vehicles individually optimized for a single mission segment and that of the vehicle optimized for the overall mission. The approach taken here is an exergy minimization to determine an optimal vehicle for each of the mission segments composing the overall mission discussed in Chapter 4. Listed in table 5.23 are the best results for each of the integrated mission optimizations and the single mission segment optimizations. For the latter, each optimization was performed twice in order to ensure that a representative minimum was found. The mass fractions specified for each of the individual segments are taken from table 5.17 for the best minimum exergy destruction case of the integrated mission.

One interesting result is that all of the individually optimized segment vehicles choose appreciable sizes for cowl extensions into the nozzle ( $\%_{nozz}$ ), while the overall vehicles minimize them. The only other noticeable trend is that all of the single mission segment optimizations produce entirely

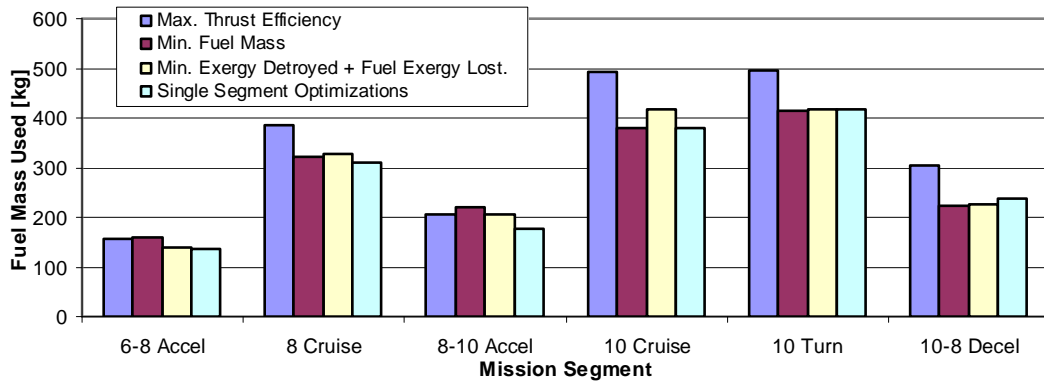
different vehicles. This result further demonstrates the need for a fully integrated synthesis/design process, as the possibility of combining each of these individual results is unrealistic, essentially requiring a vehicle which can change its entire geometry.

**Table 5.23.** Optimum decision variable values for the best performing runs of each objective function.

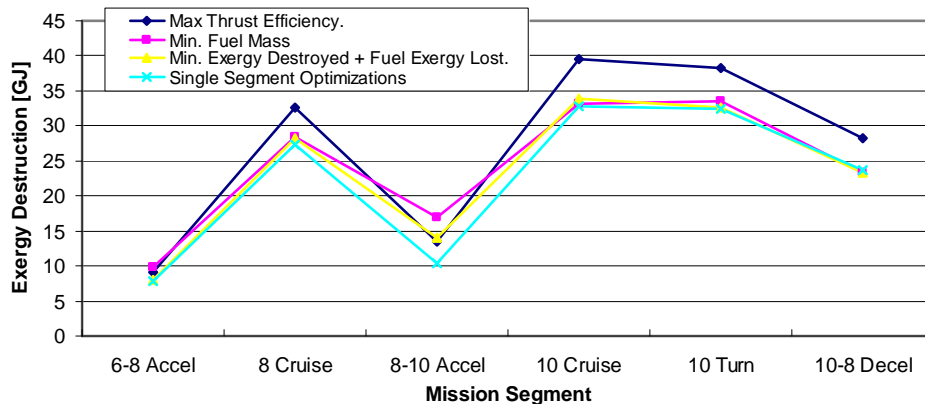
Objective Function	$X_{fb}$ [m]	$X_{cowl}$ [m]	$X_{ramp1}$ [m]	$\theta_{fb}$ [°]	$L_{comb}$ [m]	$\theta_{nozz}$ [°]	$\%_{nozz}$	$\alpha_0$ [°]
Max. Thrust Eff.	8.909	13.75	3.258	1.790	0.586	17.43	0.0063	1.687
Min. Fuel Mass	8.717	14.21	3.932	1.000	0.5000	16.67	0.5020	1.884
Min. Exergy	8.544	14.05	3.516	1.266	1.064	16.92	0.0100	2.129
Single Mission Segment Optimizations								
Mach 6-8 Accel.	8.443	14.62	3.702	1.006	1.030	15.70	12.74	1.506
Mach 8 Cruise	8.690	13.24	2.900	1.009	0.5286	10.46	19.25	1.081
Mach 8-10 Accel.	9.082	14.40	3.363	2.630	1.045	17.17	19.82	0.1000
Mach 10 Cruise	8.407	13.29	3.443	1.079	0.5537	12.93	12.50	0.4306
Mach 10 Turn	8.824	14.55	3.713	1.000	1.032	17.83	9.270	2.241
Mach 10-8 Decel.	8.537	12.98	3.030	1.000	0.5025	14.36	9.820	1.358

Figure 5.16 shows the exergy destruction plus fuel exergy loss and fuel consumption of the summed individual segment optimizations compared to the three objective functions of the integrated mission optimized vehicles. There are two segments in which the fuel consumed by the individually optimized vehicles is not the best, i.e. the integrated mission vehicle instead performed the specific mission segment using less fuel. These two segments, the Mach 10 turn and Mach 10 to Mach 8 deceleration, are also where the minimum exergy destroyed for the segment was not the overall minimum. This is attributable to the optimization algorithm used. Likely, since only two runs of each segment were performed, and, since the fuel usage and exergy destruction is not much more than the optimum for the integrated mission-level vehicles, more runs of the optimization would provide a slightly better performing vehicle. Since the vehicle mass at the beginning of each segment is exactly that of the minimum exergy vehicle using the actual mass fractions given in table 5.17, the optimization program, which is free to select the values for the design decision variables, should find a value of exergy destruction plus fuel exergy loss *at least* equal to the value found during the overall integrated vehicle minimum exergy destroyed optimization. However, considering that the inlet tailoring mechanism requires no first ramp shock tailoring for any of the single mission segments (since it never encounters a different angle of attack), one can reason that the individual segments should perform better both with respect to exergy destruction plus fuel exergy loss and the fuel used. This is particularly true for the Mach 10 to Mach 8 deceleration because, at an average Mach 9 flight condition, no forebody

energy addition is required as well. For this thesis work, it was too computationally expensive to discover how many more optimization runs would have to be performed to verify these conclusions.



(a) Fuel Consumption per Mission Segment



(b) Exergy Destroyed Plus Fuel Exergy Lost per Mission Segment

**Figure 5.16.** Performance characteristics for the single segment and integrated mission optimizations.

Overall, the individual segments do burn less fuel, at a total of 1660kg, compared to the best performing total mission minimum fuel mass objective vehicle which burned 1717 kg. The exergy destruction for the individual segments totaled 134.3GJ, which is also lower than the best value found for the total mission vehicle (140GJ). If the individual segments represent an integrated vehicle which can completely change its geometry, and, hence, were considered to be a “best” performance goal, it should be recognized that the minimum fuel mass and exergy integrated optimized vehicles perform impressively with a single geometry.

## 5.4.2 Mission-Level Performance of Single Segment Optimized Vehicles

Typically in aircraft design, as discussed in Chapter 1, vehicles are designed based on their most constraining mission segment or performance criterion. This section is dedicated to comparing the results of such a design methodology to the methodology utilized in this thesis work.

For this analysis, the single segment optimized vehicle values detailed in the previous section were each flown through the entire mission. Table 5.24 details the results. Only the Mach 6 to Mach 8 optimized single segment vehicle was capable of completing the entire mission. All other single segment optimized vehicles failed in this segment, while the vehicle for which it was specifically optimized completed the entire mission with “good” results (i.e. showing an improvement over each of the baseline configurations found for the objective functions of the mission-level optimizations), implying that the Mach 6 to Mach 8 acceleration is indeed the constraining mission segment.

**Table 5.24.** Failure location of single segment optimized vehicles flown through the entire mission.

Mission Segment	Angle of Attack [°]	Failure Segment	Component/Sub-System	Reason
Mach 6-8 Accel.	Completed Mission – see figure 5.17			
Mach 8 Cruise	$\alpha \leq 2.0$	Mach 6-8 Accel.	Combustor	$M < 1$
	$\alpha > 2.0$	Mach 6-8 Accel.	Inlet	Shock-on-lip
Mach 8-10 Accel.	$\alpha \leq 1.7$	Mach 6-8 Accel.	Combustor	$M < 1$
	$\alpha > 1.7$	Mach 6-8 Accel.	Inlet	Shock-on-lip
Mach 10 Cruise	$\alpha \leq 1.9$	Mach 6-8 Accel.	Combustor	$M < 1$
	$\alpha > 1.9$	Mach 6-8 Accel.	Inlet	Conceptual diffuser $M < 2.2$
Mach 10 Turn	$\alpha \leq 2.0$	Mach 6-8 Accel.	Combustor	$M < 1$
	$\alpha > 2.0$	Mach 6-8 Accel.	Inlet	Conceptual diffuser $M < 2.2$
Mach 10-8 Decel.	$\alpha \leq 1.8$	Mach 6-8 Accel.	Airframe	$S_{wing} > S_{wing, max}$
	$\alpha > 1.8$	Mach 6-8 Accel.	Inlet	Shock-on-lip

Four failure types were noted for the unsuccessful single segment optimizations. The most common were that the Mach number in the combustor became subsonic before reaching the nozzle and that the energy exchange mechanism could not maintain a shock-on-lip condition above certain angles of attack. At high angles of attack at Mach 10, the friction applied by the conceptual diffuser drove the Mach number below the required minimum value of 2.2 for the combustor entrance. Finally, the Mach 10 to Mach 8 deceleration vehicle made it through the inlet, combustor, and nozzle, yet failed in the

airframe sub-system because a larger than allowable wing area (lift) was required to balance the vehicle weight. Ultimately, a more comprehensive study in which various gross weights are examined would be of value.

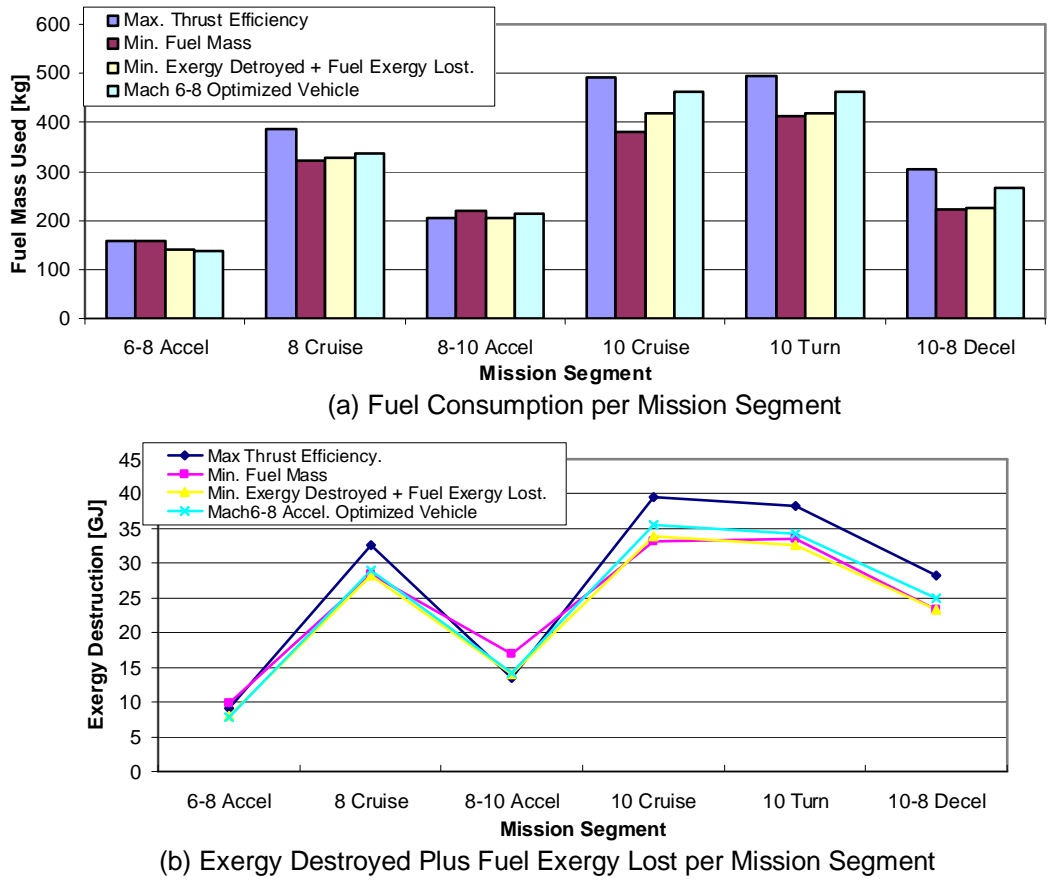


**Figure 5.17.** Performance characteristics for the Mach 6 to Mach 8 single segment optimized vehicle over the complete hypersonic mission envelope compared to the mission-level integrated vehicle optimizations.

The Mach 6 to Mach 8 single segment optimized vehicle performed the complete mission burning 1877kg of fuel and exergy destruction and loss of 145.8 GJ. This outperforms the thrust efficiency objective function mission-level optimized vehicle, but falls short of the exergy and fuel mass mission-level vehicles. Figure 5.17 suggests that the small gains made during the Mach 6 to Mach 8 acceleration (versus the mission level exergy and fuel mass vehicles) reduce its ability to perform well in other segments. This is, once again, an indication of the benefit of an integrated vehicle synthesis/design.

## 5.5 High Performance Mission Exploration

To test the limits of the hypersonic vehicle simulation program, an expanded mission was explored. This mission traverses nearly 10,000 km, reaches Mach 12, and is significantly more constrained. The constraining values and mission characteristics of the hypersonic vehicle flying this mission are given in table 5.25 (with values derived from the discussion in Chapter 4). The overall fuel mass fraction is increased fifty percent over the previous mission. Also, both accelerations require nearly double the net thrust to accommodate the climb angles and increased fuel mass.

**Table 5.25.** Mission segment characteristics and constraining conditions for the high performance mission.

Mission Segment	$t_{ms}$ [s]	$T_{veh}-D_{veh}$ [kN]	$\theta$ [°]	$R$ [km]	$\Delta h$ [km]	$\Delta V$ [m/s]	$\pi_f$	$n$
Mach 6-8 Acceleration	90	75.00	1.14	189	3.75	616	0.0551	1
Mach 8 Cruise	600	0	0	1440	0	0	0.0652	1
Mach 8-12 Acceleration	150	72.44	0.70	450	5.50	1250	0.1063	1
Mach 12 Cruise	600	0	0	2190	0	0	0.0973	1
Mach 12 Turn	675	0	0	2470	0	0	0.1089	2
Mach 12-8 Deceleration	1042	-6.400	-0.10	3150	-5.50	-1250	0.1000*	1
<b>TOTALS</b>	<b>3157</b>	<b>-</b>	<b>-</b>	<b>9889</b>	<b>-</b>	<b>-</b>	<b>0.5328</b>	<b>-</b>

\*Based on program experimentation.

**Table 5.26.** Equivalence ratios and fuel exergy lost per mission segment for the high performance mission exploration.

Mission Segment	$\phi$	Fuel Exergy Lost [GJ]
Mach 6-8 Acceleration	0.64	118800
Mach 8 Cruise	0.20	11150
Mach 8-12 Acceleration	1.18	230700
Mach 12 Cruise	0.4	26470
Mach 12 Turn	0.44	32000
Mach 12-8 Deceleration	0.20	8775

The outcome was a vehicle geometry which successfully met all of these new requirements. The results of this analysis are not necessarily comparable to the other results presented in this thesis, primarily because this vehicle was not optimized and its mission varies significantly. However, an

interesting result are the values of the equivalence ratios which were found for the high performance vehicle. These are presented in table 5.26. Though they will likely evolve some toward an optimal value, none of the initial or optimal solutions for the regular mission ever exceeded a value of one. This would indicate that there are major losses in fuel out of the mixing layer for which the high equivalence ratio is compensating. This corresponds to the calculated fuel exergy lost per segment. Since mixing efficiency is based on combustor length, it is likely that an exergy destruction minimization optimized result would extend the combustor length.

An unsuccessful attempt was made to increase the wing loading for the turn at Mach 12 to  $n = 3$ . It is likely that the inlet tailoring device, at Mach 12 and a high angle of attack, was unable to reduce the flow to Mach 9 while promoting a set of flow properties necessary for combustion. Had more time remained, further investigations into the limits of this high performance mission integrated model would have been examined. When the total mission was originally developed, it included this Mach 12 portion; however, the optimization routine was unsuccessful at finding a solution until the variable limits were further constrained. What can be gleaned is that the mission discussed in this thesis is just a sample of the potential for integrated hypersonic vehicle exploration.

# Chapter 6

## Conclusion

To summarize, a quasi one-dimensional hypersonic vehicle simulation model was designed and optimized over a formal mission with three objective functions: maximized thrust efficiency, minimized fuel consumption, and minimized exergy destruction plus fuel exergy loss. Through the numerous investigations performed in this work, many valuable conclusions can be drawn. They can be summarized as follows:

1. The dynamics of scramjets are much more complex than conventional aircraft. The impact of an almost indistinguishable boundary between engine and airframe results in a vehicle in which slight changes in one sub-system profoundly affect the other. Being able to sufficiently model the coupling of these effects, especially in a relatively new field such as this, for a single operating condition alone is a challenge. Consequently, only through the integrated synthesis/design optimization routine were optimal mission-level solutions obtained. Often, the search for solutions had to be refined before the possibility of success appeared.
2. Designing a hypersonic vehicle capable of meeting the numerous constraints of a multi-segment mission requires methods to accommodate the sensitivity of the system. For example, flow uniformity and optimum mass capture were maintained at all times via an energy exchange system motivated by the potential for the application of magnetohydrodynamics and plasma based technologies. In addition, a variable area wing was included to help the system meet the constraints of each individual mission segment.
3. The pairing of this particular genetic algorithm with the highly disconnected solution space of the mission-level analysis resulted in an inefficient optimization procedure for which many improvements can be made. The primary improvement would be to couple a gradient-based routine with the genetic algorithm. Even with this improvement, however, comprehensive vehicle models will likely still require long convergence times.
4. The combustor was the largest source for exergy destruction. It contributed to the overall loss in two ways. Not surprisingly, these two are highly related. Incomplete combustion, heat transfer, friction, and flow mixing losses are minimized for shorter combustor lengths: these are losses due to the exergy

destruction resulting from the irreversibilities in these models. Meanwhile, the mixing model, which dictates what percentage of hydrogen released into the flow is utilized, is most efficient for long combustor lengths. Because of this relationship, trade-offs between fuel exergy lost in the mixing layer and combustor exergy destruction were plainly recognized. Most notably, through the objective function analysis (discussed below), it did not matter which type of loss occurred, as the overall effect on vehicle performance was the same.

5. For the three objective functions, the minimum fuel mass and minimum exergy destruction and exergy fuel loss proved to be able to design and operate a vehicle which meets the mission constraints using nearly identical amounts of fuel. The optimized minimum fuel vehicle preferred larger mixing layer losses while the exergy destruction minimization vehicle preferred larger combustor irreversibilities. Both consumed similar fuel masses, destroyed similar amounts of exergy, and resulted in sleek vehicle geometries of the same proportion. The optimized thrust efficiency objective vehicle consumed significantly larger amounts of fuel and destroyed and lost more exergy while promoting a broad, thrust maximizing body.

6. Discretizing the cruise and acceleration mission segments illustrated some very valuable vehicle performance characteristics, such as sensitivity to angle of attack and a more accurate display of how the irreversibilities and fuel consumption vary throughout the segment. However, using the average flow properties of the less discretized mission proved sufficient for performance prediction, as the discretization yielded numerical differences totaling less than five percent.

7. Comparing single segment optimized vehicles to the overall mission optimized vehicles illustrated the necessity of a fully integrated synthesis/design approach. Though optimizing the most constrained mission segment yielded a vehicle capable of completing the mission with good results, the best vehicle performance was found only through an integrated synthesis/design over the entire mission.

8. Finally, an extended mission was flown for which the flight ceiling, gross takeoff weight, and thrust requirements were increased. The result was that a capable vehicle was found after variable constraints were modified. The need for constraint modification is undesirable for any optimization process (as feasible variable value ranges may not be initially known) but necessary in an integrated hypersonic vehicle study due to the highly coupled nature of propulsion and airframe sub-systems.

The many assumptions in this work, including frozen flow in the nozzle, heat transfer approximations, the potential for shock-on-lip control via energy exchange, etc. as well as the highly

constrained variables and sparse solution space available for mission-level hypersonic vehicle synthesis/design all suggest that the actual demonstration of such a vehicle is not likely to occur for some time. Needless to say, investigations into high-fidelity models including two- and three-dimensional effects, the feasibility of an MHD “machine”, finite-rate kinetics and dissociation, an expanded mission over various dynamic pressures, and optimization with a robust, combined genetic and gradient-based algorithm are all topics deserving further consideration and would undoubtedly provide much insight into the actual potential for mission-level hypersonic flight.

In essence, being able to predict the minimum allowable fuel usage as well as illustrate dissimilar component technology trade-offs, an exergy-based approach is a highly useful tool for integrated system synthesis/design. Though this study just scratches the surface of opportunity in hypersonic flight, it has hopefully sufficiently demonstrated the methodology to promote its expansion and development.

## References

- [1] Hill, P.G. and Peterson, C. R., *Mechanics and Thermodynamics of Compressible Fluid Flow*. Addison Wesley, Inc., Reading, Massachusetts. 1992.
- [2] Raymer, D. P., *Aircraft Design: A Conceptual Approach*. 3<sup>rd</sup> Edition, AIAA, Inc., Reston, VA. 1999.
- [3] Heiser, W. H., and Pratt, D. T., *Hypersonic Airbreathing Propulsion*. AIAA, Inc., Washington, D.C., 1994.
- [4] Anderson Jr., J. D., *Hypersonic and High Temperature Gas Dynamics*. AIAA, Inc., Reston, VA, 1989.
- [5] Curran, E. T., and Murthy, S. N. B., *Scramjet Propulsion - Progress in Astronautics and Aeronautics*, Vol. 189. AIAA, Inc., Reston, VA. 2000.
- [6] “NASA Hyper-X Program Demonstrates Scramjet Technologies,” *NASA Facts*. NASA. FS-2004-10-98-LaRC. Oct. 10, 2004.
- [7] Munoz, J. R., and von Spakovksy, M. R., “Decomposition in Energy System Synthesis/Designs Optimization for Stationary and Aerospace Applications,” *AIAA Journal of Aircraft*, Vol. 39, No. 6, 2003.
- [8] Rancruel, D. F., and von Spakovsky, M.R., “Decomposition with Thermo-economic Isolation Applied to the Optimal Synthesis/Design and Operation of an Advanced Fighter Aircraft System,” *International Journal of Thermodynamics*, Istanbul, vol.6, no. 3, Sept., 2003.
- [9] Markell, K. C., *Exergy Methods for the Generic Analysis and Optimization of Hypersonic Vehicle Concepts*. Department of Mechanical Engineering, Virginia Polytechnic Institute and State University, M.S. Thesis. 2005.
- [10] Perianann, V. *Investigation of the Effects of Different Objective Functions/Figures of Merit on the Analysis and Optimization of High Performance Aircraft System Synthesis/Design*. Department of Mechanical Engineering, Virginia Polytechnic Institute and State University, M.S. Thesis. 2005.
- [11] Moorhouse, D. J., “Proposed System-Level Multidisciplinary Analysis Technique Based on Exergy Methods,” *Journal of Aircraft*, Vol. 40, No. 1, Jan. – Feb. 2003.
- [12] Gyftopoulos, E. P., and Beretta, G. P., *Thermodynamics: Foundations and Applications*, Macmillan Publishing Co., New York, 1991.
- [13] Moran, M.J., “Availability Analysis: A Guide to Efficient Energy Use,” ASME Press, New York, 1989.

- [14] Greene, G. C., "An Entropy Method for Induced Drag Minimization," SAE TP Series 892344, Sept. 1989.
- [15] Moorhouse, D. J., Hoke, C. M., and Prendergast, J. P., "Thermal Analysis of Hypersonic Inlet Flow with Exergy-Based Design Methods," *International Journal of Applied Thermodynamics*, Vol. 5, No. 4, Dec. 2002.
- [16] Riggins, D. W., McClinton, C. R., and Vitt, P. H., "Thrust Losses in Hypersonic Engines Part 1: Methodology," *Journal of Propulsion and Power*, Vol. 13, No. 2, Mar. - Apr. 1997.
- [17] Riggins, D. W., "Thrust Losses in Hypersonic Engines Part 2: Applications," *Journal of Propulsion and Power*, Vol. 13, No. 2, Mar. - Apr. 1997.
- [18] Figliola, R. S, Tipton, R., and Li, H., "Exergy Approach to Decision-Based Design of Integrated Aircraft Thermal Systems," *Journal of Aircraft*, Vol. 40, No. 1, Jan.-Feb. 2003.
- [19] Moorhouse, D. J., Private Communication, Aug. 2003 - Aug. 2004.
- [20] Homan, K. O., "Inlet Flow Tailoring by Local Energy Deposition for High Speed Vehicles," Summer Research Presentation at Air Force Research Laboratories. Dayton, OH. July 2004.
- [21] Van Wie, D. M., and Nedungadi, A., "Plasma Aerodynamic Flow Control for Hypersonic Inlets," AIAA Paper No. 2004-4129, 2004.
- [22] Camberos, J. A., "Quantifying Irreversible Losses for Magnetohydrodynamic (MHD) Flow Simulation," AIAA Paper No. 2003-3647, 2003.
- [23] Taylor, T. and Riggins, D.W., "Impact of Electro-Magnetics and Ionization on Mixing and Combustion in Scramjet Combustors," AIAA Paper No. 2004-0859, 2004.
- [24] Schneider, et al., "Steady and Unsteady Supersonic Flow Control with Energy Addition," AIAA Paper No. 2003-3862. 2003.
- [25] Bowcutt, K., "Hypersonic Aircraft Optimization Including Aerodynamic, Propulsion, and Trim Effects," AIAA Paper No. 1992-5055, 1992.
- [26] Hendrick, I. P., "First Law of Thermodynamics Complimentary with First Law for Optimization of a Hypersonic Airbreathing Propulsion System," ICAS Paper No. 94-6.7.1, 1994.
- [27] Starkey, et al., "Coupled Waverider/Trajectory Optimization for Hypersonic Cruise," AIAA Paper No. 2005-530, 2005.
- [28] Starkey, R. P., "Scramjet Optimization for Maximum Off-Design Performance," AIAA Paper No. 2004-3343, 2004.
- [29] Ngo, A. D., "A Fuel-Optimal Trajectory for a Constrained Hypersonic Vehicle Using a Direct Transcription Method," IEEEAC Paper No. 1223, 2004

- [30] Brilliant, H. M., "Analysis of Scramjet Engines Using Exergy Methods," AIAA Paper No. 1995-2767, 1995.
- [31] Riggins, D. W., "High-Speed Engine/Component Performance Assessment Using Exergy and Thrust-Based Methods," NASA Contractor Report 198271, 1996.
- [32] Markell, K. C., Brewer, K.M., and von Spakovsky, M. R., "Exergy Methods for Mission-Level Integrated Analysis and Optimization of Hypersonic Vehicle Concepts," Summer Research Presentation at Air Force Research Laboratories. Dayton, OH. July 2004.
- [33] Roth, B. A., "A Work Potential Perspective of Engine Component Performance," AIAA Paper No. 2001-3300, 2001.
- [34] Roth, B. A., and Mavris, D. N., "Generalized Model for Vehicle Thermodynamic Loss Management," *Journal of Aircraft*, Vol. 40, No. 1, Jan. – Feb. 2003.
- [35] Moorhouse, D. J., and Suchomel, C. F., "Exergy Methods Applied to the Hypersonic Vehicle Challenge," AIAA Paper No. 2001-3063, 2001.
- [36] Rancruel, D. F., and von Spakovsky, M. R., "Use of a Unique Decomposition Strategy for the Optimal Synthesis/Design and Operation of an Advanced Fighter Aircraft System", 10<sup>th</sup> AIAA/ISSMO Multi-disciplinary Analysis and Optimization Conference, Albany, New York, 2004.
- [37] von Spakovsky, M. R., and Evans, R. B., "Engineering Functional Analysis (Part 1)", *Journal of Energy Resources Technology*, Vol. 115, No. 2, June 1993.
- [38] Munoz, J. R., and von Spakovsky, M. R., "The Application of Decomposition to the Large Scale Synthesis/Design Optimization of Aircraft Energy Systems", *International Journal of Applied Thermodynamics*, Vol. 4, No. 2, June 2001.
- [39] Munoz, J. R., and von Spakovsky, M. R., "A Decomposition Approach for the Large Scale Synthesis/Design Optimization of Highly Coupled, Highly Dynamic Energy Systems", *International Journal of Applied Thermodynamics*, Vol. 4, No.1, March 2001.
- [40] Mattingly, J. D., Heiser, W. H., and Daley, D. H., *Aircraft Engine Design*, AIAA, Inc., Washington, D.C., 1987.
- [41] John, J. E. A., *Gas Dynamics*, 2<sup>nd</sup> Edition, Prentice Hall, Upper Saddle River, NJ, 1984.
- [42] Shapiro, A. H., *The Dynamics and Thermodynamics of Compressible Fluid Flow*, 1<sup>st</sup> Edition, John Wiley and Sons, New York, 1953.
- [43] Moorhouse, D. J., Hoke, C. M., and Prendergast, J. P., "Thermal Analysis of Hypersonic Inlet Flow with Exergy-Based Design Methods," *International Journal of Applied Thermodynamics*, Vol. 5, No. 4, Dec. 2002.

- [44] Schindel, L., "Effect of Non-uniform Nozzle Flow on Scramjet Performance," *Journal of Propulsion and Power*, Vol. 15, No. 2, Mar. – Apr. 1999.
- [45] Chase, M.W., et al., *JANAF Thermochemical Tables*, 3<sup>rd</sup> Edition, American Chemical Society, Washington, D.C., 1985.
- [46] Riggins, D. W., "Evaluation of Performance Loss Methods for High-Speed Engine and Engine Components", *Journal of Propulsion and Power*, Vol. 13, No. 2, March-April 1997.
- [47] Riggins, D. W., Private Communication, July 2003 - July 2004.
- [48] Stalker, R. J. and Morgan, R. G., "Supersonic Hydrogen Combustion with a Short Thrust Nozzle," *Combustion and Flame*," Vol. 57, 1984.
- [49] Del Guidice, Dash, and Kalben, "A source Flow Characteristic Technique for Analysis of Scramjet Exhaust Flow Fields," NASA Contractor Report 132437, 1974.
- [50] Chavez, F. R., and Schmidt, D. K., "Generic Hypersonic Vehicle Performance Model," NASA Contractor Report 192953, 1993.
- [51] Lehrach, R.P.C., "Thrust/Drag Accounting for Aerospace Plane Vehicles," AIAA Paper No. 1987-1966, 1987.
- [52] Numbers, K., "Hypersonic Propulsion System Force Accounting," AIAA Paper No. 1991-0228, 1991.
- [53] Anderson Jr., J. D., *Fundamentals of Aerodynamics*, 3<sup>rd</sup> Edition, McGraw-Hill, New York, 2001.
- [54] Bejan, A., *Entropy Generation Minimization: The Method of Thermodynamic Optimization of Finite-Sized Systems and Finite-Time Processes*, CRC Press, Inc., Boca Raton, FL, 1996.
- [55] Moorhouse, D. J., Private Communication, June 2003-August 2004.
- [56] Leyland, G. B., *Multi-Objective Optimisation Applied to Industrial Energy Problems*, Department of Mechanical Engineering, University of Auckland, Ph.D. Dissertation. 2002.
- [57] Floudas, C. A., *Nonlinear and Mixed-Integer Optimization: Fundamentals and Applications*, Oxford University Press, New York, 1995.
- [58] Dornheim, M. "A Breath of Fast Air," *Aviation Week and Space Technology*, April 5<sup>th</sup>, 2005.
- [59] Bowcutt, K., "Hypersonic Aircraft Optimization Including Aerodynamic, Propulsion, and Trim Effects," AIAA Paper No. 1992-5055, 1992.

[60] Butt, J., "A Study of Morphing Wing Effectiveness in Fighter Aircraft Using Exergy Analysis and Global Optimization Techniques," M.S. Thesis. Virginia Polytechnic Institute and State University, Blacksburg, VA. 2005.